Cranfield University

JAVIER LECHUGA

Computational nanoscience of flow and mass transport through biological membranes

School of Engineering

PhD

Cranfield University

School of Engineering

Fluid Mechanics and Computational Science Group

PhD

2007-2008

JAVIER LECHUGA

Computational nanoscience of flow and mass transport through biological membranes

DIMITRIS DRIKAKIS

16^{th} January 2008

Abstract

The study presented in this document is the result of three years of research into the complex world of *Molecular Dynamics* applied to biological cell membranes.

The simulation of biological tissues involves not only an excellent knowledge of the numerical calculus and its related tools, but a profound comprehension of the biological and medical literature associated with the phenomenon.

By the other hand, the use of high performance facilities is essential for the computation of the *Molecular Dynamics* models in order to obtain results in acceptable times, so the latest technological advances have played a decisive and important part in this field of research.

The presented obtained results about shock wave interaction with biological membranes, as well as the air flow through the alveolar surface, are part of a new line of research usually known as "virtual experimental". This name comes from the fact that any physical or chemical situation can be re-created into a computer system to calculate its propagation in time.

The results of the interaction of shock waves with biological cell membranes have been particularly satisfactory and they have opened a new line of investigation into cancer research. A numerical proportional relation between the shock wave impulse and the value of lateral diffusion (from 9.80 to 12.84 $10^{-7} \cdot \frac{cm^2}{s}$), as well as the simulation of the transient provoked by the wave into a NPT ensemble are a successful achievement.

Other computations of this type of interaction have been simulated into an NVE ensemble as well, however the obtained results for the lateral diffusion, in the order of $10^{-7} \cdot \frac{cm^2}{s}$, showed no trend regarding the shock wave and the transient effect could not be simulated.

On the other hand, the recreation of the air flow through the alveolar surface is an initial step into the solution of all the controversy surrounding this extremely complex system known as alveolar surface network. An alveolar membrane of around 7 nm has been successfully simulated in agreement with Scarpelli's experiments.

This lipid-protein membrane model simulated can serve as a virtual experiment in order to solve the controversy about the alveolar surface. It points to the possibility of air flow through a stable two-layered DPPC phospholipid structure either from a numerical or physical and biological point of view and the existence of an alveolar membrane at the end of the bronchial tubes.

Acknowledgements

Three years have past since the beginning of this PhD, friends came and went, some of them are still on the campus, but others are not. I am sure I will not be able to remember all of you but I will make an effort to find you a place on this acknowledgement page.

I arrived on campus in January 2005 and thanks to my colleagues at the department, I soon fitted in. I would like to give special thanks to Marco K. and Evgeniy S.

Other people in the department at Cranfield university who have given me support include: Yiannis K., Zeshan M., Zacharias Z., Marco H and Sanjay P. Thanks for being part of Cranfield University. Matias B., Nicholas E. and Antoni M., I will never forget your kindness.

Outside the department, I found a place in the Badminton Club. I would like to thank Marta and the Polish friends for their commitment and give my admiration to the Chinese community. Nevertheless, I do believe the foundations of the club lie in Bobby. Thank you for playing badminton, mate.

Thanks as well to the people around Campus: Sue; Delia; Paul; Kranti and the Indian friends; Yura; Emanuele; Peter; Arne; Laszlo, Slavisa and the Serbian friends; Mark, Barry and Bek; cool Mathieu; the Greek community (including Nikos and the "C++ team"); Carlos; Rodolfo; Pablo and Ali; and the staff friends at Mitchell Hall and Conference Centre.

Outside the campus, I would like to keep in my heart the Cranfield village people, specially Pauline, beloved Peter, Tom, David and Keith.

I would not want to forget all my office and flat mates during these years, specially Shuguang, who is not bad ping pong player, and Sining, who can still share a house with me.

Special thanks to Heather Simpkins for her help in proof reading parts of this thesis.

My gratitude to my external Referees Doctor Marcus Grzechnik and Doctor John Hunt who recommended me to undertake this PhD.

Special recognition to my supervisor, Professor Dimitris Drikakis, who supported me through this PhD and Professor Sandip Pal for stimulating technical discussions.

I would like to thank Cancer HEAL Charity and Broomfield Hospital as well for their partial financial support.

No one rises so high as he who knows not whither he is going,
Oliver Cromwell (1599-1658)

Contents

List of Figures

List of Tables

Nomenclature

δ_i	Dihedral angle between the second two pair of covalent bonds for a time step i
ϵ	Dielectric constant
ϵ_{ij}	Depth of the potential
γ	Collision frequency
ω_0	Initial improper dihedral angle
ω_i	Improper dihedral angle for a time step i
ϕ_i	Dihedral angle between the first two pair of covalent bonds for a time step i
σ_{ij}	Distance at which the interparticle potential is zero
Θ_0	Initial angle between a pair of covalent bonds
Θ_i	Angle between a pair of covalent bonds for a time step i
$\vec{F}_i$	Force applyed to particle i
A	Area
D	Diffusion coefficient
d_f	Number of dimensions ijn which the diffusion occurs
E_k	Kinetic energy
I_p	Impulse
k_B	Boltzman constant
k_i^{angles}	Parameter to compute the potential in the angles

k_i^{bonds} Parameter to compute the potential in the bonds

$k_i^{dihedrals}$ Parameter to compute the potential in the dihedrals

$k_i^{impropers}$ Parameter to compute the potential in the improper dihedrals

M Mass

m_i Mass of the particle i

N Number of particles

P Pressure

q_i Charge of particle i

q_j Charge of particle j

$R(t)$ Random force taken from a Gaussian distribution with zero mean and variance

r_0 Initial position of a particle

r_i Position of a particle for a time step i

r_{ij} Distance between two particles

S_{cd} Deuterium order parameter

T Temperature

$U(\vec{R})$ Potential

V Volume

v_i Velocity of the particle i

Z_n Gaussian random value of zero mean and variance 1

DMPC Dimyristoylphosphatidylcholine

DPPC Dypalmitoylphosphatidylcholine

ESW Extracorporeal shock wave

LASER Light Amplification by Stimulated Emission of Radiation

LSW Laser shock wave

ns Nanosecond

POPC Dalmitoyloleoylphosphatidylcholine

POPE Dalmitoyloleoylphosphatidylethanolamine

ps Picosecond

t Time

Executive summary

The interaction of lasers, ultrasonics, extracorporeal shock waves or photoacoustics on biological tissues, cells or macromolecules are of great interest to science and medical applications and, even though many experimental studies have been done in this field for more than 20 years, there is still much to understand and, in addition, the effects of these interactions are not well understood, yet.

There is a variety of situations in medicine which suggest the application of different waves to provoke an interaction with the biological system. A few examples of these kinds of situation are:

- Bone surgery [1] and pseudarthrosis [2] and [3].
- Cancer treatment [4] and [5].
- Selective cell killing [6].
- Lithotripters to disintegrate kidney stones [7] [8].
- Ophthalmology [9].
- Shock wave interaction with biological cells [10] [11] [12].
- Molecular delivery [13]

The first study in this project is focused on the interaction of shock waves with cell membranes in order to provide, in long term, important information for cancer treatment, with anti-cancer agents, implying a mass transport through the cell membrane, or without it.

Biological cell membranes are neither completely rigid nor fluid, but they are characterised by a delicate balance between rigidity and fluidity. The properties of a biological membrane are the result of a precise detailed composition

of a double layer (bilayer) which contains phospholipids of various types as well as different proteins and other components.

The mass transport through a biological cell membrane occurs naturally and it can be measured using different techniques [14]. However, in the case of cancer treatment, it is rather interesting to increase the uptake of anti-cancer agents by the tumour cells in order to decrease their growth. When applying shock waves to these cells, a transient permeability of the membrane occurs, so the uptake of other macromolecules as anti-cancer agents can be increased, consequently, decreasing the tumour growth [15].

The term shock wave is often used to describe the pressure waves generated by extracorporeal shock wave lithotripters and pulsed lasers [16].

It has been demonstrated that short laser pulses can generate different kinds of shock waves into living structures [17] [18] and, at about the same time, the biomedical research community also became aware of the potential damage those stress waves could generate during medical applications of pulsed, high-power lasers [19].

On the other hand, the use of shock waves in cancer treatment is a promising method to decrease cancer tumour growth and the comprehension of this process is fundamental to decrease other and possibly more harmful effects [20].

The study of the membrane requires such sophisticated physicochemical techniques that researchers have chosen to perform investigations on synthetic models. However, in order to precisely analyse this extremely complicated process, computer simulations provide an unique tool to understand biomembrane properties from an atomistic perspective with a level of detail that is missing in any other technique.

An alternative to the *Monte Carlo* analysis has arisen, achieving an excellent conformity with experimental results. *Molecular Dynamics* simulation studies on simple model membranes consisting of phospholipid bilayers in the biologically relevant fluid phase have permitted new applications to membrane systems of a considerable degree of complexity. These complex systems usually consist of the introduction of other molecules, such as solutes, membrane peptides or proteins into a simple phospholipid bilayer model [21].

As the modelling of these molecular structures and the simulation of external shock wave influences can be computed using *Molecular Dynamics* techniques, the physical and structural properties of those systems along a time

scale can be examined and analysed.

The simulation of shock waves applied to biological cell membranes using computer science techniques is quite a new and original subject in the research community. This makes it rather difficult to find any literature about it, so the research must be started almost from its basic physics.

As an essential feature of the whole dynamical structure which is the cell membrane, the fluidity is relevant to its proper functioning and particularly to the functioning of the proteins bounded to or embedded in it. The proteins, as well as the surrounding phospholipids, are thought to be freely diffusing in the plane of the membrane and this process is of considerable interest and importance for the understanding of the functions of biological membranes [22].

Regarding to this phenomenon, and even though there is a article [23] which has described a numerical scheme for a particular case, there is not any complete and detailed study about it. One relevant issue, the explanation of the effects of the shock wave on cancer chemotheraphy is still a matter to understand and the presented numerical approach becomes the first numerical proper study about it (See chapter 4).

On the other hand, there are other biological membranes which have been studied. In the case of the lungs, and after years of controversy, diverse models for the alveolar surface have been published.

In any case, it is accepted that single layer phospholipid membranes embedded into pulmonary fluid and alveolar gas form liquid-air interfaces or sacs similar to air bubbles in water [24]. These kind of membranes found in the lungs are part of the so-called pulmonary alveoli, which consist of an extracellular matrix surrounded by capillaries.

The alveoli permit an air flow through the phospholipid layer thanks to the presence of pulmonary surfactant, a protein which decreases the surface tension of watery fluids letting the gas penetrate into the blood and producing the so-called gas exchange.

There is not numerical study about the behaviour of these alveolar structures and how the gas flow happens through the membrane. However, it is possible to find plenty of experimental studies about the alveolar structure [25] and set up a virtual experiment using computer techniques in order to obtain a detailed description of this phenomenon.

The existence of an alveolar membrane at the end of the bronchial tubes is a missing detail in the experimental work as it can not be identified because of the modifications produced by the experimental analysis, only a virtual experiment could show this structure (See chapter 5).

The *Molecular Dynamics* method provides a precise and extraordinary technique to analyse, examine and comprehend all these processes from a molecular level as will be shown in detail within this document.

The aim of the present research is to contribute to the understanding of shock wave interaction and mass flow through biological membranes using advanced *Molecular Dynamics* modelling techniques.

The objectives for this PhD project are listed below:

1. To develop computer models for different membranes with several types of phospholipid molecules (POPC, POPE, DMPC and DPPC). The inclusion of other molecules, such as proteins, and their repercussion in the membrane will be studied.

2. To develop computer models for investigating the interaction of a shock wave with the cell membranes providing detailed information about this phenomenon and its application in cancer chemotherapy.

3. To provide information to the computational science community and to medical practitioners, as well as biologists, about the shock waves on biological membranes.

4. To perform extensive simulated studies and analysis of the results for ranges of parameters involved in the modelling process in other to compare different *Molecular Dynamics* ensembles which lead to different results.

5. To develop *Molecular Dynamics* models to study the mass flow through biological cell membranes setting up virtual experiments for the alveolar surface.

Chapter 1

Introduction

Even though the flow and mass transport through a biological membrane is a process which can be studied using CFD techniques, because of the dimensions and time scales involved in the studied processes, important details could be missed.

When, rather than trying to get a mean value to characterise the flow through the membrane in terms of mass transport, a detailed study of the movement of the particles is necessary, *Molecular Dynamics* techniques provide an alternative of the *Monte Carlo* analysis, so, instead of probability ranges, an explicit numerical solution is achieved.

Within this document, and by using the *Molecular Dynamics* methodology, several studies with different medical applications will be presented.

The first study will be focused on the interaction of shock waves with cell membranes and the influence of that interaction on permeability and diffusion; the second study will be based in alveolar membrane gas flow.

1.1 Biological membranes and permeability.

The basic composition and structure of a biological membrane is a phospholipid bilayer [26] often described as a "fluid mosaic" [27]. This is a two dimensional fluid, along the cell surface, composed of freely diffusing phospholipids with embedded proteins, which may function as channels or transporters across the membrane and other complex molecules such as cholesterol, glycolipids,

carbohydrates and filaments of cytoskeleton (See figure 1.1) which can have different diverse functions such as the formation of microdomains [21].

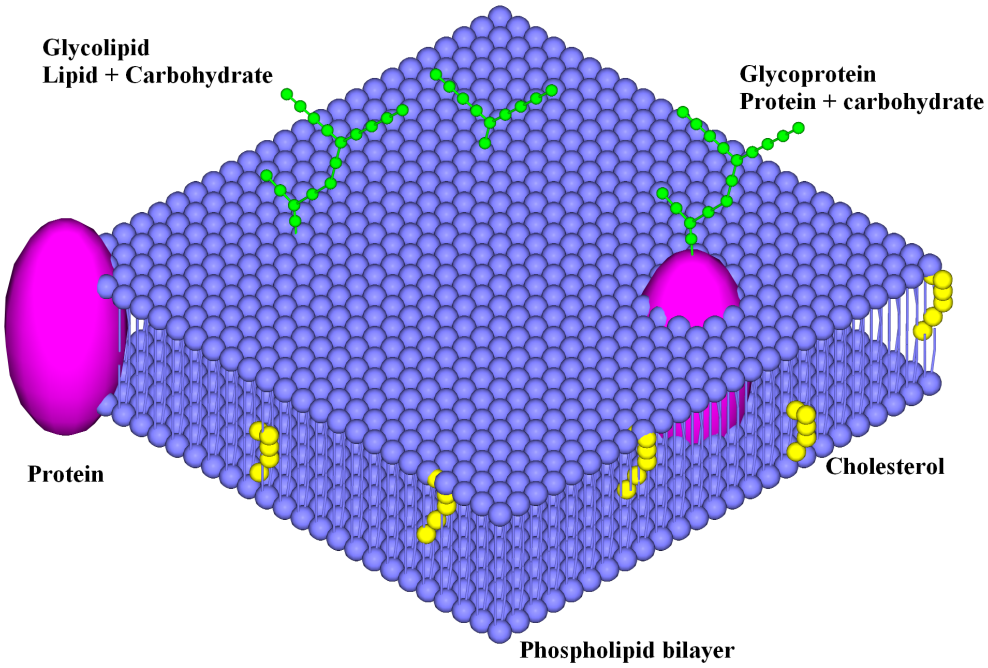

Figure 1.1: Fluid mosaic model.

The phospholipids have a hydrophilic head and a hydrophobic tail. In the case of biological cell membrane bilayers, the polar heads are placed in contact with the extracellular fluid and the intracellular cytoplasm, both rich in water (more than 80%), while the non-polar tails point inwards avoiding contact with fluid, as shown in figure 1.1. According to the fluid mosaic model [27], this structure is fluid, so the molecules can move around the membrane surface.

As the cell cannot survive as a closed system, the molecules must enter and leave the cell through the plasma membrane. This process implies an ion concentration balance between the inside and the outside of the cell in order to obtain osmotic equilibrium.

The phospholipid bilayer, said to be semi-permeable, is the major route of water [28]. The osmotic balance has to be achieved by special proteins embedded into the membrane which serve as active channels for diverse molecules which can be pumped in or out of the cell.

When a molecule or ion crosses the membrane without input of metabolic

energy, it is said to be transported passively by moving down a concentration or electrochemical gradient. Another name for this process is diffusion.

The passive transport through the cell membrane or diffusion process is driven by the kinetic theory of matter. According to this theory, matter is composed of small components (atoms or molecules), all in random motion. The energy of these particles is called kinetic energy, proportional to their temperature and velocity. The motion theoretically stops when temperature reaches absolute zero, which means there is no kinetic energy.

The diffusion process is balanced within the biological system, and the flow of substances between the inside and outside of the membrane therefore occurs naturally. However, in the case of medical treatments, an artificial increase of that flow can be of vital importance.

Regarding this effect, it is known that thermal fluctuations in the lipid bilayer can make a molecule cross the membrane into the biological cell without involving a diffusion process. In this case, and due to transients effects [29], the permeability could be increased to two orders of magnitude [30].

Diffusion and thermal fluctuation processes are not mutually exclusive and both can drive a molecule through the membrane, but, in order to get a significant increase of the permeability, the focus is on the artificial provocation of that thermal fluctuation.

By the other hand, the lateral diffusion in lipid membranes has been studied for at least 40 years, the mechanism by which lipids diffuse is not well characterized or understood. Several theories exist [31] [32] relating to their lateral diffusion and one might expect that this diffusion is similar to that of an ideal fluid on a two-dimensional surface.

Both permeability and lateral diffusion are strongly affected by the amount and distribution of free volume or area in a membrane (space not occupied by phospholipids) and it is reasonable to expect that the changes in these properties are somehow coupled [33].

1.2 Shock wave interaction with biological membranes.

The effects of shock waves on cells and tissue have been a recurrent theme of investigation involving researchers in ultrasonics, photoacoustics, lithotripsy or laser-tissue interactions [34], where the term "shock wave" is often used to describe the pressure waves generated by extracorporeal shock wave lithotripters (ESW) and pulsed lasers (LSW) [16], which, as well as ultrasounds, can increase the permeability of the cell membrane [35].

A shock wave is defined as a discontinuity in pressure, density, particle velocity and internal energy, otherwise the more general term stress wave would be used [36].

As more than 80% of blood consists of water, those shock waves can be considered into an aqueous system and treated as underwater shock waves in three dimensions, i.e. reflection, refraction and diffraction, which at non-normal incidence cannot lead to larger values of the pressure, particle velocity or partial displacement [37].

LSW, which van be generated by ionization of the medium (optical breakdown), ultraviolet radiation (ablation) or rapid heating of the absorbing medium below ablation threshold [38], have unique optical properties which make them much more interesting than other sources for the generation of shock wave and tissue interaction, namely, as spatial and temporal coherency, minimum angular beam divergence, polarisation and monochromaticity. Beneficially, they do not produce those tensile components observed in ESW [11].

Furthermore, as a source of radiant energy of extremely high instantaneous power [37], LSW can be used for other purposes such as selective cell killing based on the radiation absorption of the different particles which make up the laser target [6].

An LSW can be generated by optical breakdown, ablation and rapid heating of an absorbing medium. Their characteristics depend on the laser parameters, namely, wavelength, pulse duration and fluence [35] which cause an impulse to the targeted tissue and a change in the linear momentum of the particles as will be explained within this document in the numerical definition of the shock wave.

The laser-tissue effects are usually divided into photochemical, photother-

mal and photomechanical effects.

The photomechanical effects include a wide number of phenomena, such as ablation, plasma, cavitation, micro-jet formation or shock wave generation. These effects are not completely independent because the expansion of the membrane and cavitation can lead to the generation of shock waves, and cavitation in the proximity of a solid boundary can lead to micro-jet formation [36].

Cavitation occurs when the water phase changes into vapour, which can be produced by LSW as they increase the pressure value, and the vaporisation-energy threshold can be exceeded by the current temperature and density.

From this point of view, a decrease in cavitation would produce a decrease in the cell damage and an improvement of the cell membrane recovery after the shock. This is why the use of low pressure waves below the vaporisation threshold, i.e. where the thermoelastic expansion is the dominant effect, would be less dangerous for the tissues than high pressure waves which move at supersonic speed inducing additional vaporisation effects [39].

However, the generation of the shock wave requires a fast energy rise to provoke discontinuity in pressure, density, particle velocity and internal energy [40]. This effect can be achieved by the use of different lasers [37].

The process of a macromolecule introduction into a biological cell due to an LSW exposure would be as follows:

1. Show wave generation and high particle velocity rise.
2. Cell membrane permeability transiently increases.
3. Uptake of the macromolecule.
4. Cell membrane recovery.

1.3 Cancer treatment.

The application of shock waves to biological tissues is a promising method for cancer treatment as they have the capability of retarding a tumour growth either alone or when increasing the uptake of anticancer agents through the cell membrane [16].

This effect has been demonstrated in several experimental studies, where it was clearly detected that, after shock wave exposures, the macromolecules of anticancer were introduced into the cells as their proliferation was decreased [4].

On the other hand, as cancer can be considered to be a disease of a series of genes, an important application for this method is gene therapy, where a nucleotide can be delivered into the cell by targeting a fundamental molecular defect [41].

Other important applications for this intracellular macromolecular delivery technique in cancer therapy involve the use of ribosome-activating proteins [42].

In any case, ESW chemotheraphy is a promising method for cancer treatment [20] as it increases the uptake of antibiotic agents into the cells. However, LSW treatment, in addition to possessing unique optical properties such as spatial and temporal coherency, minimum angular beam divergence, polarization and monochromaticity, may also provide a source of radiant energy of extremely high instantaneous power [37].

One of the many interesting effects induced by LSW that have been observed is the permeabilization of the plasma membrane [36]. Experiments have shown that LSW can also permeabilize the stratum corneum in vivo. The change of permeability is transient and the barrier function of the stratum corneum recovers within a few minutes.

The increased permeability allows macromolecules to diffuse through the stratum corneum into the viable epidermis and dermis. Furthermore, the LSW do not appear to adversely affect the viability or damage the structure of the skin [36].

In the case of use of bleomycin, an anticancer agent, it is clearly detected that after shock wave exposures it is introduced into the cells and their proliferation is found drastically suppressed [4]. bleomycin was introduced into the cancer cell through the process of perforations.

A extensive numerical study of these processes using *Molecular Dynamics* techniques has been done all along this PhD. That includes the modelling, equilibration, shock wave implementation and simulation for all the cases.

Even though the distribution of the phospholipids in the cell membranes does not seem to be random, a membrane can contain more than a 100 different species of these molecules. Therefore, a extremely precise modelling of this

kind of tissue is rather complicated and would reach the limits of *Molecular Dynamics*, however, simplier cases with only one specie were succesfully performed and the transient effect was simulated and numerically analysed (See 4.1.4).

1.4 The alveolar surface.

Alveolus-alveoli comes from the Latin word "alveus", which mean "little cavity". In anatomy, it refers to a structure with the form of a hollow cavity. In the case of the lung, the pulmonary alveoli, appearing at the end of the respiratory bronchioles, make gas exchange possible within the blood.

The way to the actual accepted model started with Von Neergaard [43], who introduced the concept that the force required to move gas into and out of the lungs is determined in part by surface tension at the interface between alveolar tissue and alveolar gas.

He also noted bubbles during deflation to low lung volumes but concluded that bubbles could not exist in vivo and rejected them categorically.

Pattle's discovery of lung surfactant [44] [45] was based essentially on the resistance of the lung bubbles to the foam and the low stable surface tension of the bubble films. Ideas recovered by Scarpelli [46] [47] were later used to develop the bubble films model.

However, Pattle considered that the surfactant was derived from the normal open alveolar lining and that bubble formation was an artifact of his laboratory manipulations, therefore he rejected that the bubbles existed in situ. These was reported subsequently by a few other investigators [48].

Finally, the characterisation of the bubble films [25] found in the alveolar structures revealed their properties:

1. Structural stability.
2. Natural formation.
3. Close apposition and potential mobility.
4. Low surface tension [49], [50] and [51].
5. Architectural position as alveolar infrastructure [52].

The studies in this matter are extremely complex and a definition of the agglomeration of bubble films in situ is needed. The liquid channels have been used to identify them in the experimental process [48].

The experiments were confirmed later after further expositions of the complexities of the surface network into the different publications:

1. Bubble and bubble foam film structure was validated for all kind of alveoli in vivo and in vitro [48] [53] [54] [55].
2. No evidence of free gas or open surfaces [53] [54].
3. Conducting airways from trachea to bronchioles contained free gas [53] [54].
4. Bubble films in fresh lung tissue were fluid [54].
5. The physical properties of the local fluid substrate that governed the bubble formation were relatively less significant [56] [55].
6. The liquid transfer between film channels was in the order of seconds [54] [55].
7. The studies of air drying revealed apparent continuity of the film liquid channels [48] [54] [55].
8. Bubble film conformations in situ were destroyed by analysis techniques, which explains, in part, why they have not yet been recognised [55].

In addition, the origin and transfer of forces involved in the respiration process have been assessed over the past century using all kind of measurements from gas flow or transpulmonary pressure to lung volume [57]. Even though such studies of the lung did not provide direct information about forces or transduction of forces operating at the cellular and subcellular levels, they yield an assumption of a continuous open layer for the alveolar surface layer.

This approach generated a variety of models to explain its mechanical behaviour [58] [59] [60] [61] [62] [63], but the models and their derivative theories cannot be sustained for a number of reasons [25] [64] [53] [54] [55]:

1. There is no documented continuous open surface layer in vivo yet.
2. Traditional laboratory methods destroy conformation of surfaces.
3. The idea that surfactants of the surface liquid form a single layer film at the open gas-liquid interface, lowering surface tension to near zero is tenuous [65] [46].

4. Normal bubble films have not been considered.

After all those studies and results, Scarpelli concluded that the alveolar surface liquid resides in continuous interconnected channels next to the alveolar bubble films into the so-called alveolar surface network or infrastructure [25].

The alveolar surface network is the agglomeration of gas bubbles, called foam, that aerates and mechanically supports the terminal lung units from respiratory bronchioles to alveolar sacs [25].

All these studies led to different models in order to explain the alveolar structure and operation and they are shown below.

- The bubble model [66].

  Widespread accepted for over 40 years, it works on the principle that the alveoli are normally covered with liquid forming an air-liquid interface with the alveolar gas, the only place where surfactant is assumed to be located as a surface of constant thickness.

  However, since the only stable liquid-gas interface, according to basic physics, is the sphere, this model could not explain alveolus as non-spherical structures.

- The morphological model [67].

  Starting from the point of surfactant thickness variation all along the alveolar surface, morphological studies led to the definition of concave fluid free areas as well as convex areas with excess of fluid.

  This model led to a self-regulating alveolar fluid control to resolve the accumulation of surfactant in the convex areas.

- The foam model [68].

  The alveolar surface, defined as an agglomeration of bubbles, fills the bronchioles end in the form of alveolar sacs. These are complete surfactants containing films which surround units of alveolar gas.

  This is opposite to the other two models which accept bubble segments or one-sided bubbles.

- The geodesic model.

  Opposite to the bubble model, where a continuous lining for the alveolar surface was implicit, a solid phase of DPPC is assumed. The surface activity of these lipids, identified in the lung in 1946 [69], was demonstrated in the 1920s [70].

In the process of expiration, the lipids of the membrane can come together in order to generate a solid geodesic dome rigid structure [71] while they can expand in inhalation.

Chapter 2

Molecular Dynamics method

The forms of matter which can be studied may be large, or they may be far too small to be seen by the most high-powered microscopes available. Such is the realm of *Molecular Dynamics*, the study and simulation of molecular motion.

Molecular Dynamics exists as well at the borders between physics and chemistry providing understanding regarding the properties of matter, including phenomena such as the liquefaction of gases, in which one phase of matter is transformed into another.

This method, which makes it possible to define matter at an atom level, considers any material, tissue or molecule as a sum of particles.

It was English chemist John Dalton (1766-1844) who first recognised that nature is composed of tiny particles. This concept was adopted from the Greek philosopher Democritus (470-380 BC), who proposed that matter is formed out of tiny units he called "atomo" (unable to be cut).

Molecular Dynamics is a form of computer simulation, wherein atoms and molecules are allowed to interact for a period of time under known laws of physics. It represents an interface between laboratory experiments and theory, and can be understood as a "virtual experiment" which, nowadays, is regarded as a well accepted tool, alternative to *Monte Carlo* method, for studying a wide variety of phenomena.

2.1 Description.

As its name suggests, *Molecular Dynamics*, from the dynamics point of view, can be the study of why objects move as they do into a potential field. Meanwhile, as it is thermodynamically affected, it will give information about the relationships between heat, work and energy.

By solving Newton's equations of motion numerically and applying them to a finite number of particles into a system, once you know the properties of the particles for a particular time t_0, their evolution can be integrated in time and space as an initial value problem. This approach provides a suitable tool for the study of many processes when the dynamics of every single particle can be obtained for each time step into the *Molecular Dynamics* volume, and further calculations and analysis can be done.

The particles in the system, assumed as spheres, can have different numerical properties depending on the kind of *Molecular Dynamics* simulation to be carried out. In the case of atomic models into an electrostatic field, a particle is defined by its position, velocity, radius, mass, charge and bonds.

$$f(\epsilon_k) = \frac{2}{\sqrt{\pi}} \cdot \frac{1}{(k_B \cdot T)^{\frac{3}{2}}} \cdot \sqrt{\epsilon_k} \cdot e^{-(\frac{\epsilon_k}{k_B \cdot T})} \tag{2.1}$$

The chemical structure of the molecules can be obtained from their crystal structure, providing the relative position of the atoms in a particular molecule and a random Boltzman distribution (Equation 2.1) can be used to generate the initial velocities field.

Once the properties of the particles for a particular time are known, the interactions among them can be calculated.

2.2 Equations.

The potential function presented as an equation 2.2 can be used to determine the force applied to each atom, as forces and potentials can be related by the equation 2.3.

$$
\begin{aligned}
U(\vec{R}) &= \sum_i k_i^{bonds} \cdot (r_i - r_0)^2 + \sum_i k_i^{angles} \cdot (\Theta_i - \Theta_0)^2 \\
&+ \sum_i k_i^{dihedrals} \cdot [1 + \cos(n_i \cdot \phi_i + \delta_i)] + \sum_i k_i^{impropers} \cdot (\omega_i - \omega_0)^2 \\
&+ \sum_i \sum_{i \neq j} 4 \cdot \epsilon_{ij} \cdot \left[\left(\frac{\sigma_{ij}}{r_{ij}} \right)^{12} + \left(\frac{\sigma_{ij}}{r_{ij}} \right)^{6} \right] + \sum_i \sum_{i \neq j} \frac{q_i \cdot q_j}{\epsilon \cdot r_{ij}}
\end{aligned}
\tag{2.2}
$$

The total value of the potential, $U(\vec{R})$, is the sum of 6 terms, where "bonds" counts each covalent bond in the system, "angles" are the angles between each pair of covalent bonds sharing a single atom at the vertex, and "dihedral" describes atom pairs separated by exactly three covalent bonds with the central bond subject to the torsion angle, "improper" dihedral refers to a geometry of four planar, covalently bonded atoms and the last two terms calculate the values for van der Walls interaction and electrostatic potential respectively [72].

$$
\vec{F}_i = m_i \cdot \frac{d^2 \vec{r}_i}{dt^2} = -\vec{\nabla} U(\vec{R}) \tag{2.3}
$$

This scheme leads to a set of coupled 2^{nd} order differential equations that can be propagated in time using the verlet algorithm [73] described in equation 2.4.

$$
\begin{aligned}
x(\Delta t) &= x(0) + \dot{x}(0) \cdot \Delta t + \ddot{x}(0) \cdot \frac{\Delta t^2}{2} + O(\Delta t^3) \\
\dot{x}(\Delta t) &= \dot{x}(0) + [\ddot{x}(0) + \ddot{x}(\Delta t)] \cdot \frac{\Delta t}{2} + O(\Delta t^3)
\end{aligned}
\tag{2.4}
$$

As the second time derivative depends on the first, the $\dot{x}(\Delta t)$ can be determined iteratively using equation 2.4, losing reversibility, though.

2.3 Ensembles.

The equations of motion are not modularly invariant, which makes the simulation dependent of the *Molecular Dynamics* cell definition, but, in the case of

isobaric schemes, modular invariance can be incorporated into a fully flexible cell [73].

The temperature can be related to the velocity field using the Boltzman constant as equation 2.5 points out.

$$E_c = \sum_i \frac{1}{2} \cdot m_i \cdot v_i^2 = \frac{3}{2} \cdot N \cdot k_B \cdot T \tag{2.5}$$

Using a modified Nose-Hoover method [73] in which Langevin dynamics are used to control fluctuations, combined with a method of temperature control, a constant particle number, pressure and temperature (NPT) ensemble can be simulated.

$$P = \frac{N \cdot k_B \cdot T}{V} \tag{2.6}$$

This NPT ensemble makes it possible to set to a target value both the temperature and pressure values, as the boundary dimensions of the system are allowed to change and the pressure is related to the volume through equation 2.6.

In this way, the Langevin piston Nose-Hoover method is a combination of the Nose-Hoover constant pressure method [74] with Langevin dynamics volume fluctuation control which carries out an isobaric-isothermal (NPT) ensemble [75]. The Langevin equation for a cubic cell results in:

$$\begin{aligned} \dot{r}_i &= \tfrac{p_i}{m_i} + \tfrac{1}{3} \cdot \tfrac{\dot{V}}{V} \cdot r_i \\ \dot{p}_i &= f_i - \tfrac{1}{3} \cdot \tfrac{\dot{V}}{V} \cdot p \\ \ddot{V} &= \tfrac{1}{W} \cdot [P(t) - P_{ext}] - \gamma \cdot \dot{V} + R(t) \end{aligned} \tag{2.7}$$

where, the γ is the collision frequency and $R(t)$ is a random force taken from a Gaussian distribution with zero mean and variance [75] as a result of solvent interaction.

The Langevin equation can be integrated using the Brünger−Brooks−Karplus (BBK) method, which refers to a natural extension of the Verlet method for the Langevin equation and can be expressed as:

$$\begin{aligned} r_{n+1} &= r_n + \frac{1-\gamma\cdot\frac{\Delta t}{2}}{1+\gamma\cdot\frac{\Delta t}{2}} \cdot (r_n - r_{n-1}) \\ &+ \frac{1}{1+\gamma\cdot\frac{\Delta t}{2}} \cdot \Delta t^2 \cdot \left[M^{-1} \cdot F(r_n) + \sqrt{\frac{2\cdot\gamma\cdot k_B\cdot T}{\Delta M}} \cdot Z_n \right] \end{aligned} \tag{2.8}$$

where, Z_n is a Gaussian random value of zero mean and variance 1 set for each dimension [72].

When there is no pressure or temperature control, and the equations are followed as described in section 2.2, the ensemble is called microcanonical or NVE, as the number of particles, the volume and the energy are kept constant.

2.4 Bonded interactions.

The first four terms of the potential equation refer to different molecular interactions described in figure 2.1, namely: bonded, rotation, dihedral and improper.

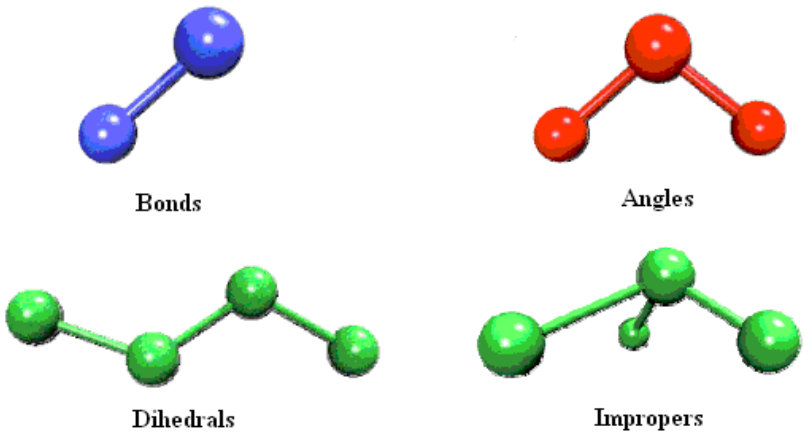

Figure 2.1: Molecular structures.

The molecular different structures, namely:

- Bonds: Covalently bonded atoms.
- Angles: Two bonds which share a common atom form an angle.
- Dihedrals: Two angles which share a common bond form a dihedral.
- Impropers: Any planar group of four atoms forms an improper.

depend on the relations between the particles part of model which have to be defined for the *Molecular Dynamics* model before undertake the simulation.

2.5 Non bonded interactions.

The fifth and sixth terms in the potential equation define the non-bonded interaction of the particles in the *Molecular Dynamics* model. These are van der Waals and electrostatic.

These kinds of interaction are calculated using a non-bonded pair list which contains all pairs of atoms for which non-bonded interactions should be calculated. The search for pairs of atoms which should have their interactions calculated is an expensive operation, so the pair list is only calculated periodically in order to reduce computation time.

Van der Waals interactions, often truncated at a cutoff distance abruptly, can be calculated using a smooth switching function shown in figure 2.2. This function will be used to truncate the van der Waals potential energy smoothly at the cutoff distance, otherwise the energy may not be conserved.

However, the handling of electrostatics is slightly more complicated due to the incorporation of multiple time stepping for full electrostatic interactions. There are two cases to consider, one where full electrostatics are employed and the other where electrostatics are truncated at a given distance.

When electrostatics are truncated at the cutoff distance, all electrostatic interactions beyond a specified distance are assumed to be zero, so rather than having a discontinuity in the potential at the cutoff distance, a shifting function is applied to the electrostatic potential as pointed out in figure 2.3. The shifting function shifts the entire potential curve so that the curve intersects the x-axis at the cutoff distance.

In the case of full electrostatics, the interactions are not truncated at any distance. The cutoff parameter represents the local interaction distance. Out-

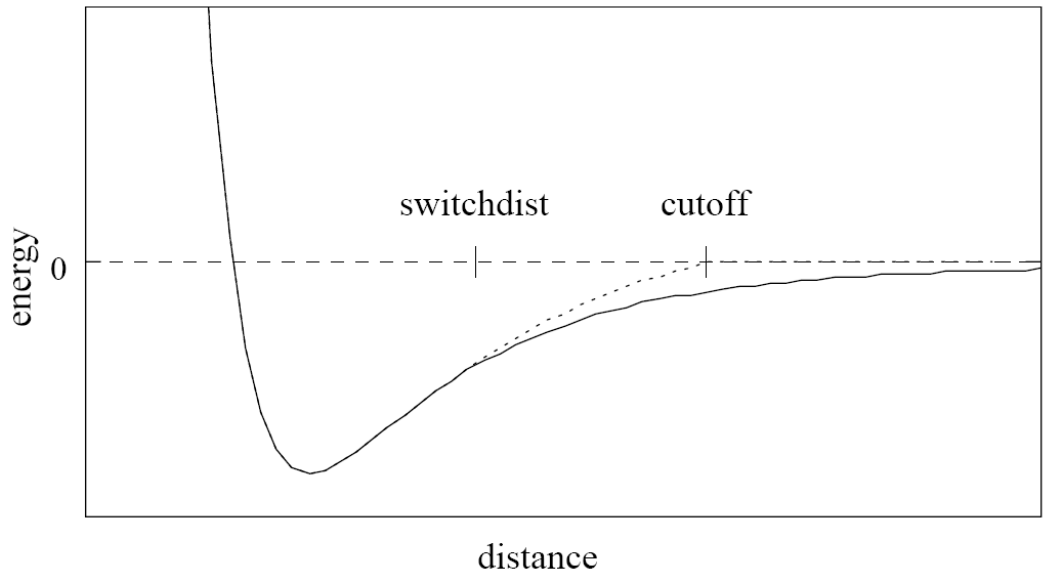

Figure 2.2: Switching function.

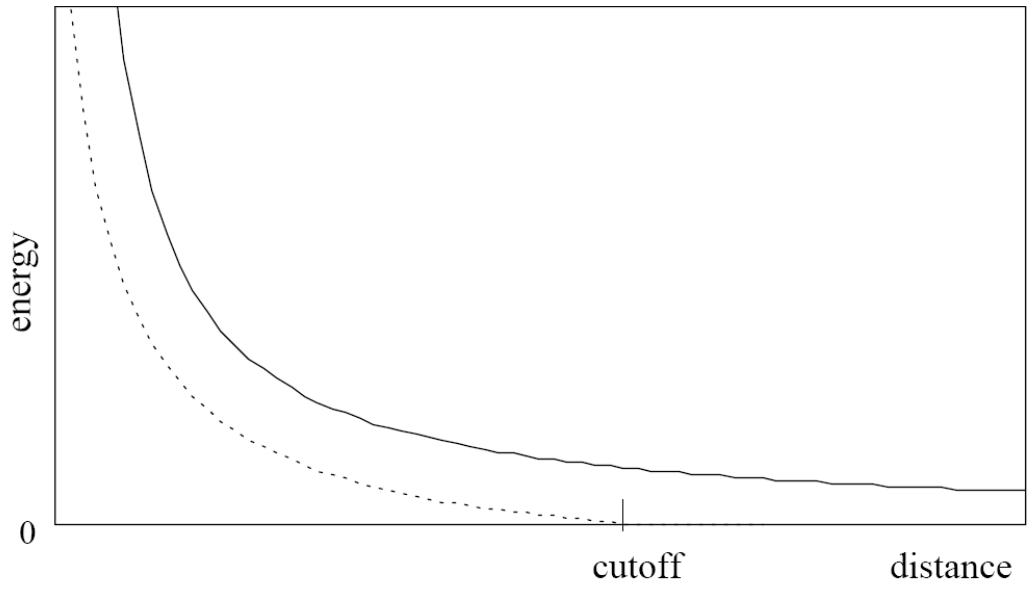

Figure 2.3: Electrostatic potential.

side this distance, interactions will be calculated only periodically to save calculation time.

In the case of our simulations the value of the cut-off distance has been

set to 10 Å following the instructions written in NAMD package manual and tutorials [72].

2.6 Limitations.

The limitations of the *Molecular Dynamics* method are very well documented from a theoretical point of view.

The first limitation is about the potential function, shown in equation 2.2, which has several options. In particular, different forms for the van der Waals interactions and the dihedrals are in common use [76].

Another limitation of the *Molecular Dynamics* calculations is about the maximum time step that can be used for the integration of the equations of motion, which is limited to a few microseconds. This means a rather computationally expensive integration to obtain only a few nanoseconds of simulation. Likewise, the size of the model increases the time per integration step, so it must be limited to a few nanometres in order to decrease the simulation time and to not cause impractical delays.

Finally, the major limitation is the classical treatment of the system, which makes it impossible to consider chemical reactions without describing at least part of the system dynamically, but that is currently of no consequence in simulations of phospholipid systems [76].

From a practical point of view, it is not at all trivial to choose the volume of the system, usually a cube, when carrying out an NVE ensemble, as the properties of the constituents in the model are usually available in the bulk, but they are not for the *Molecular Dynamics* cell which has dimensions in the order of a few nanometres.

This can be expressed as follows: The population of the planet Earth is about 6,450 million people, who live in about 149 million km^2. Cranfield University campus area is about 3 km^2, so its whole population should be $\frac{6450 \cdot 3}{149} \approx 130$ people. However, in Cranfield University Annual Report 2007, you can read that the number of students on Campus is 1,548, which is a distance away from our bulk interpolation, particularly when the non-student population is not included in this number.

That makes it necessary to find a way to carry out other ensembles where

the dimensions of the cell can be adjusted and, at the same time, set other magnitudes to target values [75].

2.7 Computations.

NAMD [1] [72], a parallel *Molecular Dynamics* code designed for high-performance simulation of large biomolecular systems, has been used to execute the different simulations of the membrane models (See chapter 3).

The velocity verlet 2.4 integration method is used to advance the positions and velocities of the atoms in time, and by using periodic boundary conditions, strong artefacts from the presence of boundary planes [76] are avoided.

The local interactions (bonded, van der Waals and electrostatic interactions within a specified distance) are calculated at each time step, but the longer range interactions (electrostatic interactions beyond the specified distance) are computed periodically less often.

This way of computation reduces the cost of computing the electrostatic forces over several time steps and a smooth splitting function is used to separate a quickly varying short-range portion of the electrostatic interaction from a more slowly varying long-range component.

As the fastest motions within the lipid bilayer, which include diffusion and orientational correlation of water, occur on a time scale up to a few picoseconds (ps) [76], a time step set to 1 femptosecond (fs) is a fair value, while non bonded interactions are calculated every 2 fs and full electrostatics every 4 fs.

This triple time step procedure is used to reduce the computational cost to acceptable values, so longer computations can be achieved.

In order to run a *Molecular Dynamics* simulation, the parameters for the potential function and the initial values must be provided. In the case of NAMD, the values for the parameters can be obtained from the different publications into Prm format files; The initial values for position and velocity of the atoms can be read from generated Pdb format files and the structure definition of the molecules involved has to be described into Psf format files (See

[1] NAMD was developed by the Theoretical and Computational Biophysics Group in the Beckman Institute for Advanced Science and Technology at the University of Illinois at Urbana-Champaign.

http://www.ks.uiuc.edu/Training/Tutorials for more information).

Chapter 3

Biological membrane modelling

The study of the biological membranes using *Molecular Dynamics* techniques has been getting extremely good results in the field of biology for a few years as a result of the technological advances in the computer industry, which let the researchers run models with thousands of particles in acceptable times.

In this chapter, different models will be presented: Models for biological cell membranes, as described in section 1.1, using different kind of lipids; a model for the alveolar surface, which, even though it consists mainly of a lipid membrane, cannot be referred to as a bilayer but a completely different structure from a biological point of view (See section 1.4).

All these models will be used in the next chapters for the *Molecular Dynamics* simulations presented in this document.

3.1 Generation of the models.

The generation of the *Molecular Dynamics* models for the membranes is a difficult process which needs to be studied carefully as the results are highly affected by the initial positions of the particles involved.

It is possible to use an external plugin included into the VMD package called "membrane" (See Membrane plugin) to generate the hydrated membrane and more water can be added later using another included package called "Solvate" (See Solvate plugin).

This way of generation worked fairly well for the POPC models used in this study as the position of the particles and the generation of the water layers have a previous development in order to find the conformation of this king of biological structures.

By the other hand, if it is not possible to find previous models made by other authors or the these plugins can not produce the desired model, then, it will have to be done manually placing the molecules in their position. It usually requires some programming and developing in order to do the generation and, probably, different attempts until a valid model is found.

This last way of doing *Molecular Dynamics* with biological membranes requires the exact definition of the position for all the particles in the model. They can be set to match experimental values of thickness and area per lipid as possible, but a general rule can not be concluded from that advice as sometimes giving higher values for this these parameters before the minimization and equilibration process makes the particle find their natural position easily avoiding steric effects.

3.2 The cell membrane.

3.2.1 POPC bilayer.

Even though the distribution of the lipids in the cell membranes does not seem to be random, a single membrane can contain more than a 100 different species of these molecules. The reason for this heterogeneity is not known. However some can be considered: Generation of a stable membrane for the embedded proteins, their shape steadies the curvature, biosynthetic pathways, regulatory agents, enzyme activities, cell growth regulation... [77]

The POPC molecule [78] [79] [80] consists of a complex structure of 134 atoms including Carbon, Hydrogen, Nitrogen, Oxygen and Phosphorus.

The lipid heads have been properly hydrated using water molecules [81]. The model for fluid water has the following characteristics (See Solvate plugin):

- Irregularly-shaped volumes, adapted to the structure.
- Minimal boundary-distance is guaranteed.

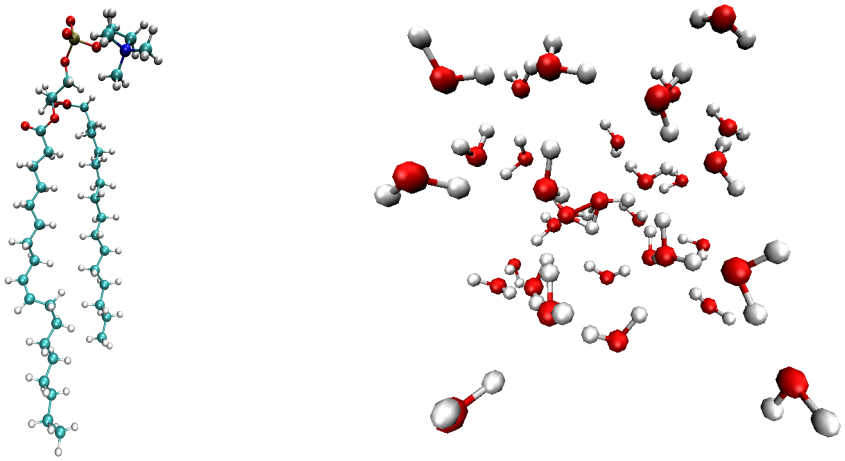

(a) POPC phospholipid.

(b) Disordered fluid water.

Figure 3.1: 3D structure of the molecules involved in the POPC bilayer.

- It is generated as disordered (fluid) water, not a grid of water molecules (i.e., ice).
- The positions of all water molecules are minimised.

For the studies on POPC, a rectangular lattice of hydrated lipids was generated using VMD package [82]. The model consists of 21,555 atoms with 66 POPC bilayer lipids and 4,237 water molecules.

The lipid tails, pointing inside the lipid membrane, are almost fully extended in order to reduce the minimisation time. The distance between the layers was set around the membrane thickness and the lattice period was set around the lipid membrane density.

To make the generated structure more realistic, some disorder was introduced into the position of each lipid in the membrane plane and more disorder was caused by a short (1ps) minimisation in the vacuum, eliminating possible steric collisions among the lipid atoms (See Membrane plugin).

You can find much more detailed information about the computational set-up of this membrane in Appendix I at the end of this document.

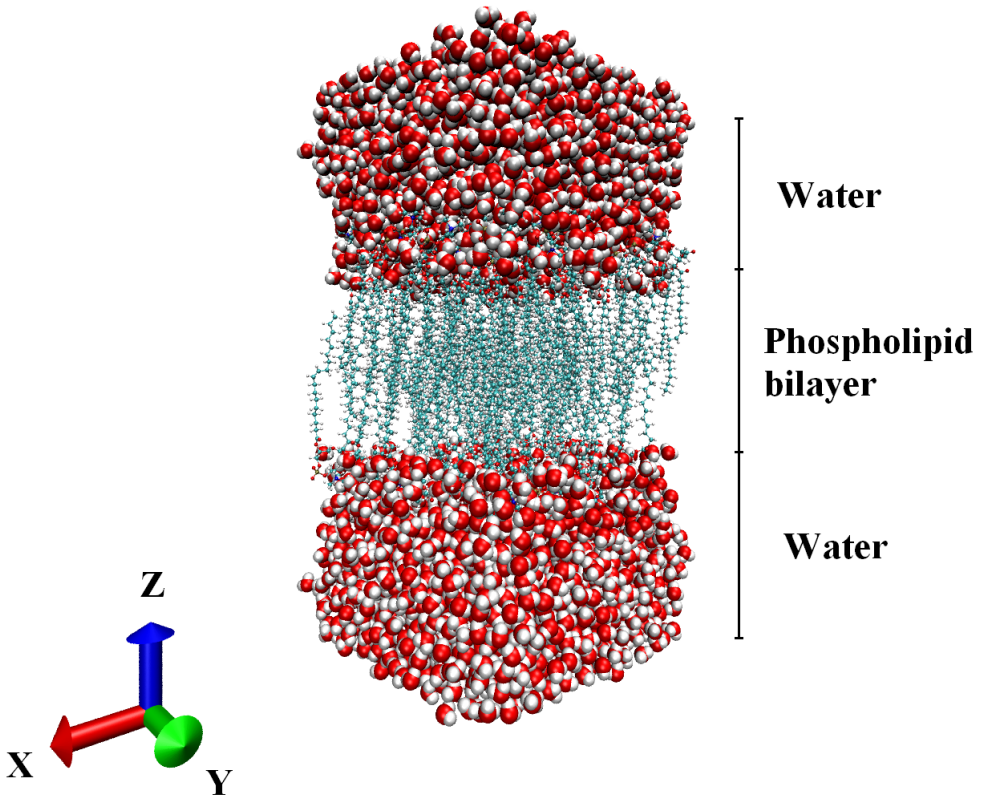

Figure 3.2: *Molecular Dynamics* model for the POPC membrane.

3.2.2 Other bilayers.

With the same model for the water used in subsection 3.2.1, another four different models of hydrated cell membranes were developed. The 3D structure of the lipids used for the bilayers is shown in figure 3.3.

Adjusting the thickness and area per lipid as much as possible for each bilayer, a lattice with constant separation among the lipids was used as an initial condition this time. A small displacement between the layers was introduced to stabilise the membrane across the minimisation process and a random roll around the intrinsic axis of each single lipid was produced.

All these models consisted of 128 phospholipids (2 x 64) with 12,173 molecules of water.

The figure 3.4 represents the model of the bilayer for the DMPC lipid.

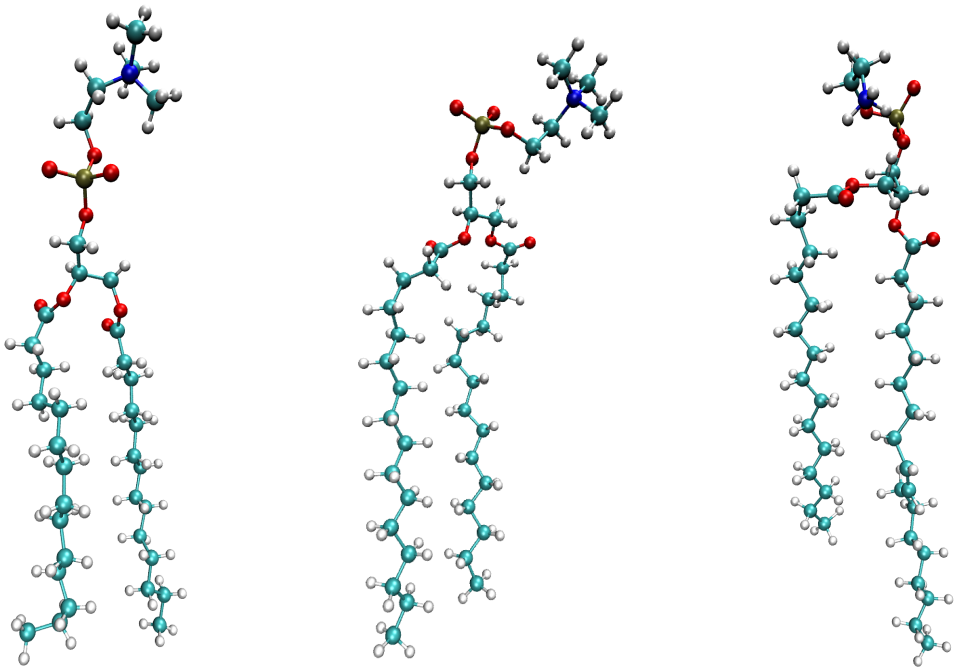

(a) DMPC. (b) DPPC. (c) POPE.

Figure 3.3: 3D structure of the lipids involved in the different bilayers.

The figure 3.5 represents the model of the bilayer for the DPPC lipid.

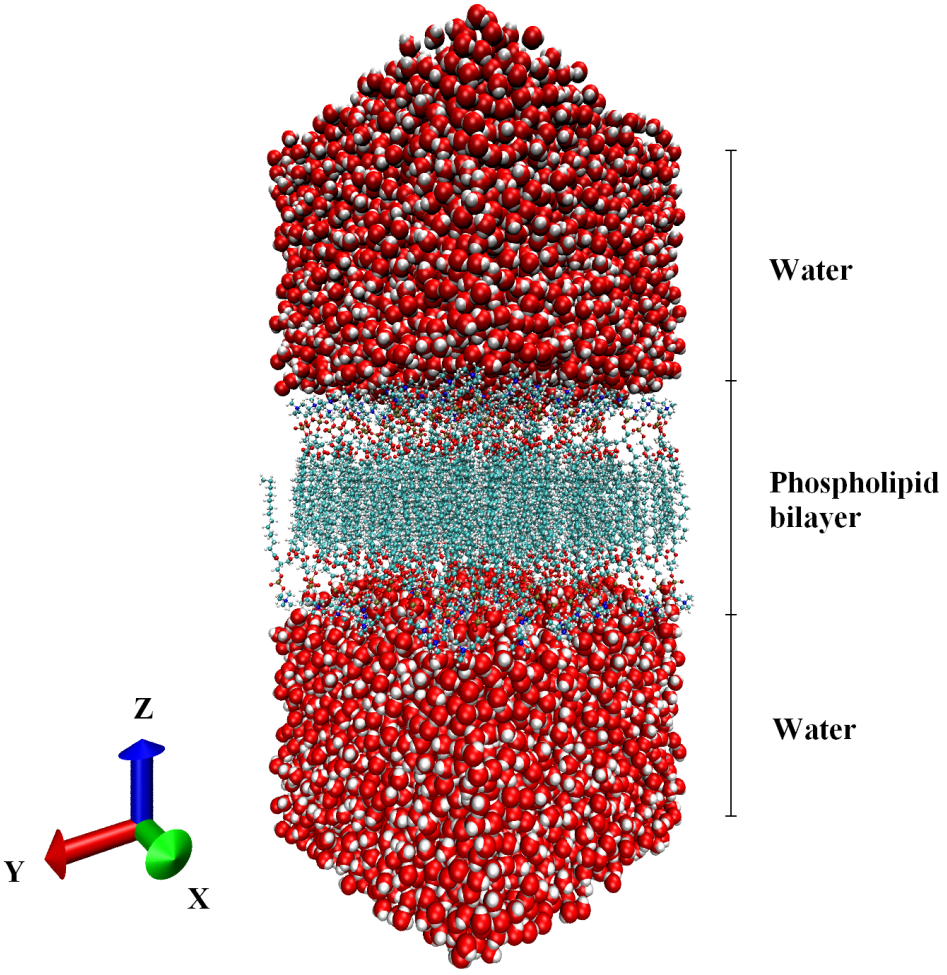

Figure 3.4: *Molecular Dynamics* models for the DPMC bilayer.

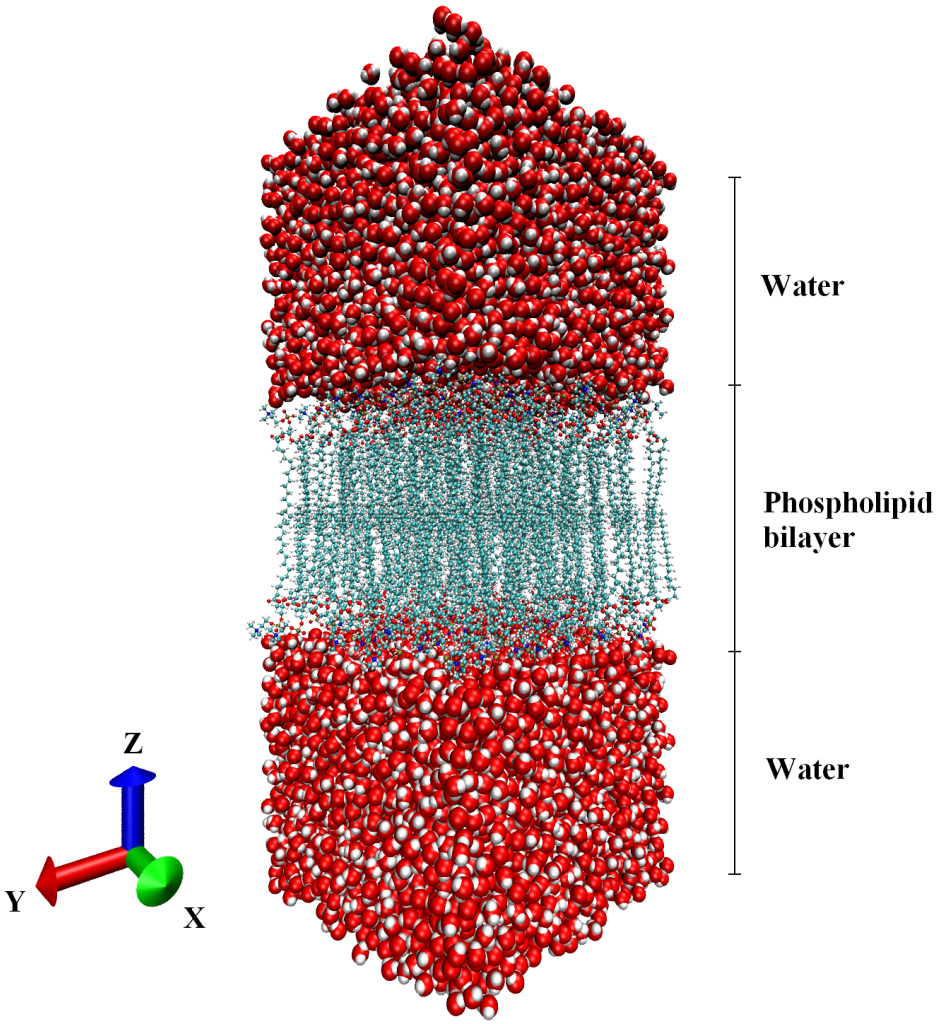

Figure 3.5: *Molecular Dynamics* models for the DPPC bilayer.

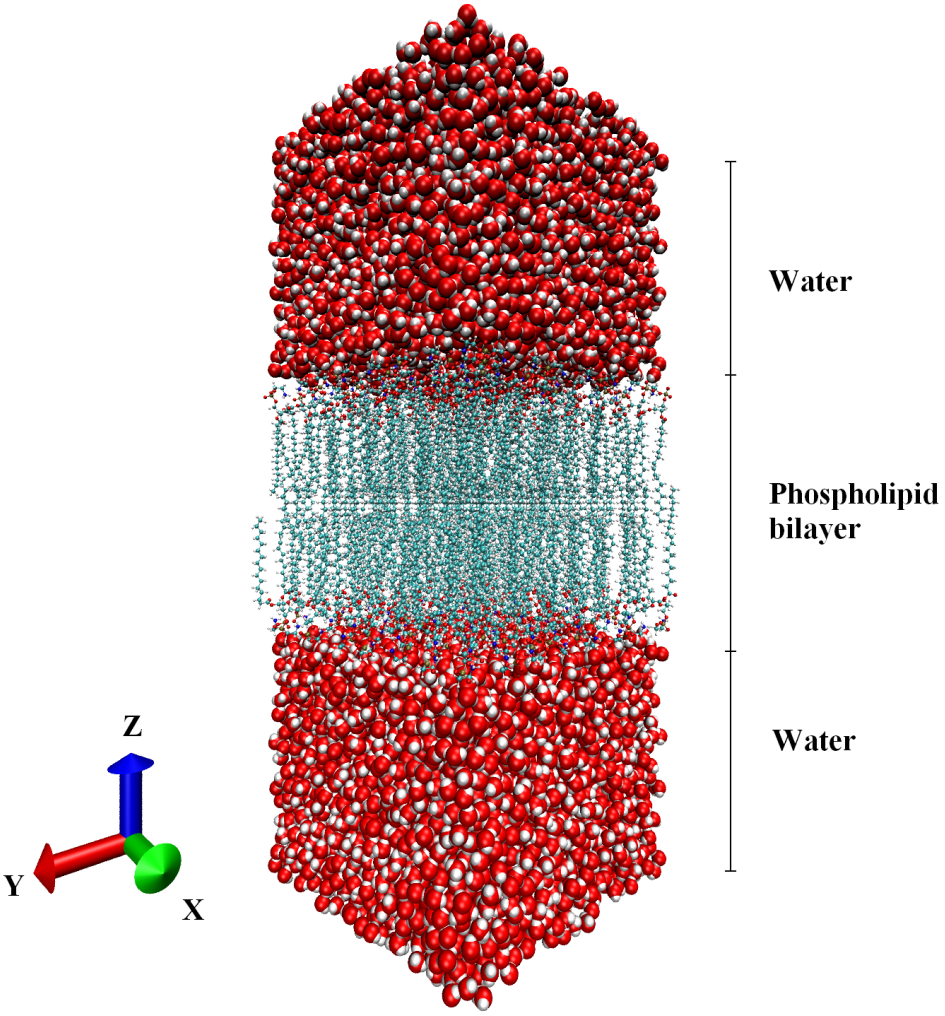

Figure 3.6: *Molecular Dynamics* models for the POPE bilayer.

The figure 3.6 represents the model of the bilayer for the POPE lipid.

3.3 The alveolar surface.

Even though the alveolar surface consists mainly of DPPC, unsaturated phosphatidylcholine(PC) and phosphatidylglycerol(PG), cholesterol and proteins [83], and apart from all the controversy commented on in section 1.4 and chapter 5, it can be considered as a DPPC layer where the hydrophilic tails of the lipids are in contact with the gas, while the hydrophilic heads are usually hydrated by fluid.

The fluid will not be modelled this time and the hydrophilic heads of two alveolar DPPC layers will be in contact while the gas will be placed in contact with the hydrophobic tails. This structure can not be considered as a bilayer at all as each layer belongs to a different alveolus.

The surfactant is a protein embedded in the alveolar layers which has two main characteristics: Rapid adsorption to an air-water interface to form surface active films and reduction of the surface tension facilitating the gas flow throw the DPPC layers.

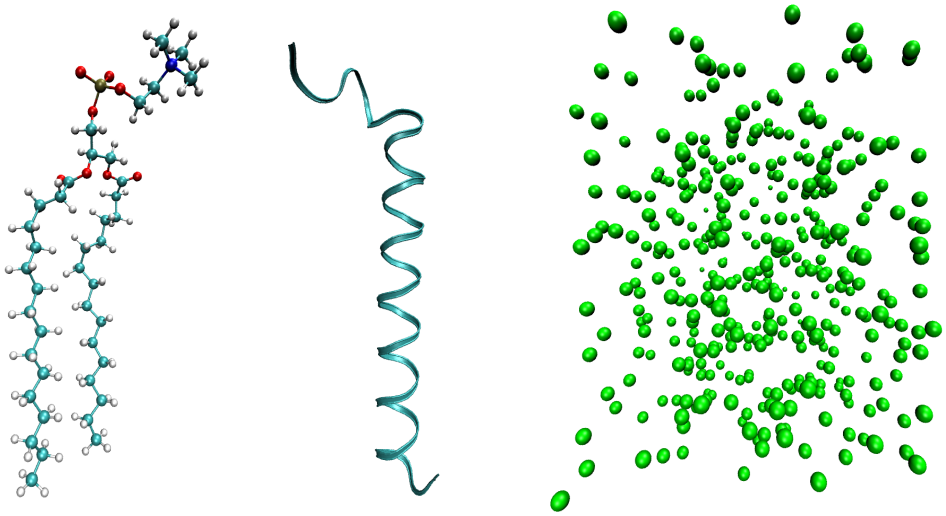

(a) DPPC phospholipid. (b) Surfactant. (c) Air particles.

Figure 3.7: 3D structure of the molecules involved in the alveolar surface.

In order to obtain more realistic results (See 1.4), these types of proteins have been included into the simulation model. The structure of the molecules involved in the *Molecular Dynamics* model are shown in figure 3.7.

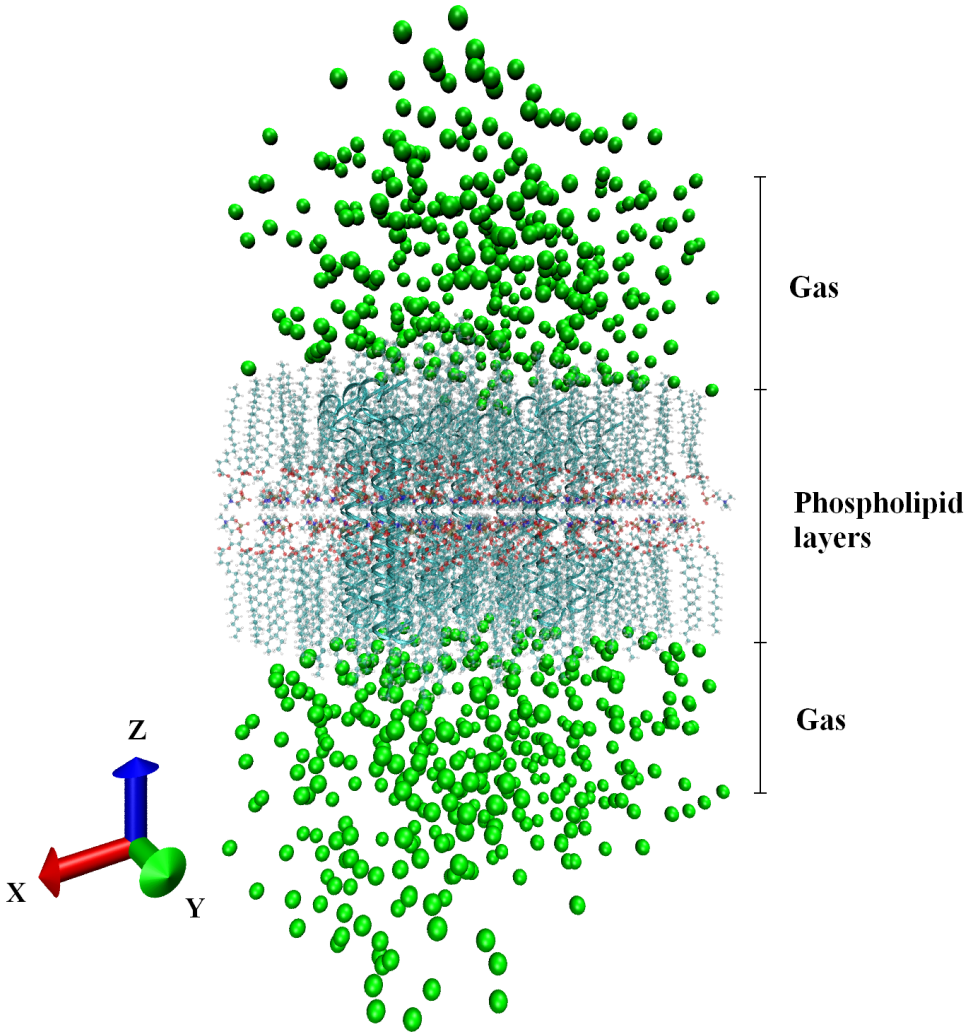

Figure 3.8: *Molecular Dynamics* model for the alveolar surface.

The model (Figure 3.8) consists of 790 air particles [84], 2 DPPC layers [78] [79] [80] with 64 molecules each and 16 molecules of surfactant [85] [86], which have been randomly embedded into the layers removing the overlapping lipids. The made model has an area of 10 x 8 nm.

You can find much more detailed information about the computational set-up of this membrane in Appendix II at the end of this document.

Chapter 4

Shock wave interaction with a biological membrane

This part of the document will present how the *Molecular Dynamics* techniques can be used to analyse the interaction of a single shock wave with a biological cell membrane. Two different ensembles, the NPT and NVE, will be highlighted.

The NPT ensemble will simulate the transient process of the lipid membrane after the shock wave application, while the NVE ensemble will not be sensitive to that.

On the other hand and as it would be expected, many more *Molecular Dynamics* simulations have been performed during the time spent on this doctoral study in other to achieve a precise comprehension and tune up of this bioengineering phenomenon, sometimes with greater accuracy than others. With these simulations, several tries with cell membrane bilayers of DPMC, DPPC and POPE were computed using Cranfield University HPC facilities when available. Their computational cost made the tune up impossible, so the results were not as satisfactory as the researcher would have wished.

By the other hand, a lot of time was used to generate appropriate *Molecular Dynamics* models of the different membranes. In this process, the initial area per lipid, the separation and thickness of the layers or the number of molecules make the simulation success or fail.

In case of failure, the membrane does not stay together any more and the lipids separates mixed with the other molecules in the model after the

application of the shock wave. This kind of result does not make any sense if the whole cell membrane, as a sphere-shaped structure, is taking into account.

4.1 The NPT ensemble

This computation was the initial idea for the study of the shock wave interaction with the biological cell membrane and it was made with a 32 bit single 3.00 GHz processor desktop computer with 1.00 GB of RAM. This is a very limited resource for a *Molecular Dynamics* simulation, nevertheless, as it is said in Spain, "La paciencia es la madre de la Ciencia" (Patience is the mother of science), and the computations were successfully computed after some time.

The NPT ensemble for a POPC membrane, which will be described next, achieved rather good results which were validated and published in the International Journal for Numerical methods in Fluids, 2007.

4.1.1 Minimisation.

In the case of molecular systems, the number of local minima and the cost of computations make the search for the energy minimum completely unapproachable. However, a local minimum in the neighbourhood of the x-ray structure used as the initial position for the atoms can be easily examined. This process can be performed in order to relieve strain in experimentally obtained conformations [87]. Therefore before carrying out the simulation, a minimisation can be computed to reach an initial equilibrium range for the system.

This process is based in a sophisticated conjugate gradient and line search algorithm performance, which can select successive search directions from the initial gradient and eliminate repeated minimisation along the same directions. Once a minimum is rigorously bounded, the conversion can be made using a golden section search or, when gradient information is available, a quadratically convergent method.

For this simulation, the minimisation was done for 50 ps in three stages described as follows:

1. Minimisation for 1000 femptoseconds (fs).

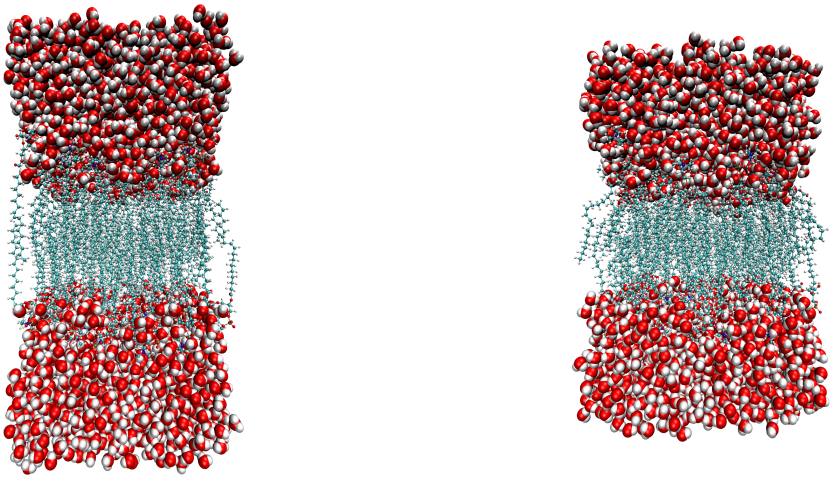

(a) Initial condition.

(b) End of minimisation, after 50 ps.

Figure 4.1: NPT minimisation.

2. Temperature increasing for 1000 fs.
3. Pressure increasing for 3000 fs.
4. Volume equilibration for 45000 fs.

4.1.2 Shock wave implementation.

A study of cell permeability suggested that the use of shock waves may be a way to introduce macromolecules and small polar molecules into the cell cytoplasm as they may increase the membrane lipids' diffusion. In this study, each shock wave source leads to a different shock wave form, so it was uncertain which shock wave parameters were important for the uptake as it did not depend on the peak pressure of the shock waves [13].

It was concluded that the impulse (I_p) of the shock wave, rather than the peak pressure, was the dominant factor for increasing the diffusion into living cells. This impulse can be mathematically defined as:

$$I_p = \int_0^{2 \cdot R_t} P \cdot dt \tag{4.1}$$

Therefore, a single shock wave, applied downwards to a part of the water layer, can be characterised by an impulse which can be expressed with an increase in the velocity (V_z) that will lead to a change in the momentum of the upper water layer.

$$V_z = \frac{I_p}{M} \cdot A \tag{4.2}$$

Using this value of velocity (V_z) [23], several simulations have been performed with impulses in the range of 0.0 to 40.0 $Pa \cdot s$. These values are comparable to those provoked by lasers in different experiments and published by other authors [13] [88].

In water, the rise time of a shock wave is a few picoseconds, corresponding to a shock front thickness of a few nanometers [31], however, from experimental studies it is known the shock wave has a rise time of about 30 ns after propagation of a distance of 800 μm [36].

In any case, those values are in an order of magnitude over the time and scale limits of the *Molecular Dynamics* simulations undertaken in this study, therefore the whole wave will not fit into the simulations which run for around 0.3 ns in a model of around 0.1 nm, but a part of the front wave at the very top of the model will be included.

4.1.3 Simulation.

Once the model is minimised and the shock wave calculated, the latest coordinates and velocities of the atoms just after the impulse can be used as initial conditions for the simulation.

In the case of having a null impulse ($I_p = 0.0 Pa \cdot s$), a standard *Molecular Dynamics* simulation, which will serve to compare and validate the experiment, is computed (Figure 4.2).

As the stability of the lipid bilayer system is susceptible to the starting conditions [89], analysis of the variables result of the calculation is needed to verify its reliability. In this simulation, the stability is assured as the quantities of the variables involved just fluctuate around certain values in their range as will be described within this document. The simulations run for 200 ps and their reliability will have to be validated.

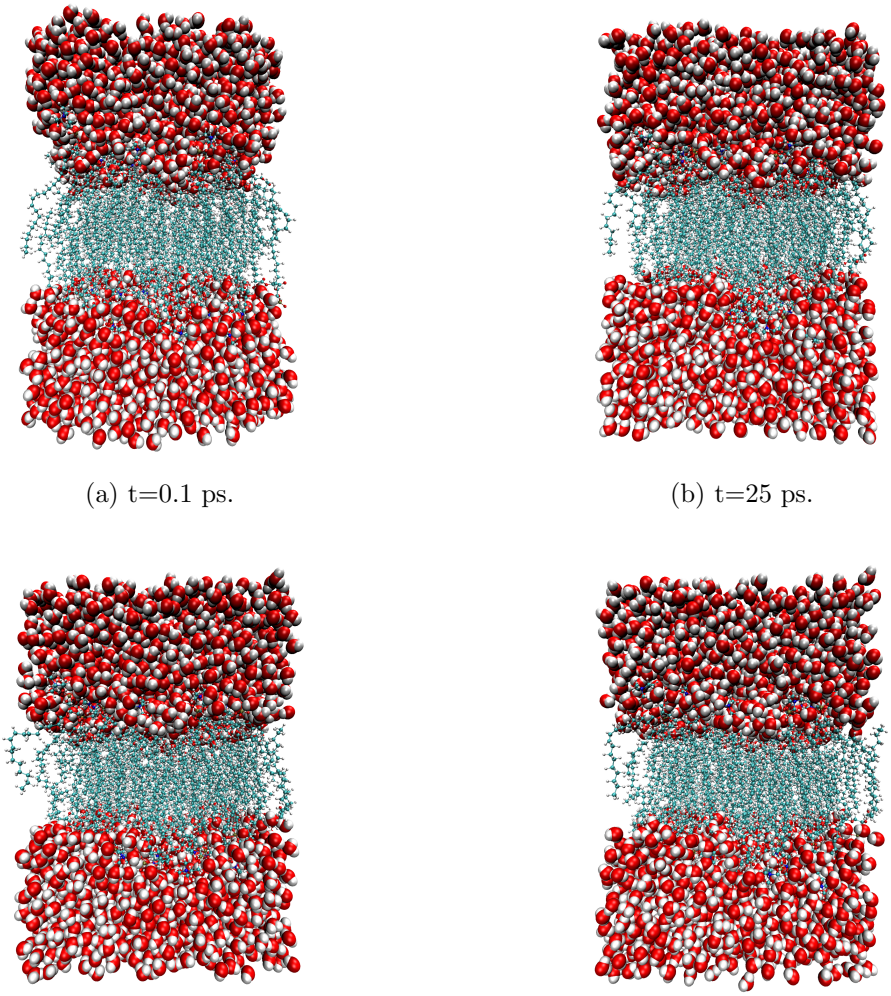

(a) t=0.1 ps.

(b) t=25 ps.

(c) t=50 ps.

(d) t=75 ps.

Figure 4.2: NPT simulation without shock-wave.

The simulations for positive values of the shock wave, which have also been calculated, are original, so they will not serve for calculus validation, but for increasing our knowledge in this interaction which is not yet well understood.

The membrane remains stable for all the intensities of the shock wave from Ip = 8 to 40 $Pa \cdot s$ as it can be seen in figure 4.3.

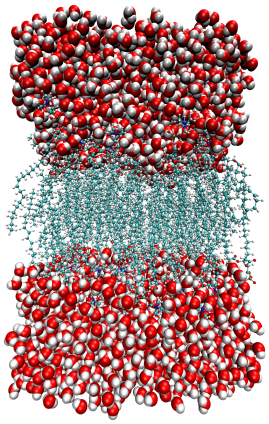

(a) t=0.1 ps.

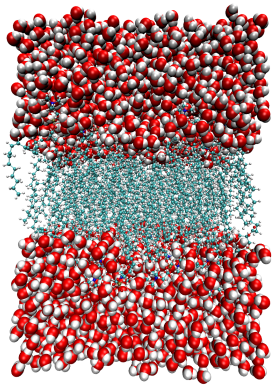

(b) t=25 ps.

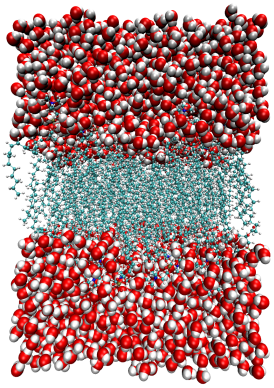

(c) t=50 ps.

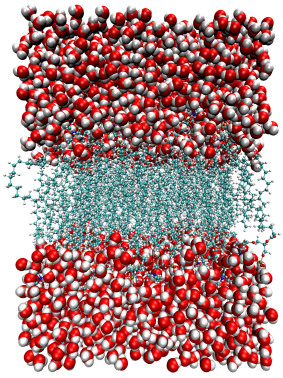

(d) t=75 ps.

Figure 4.3: NPT simulation with a shock-wave of Ip = 40 $Pa \cdot s$.

4.1.4 Analysis.

It is often supposed that determining the bilayer structure by diffraction means doing crystallography, however, fully hydrated lipid bilayers are not even close to being in a crystalline state. The contrast is strongest for bilayers that are in the fluid phase where the hydrocarbon chains are disordered in contrast to the nearly all-trans chains in lipid crystals.

These differences are not surprising since there is much more water in fully

hydrated lipid bilayers. This substantially alters the balance of interaction energies of the bilayers compared to the nearly dry crystalline state and also allows for increased fluctuations [90].

According to the kinetic theory of matter, all the particles in the model must be in constant motion and their position, calculated by solving the equations exposed at the beginning of the document, changes all along the simulation time.

After the simulations are computed, the results can be processed and analysed. In a step further, some different regressions have been calculated in order to obtain the trend which is chosen from linear, exponential, logarithmic or double-log functions.

Kinetic energy.

As the shock wave generates a sudden increment in the velocity value of the upper water layer, the kinetic energy (E_k), which is calculated using equation 4.3, will be increased proportionally to the intensity of the impulse.

$$E_k = \sum_i \frac{1}{2} \cdot m_i \cdot v_i^2 \tag{4.3}$$

The produced system imbalance lasts only for a few picoseconds. After that, the values come back to equilibrium and fluctuate in their range until the end of the simulation. This behaviour of the membrane points out the transient effect of the shock wave which will be noticed in other values as well, as discussed in subsequent sections.

The maximum values for this variable occur when the shock wave is applied and they are shown in the table below.

Impulse ($Pa \cdot s$)	$I_p = 0$	$I_p = 8$	$I_p = 16$	$I_p = 24$	$I_p = 32$	$I_p = 40$
Maximum	20,218.3	20,570.4	21,939.8	24,202.7	27,358.9	31,408.6

Table 4.1: NPT kinetic energy ($\frac{kcal}{mol}$).

An obvious trend, proportional to the impulse, can be easily observed in figure 4.5. This trend has also been analysed and adjusted to an exponent

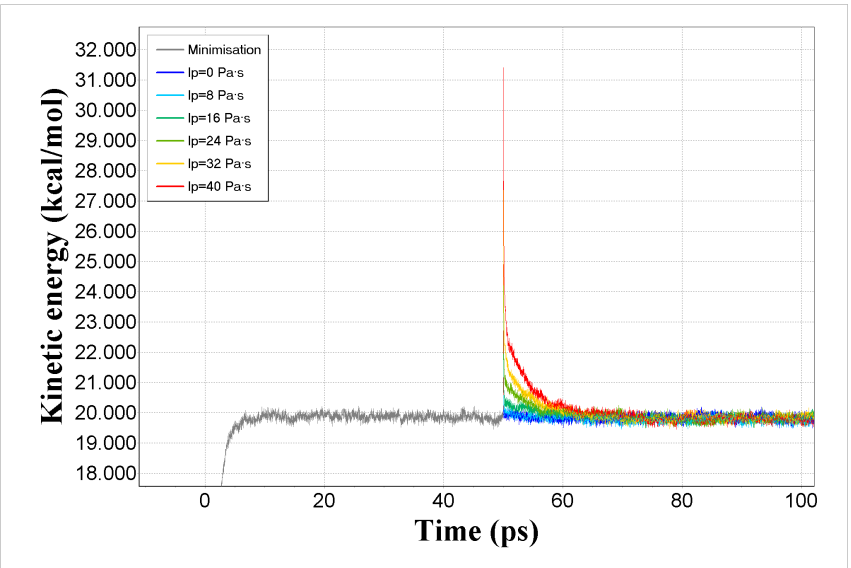

Figure 4.4: NPT kinetic energy representation.

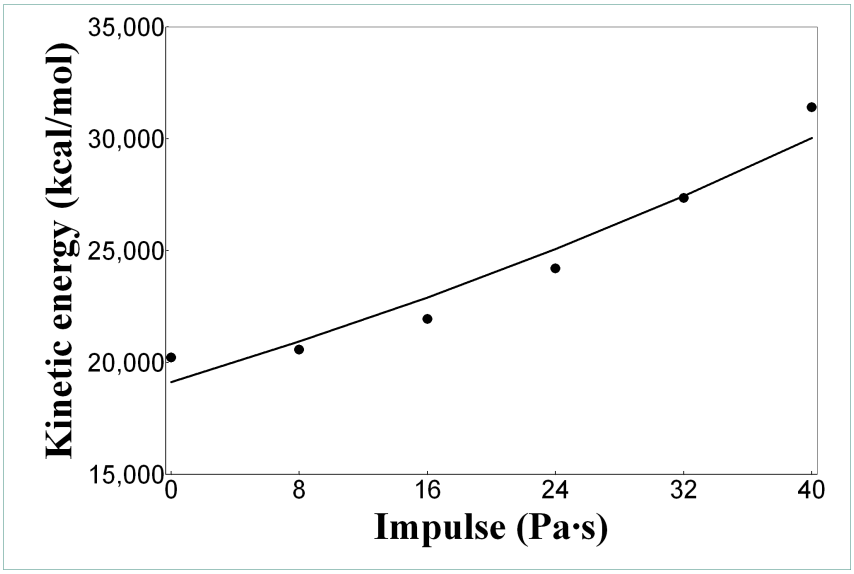

Figure 4.5: NPT kinetic energy trend.

function, which is the best fit for the obtained results.

Temperature.

As it was set out in equation 2.5, the temperature and the velocity of a *Molecular Dynamics* system are related through the Boltzman constant, so the representation of this value will have a behaviour rather similar to the case of kinetic energy.

As it was concluded from the analysis of the kinetic energy, the values come back to equilibrium after a few picoseconds and keep on fluctuating in their range until the end of the simulation in an *Molecular Dynamics* equilibrium state.

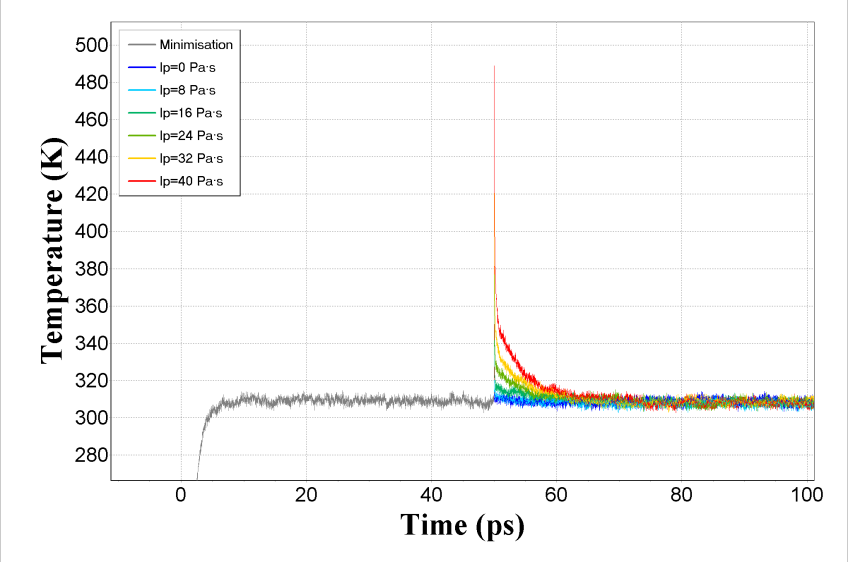

Figure 4.6: NPT temperature representation.

The representation of this variable for the time of the simulation can be seen in figure 4.6.

The trend of the maximum of the temperature is shown in figure 4.7 while the maximum values for this variable occur when the shock wave is applied and they are shown in the table below.

An obvious trend proportional to the impulse can be easily observed in figure 4.7 and it has also been calculated. The exponential function is the best fit for the obtained results.

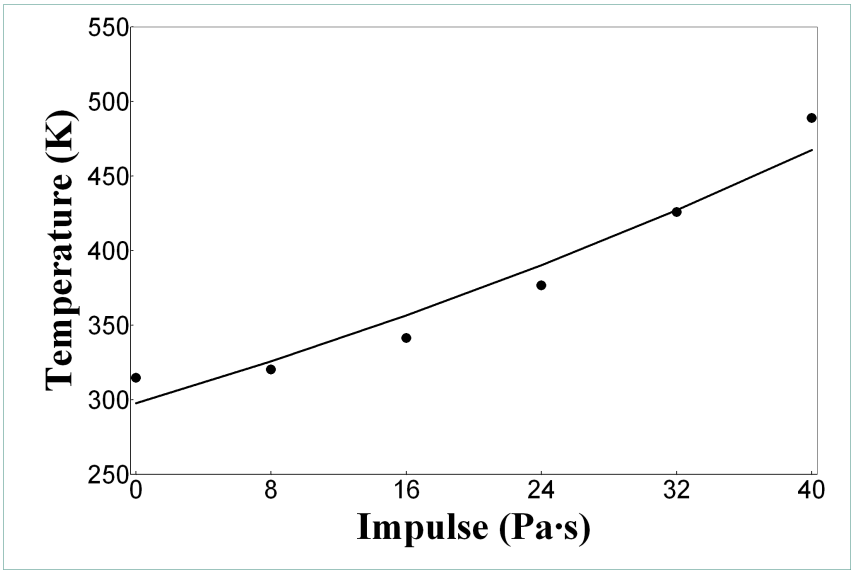

Figure 4.7: NPT temperature trend.

Impulse $(Pa \cdot s)$	$I_p = 0$	$I_p = 8$	$I_p = 16$	$I_p = 24$	$I_p = 32$	$I_p = 40$
Maximum	314.7	320.2	341.5	376.7	425.8	488.8

Table 4.2: NPT temperature (K).

Thickness of the membrane and area per lipid.

The thickness of the membrane is changing all along the simulation as the particles are in continuous movement and the dimensions of the model vary. It can be measured by calculating the difference between the maximum and the minimum positions of the lipid phosphorous atoms for each time step.

The obtained values, shown in table 4.3, do not point to any significant repercussion derived from the shock wave as they keep on fluctuating in their range around 38 Å.

Even though, we can not conclude the increase of the impulse generates a decrease in the value of the thickness as the mean values slightly fluctuate fairly unordered, the range, defined as the difference between the maximum and the minimum value, seems to experiment an increase proportional to the impulse as shown in table 4.3. An explanation for this behaviour can be in the excitement the shock wave produces into the particles as it elevates their

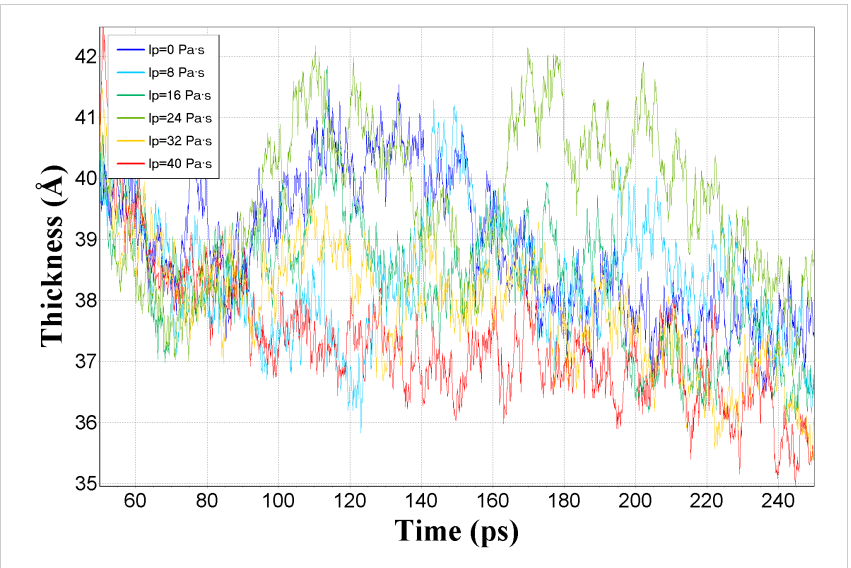

Figure 4.8: NPT thickness trend representation.

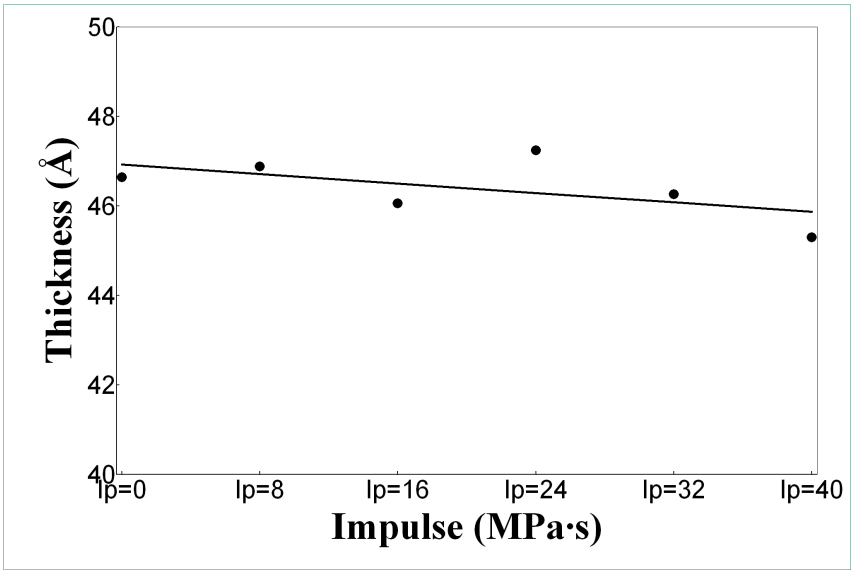

Figure 4.9: NPT thickness trend.

velocity.

The area per lipid is calculated as the area of the lipids in the plane of the bilayer divided by the total number of lipids.

Impulse $(Pa \cdot s)$	$I_p = 0$	$I_p = 8$	$I_p = 16$	$I_p = 24$	$I_p = 32$	$I_p = 40$
Maximum	41.54	41.35	41.84	42.18	41.47	42.48
Minimum	36.51	35.83	36.00	36.75	35.30	34.95
Mean value	38.87	38.42	38.29	39.62	37.90	37.30
Range	5.02	5.52	5.84	5.43	6.18	7.53

Table 4.3: NPT thickness (Å).

Even though the value of the area per lipid fluctuates all along the simulation because of the lipid movement and lateral diffusion (which will be discussed later), its mean value is not considerably affected by any of the shock waves calculated and an almost horizontal trend is obtained.

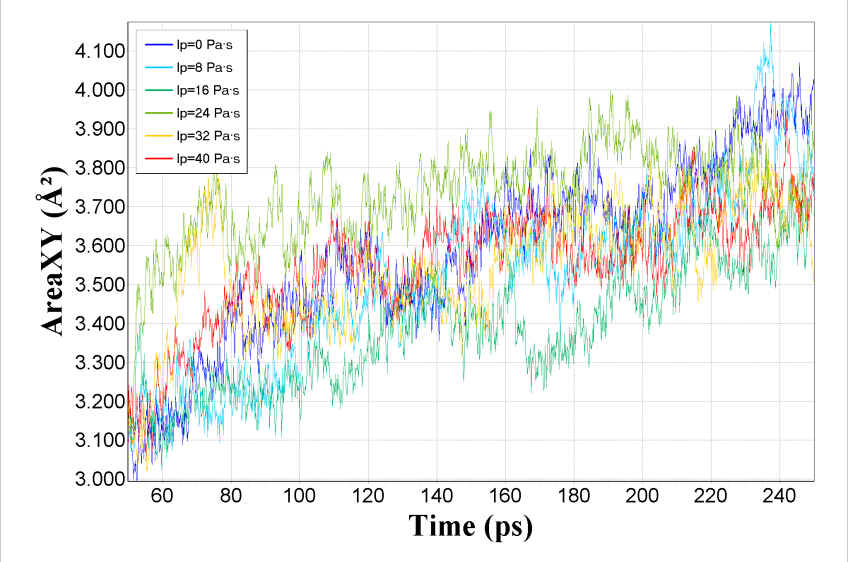

Figure 4.10: NPT area in the plane of the bilayer representation.

Impulse $(Pa \cdot s)$	$I_p = 0$	$I_p = 8$	$I_p = 16$	$I_p = 24$	$I_p = 32$	$I_p = 40$
Maximum	62	63	57	61	59	60
Minimum	45	46	46	47	46	46
Mean value	54	53	51	57	54	54

Table 4.4: NPT area per lipid (Å^2).

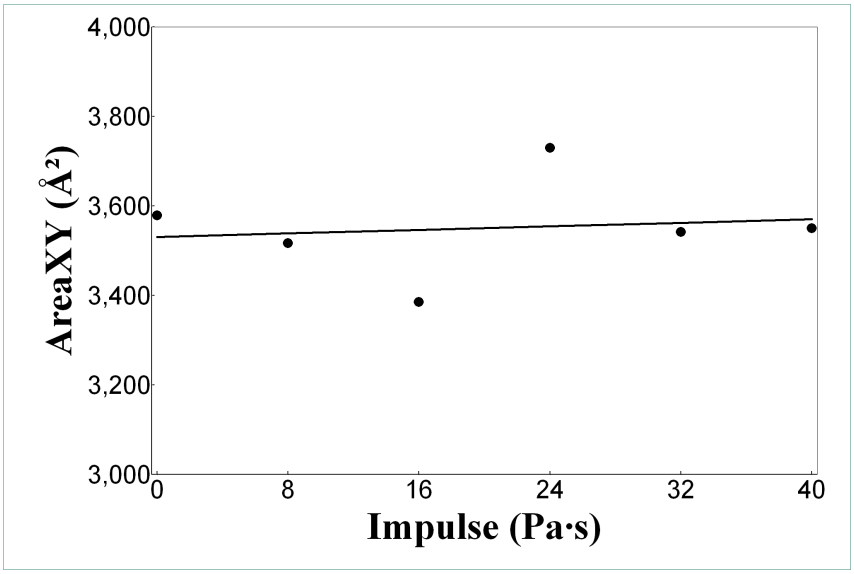

Figure 4.11: NPT area in the plane of the bilayer trend.

Volume of model.

As the velocity of the particles is affected by the shock wave, the volume of the model changes just after the shock experiencing an increase proportional to the shock wave.

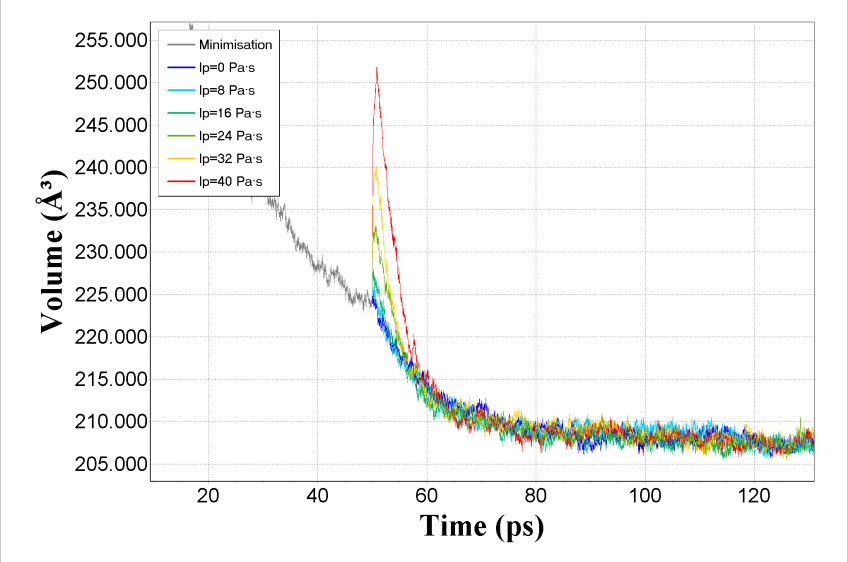

Figure 4.12: NPT volume of the model representation.

This behaviour, represented in figure 4.12, is derived from the NPT ensemble used for this simulation, since, as explained in the methodology chapter, this *Molecular Dynamics* scheme makes it possible to control both values, i.e. the temperature and the pressure, as the boundary dimensions of the system are allowed to change and the pressure is related to the volume through equation 2.6.

Impulse $(Pa \cdot s)$	$I_p = 0$	$I_p = 8$	$I_p = 16$	$I_p = 24$	$I_p = 32$	$I_p = 40$
Maximum	225,029	225,971	227,947	233,150	240,267	251,810

Table 4.5: NPT volume of the model ($Å^3$).

By the other hand, this observed increment of the volume and recover to the equilibrium state (See figure 4.12) can be considered as the numerical representation of that transient found in experiments presented by other authors [37].

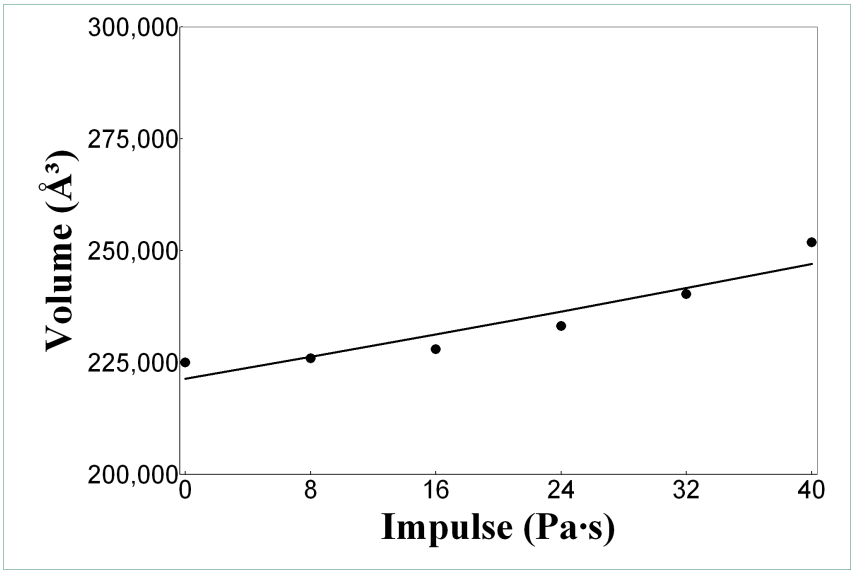

Figure 4.13: NPT volume of the model trend.

Order parameter.

The deuterium-order parameter (S_{cd}) is a measure of the average methylene group orientation with respect to the bilayer normal [91]. This quantity characterises the order of the lipid bilayers.

In the case of *Molecular Dynamics* simulations, it can be calculated using equation 4.4. The obtained values are shown in table 4.6.

$$S_c d = \frac{1}{2} \cdot (3 \cdot \cos(\beta - 1)) \tag{4.4}$$

β is the angle between a vector normal to the bilayer and the plane formed by carbon and deuterium atoms (C-H bonds).

Following equation 4.4, S_{cd} have been calculated for all the lipids and time steps along the simulation from the average orientation of the C-H bonds.

Even though this value fluctuates all along the simulation because of the lipid tails fluctuation, its mean value is not affected by any of the shock waves calculated and an almost horizontal trend around 0.2 is obtained, which is the usual value in this kind of simulation.

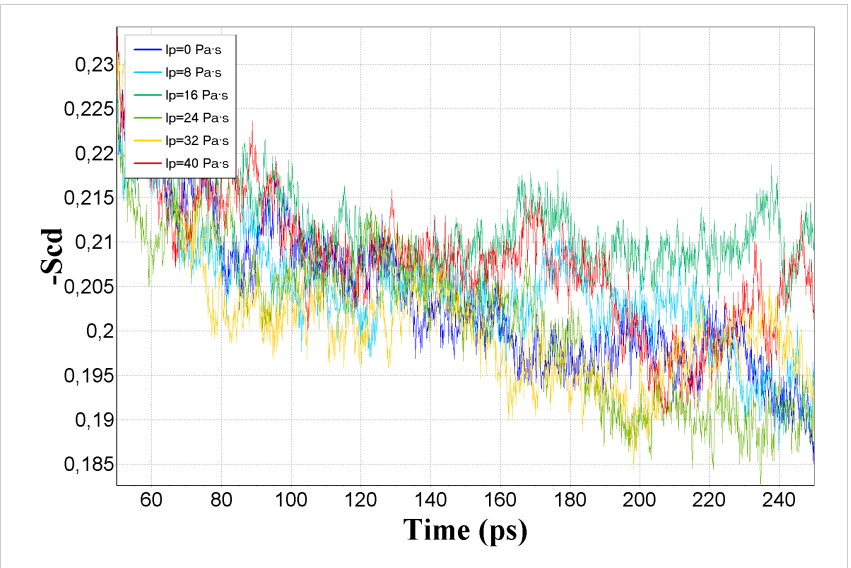

Figure 4.14: NPT order parameter representation.

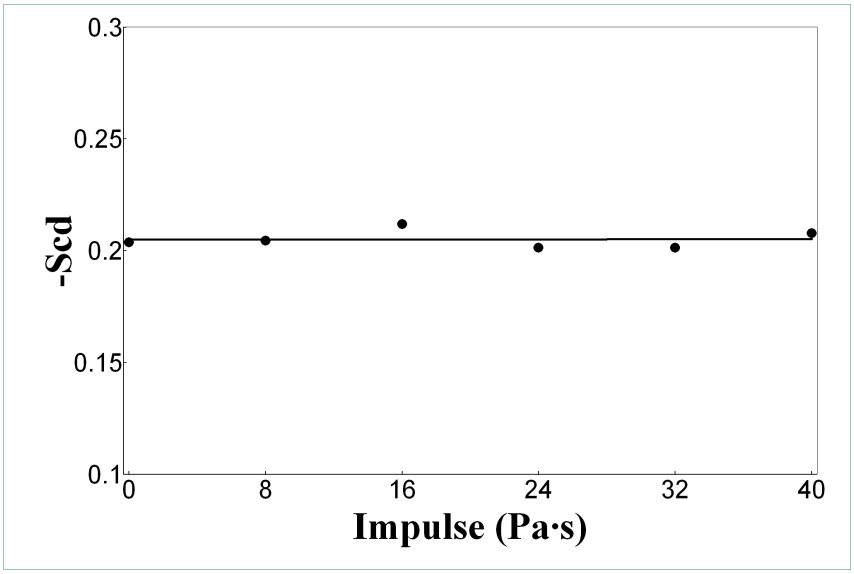

Figure 4.15: NPT order parameter trend.

Impulse ($Pa \cdot s$)	$I_p = 0$	$I_p = 8$	$I_p = 16$	$I_p = 24$	$I_p = 32$	$I_p = 40$
Maximum	0.23	0.23	0.23	0.23	0.23	0.23
Minimum	0.19	0.19	0.20	0.18	0.18	0.19
Mean value	0.20	0.20	0.21	0.20	0.20	0.21

Table 4.6: NPT order parameter.

Lateral diffusion.

As the biological cell membrane is a complex system composed of several molecules and the basic composition of which is a fluid lipid bilayer, those lipids have the ability to move laterally through the membrane surface. This process is called lateral diffusion.

Experimentally, there is a clear discrepancy between lipid lateral diffusion measured on short length scales and values obtained on longer scales using other techniques. The long range diffusion can be an order of magnitude smaller [92] and its mathematical expression can be written as:

$$D = \lim_{t\to\infty} \frac{1}{2 \cdot d_f} \cdot \frac{d}{dt}[r_i(t) - r_i(0)]^2 \tag{4.5}$$

, where index "i" refers to each lipid in the model. The coefficient is calculated as the average of the diffusion of the center of mass of each lipid.

This behaviour of the lipids implies a lateral motion can be quantified through the long time mean square displacement coefficient or MSD yielding a simulated diffusion coefficient (D) defined in equation 4.5.

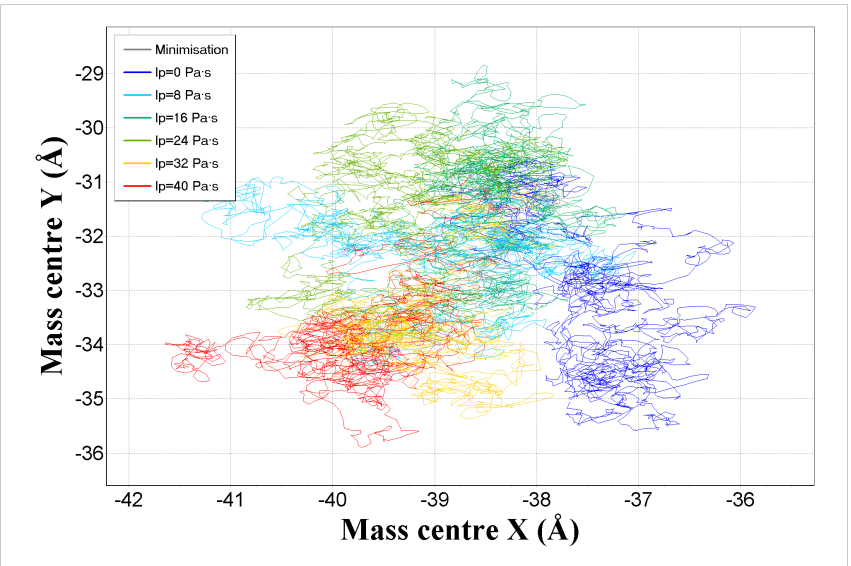

Figure 4.16: NPT mass centre of the lipids trajectory.

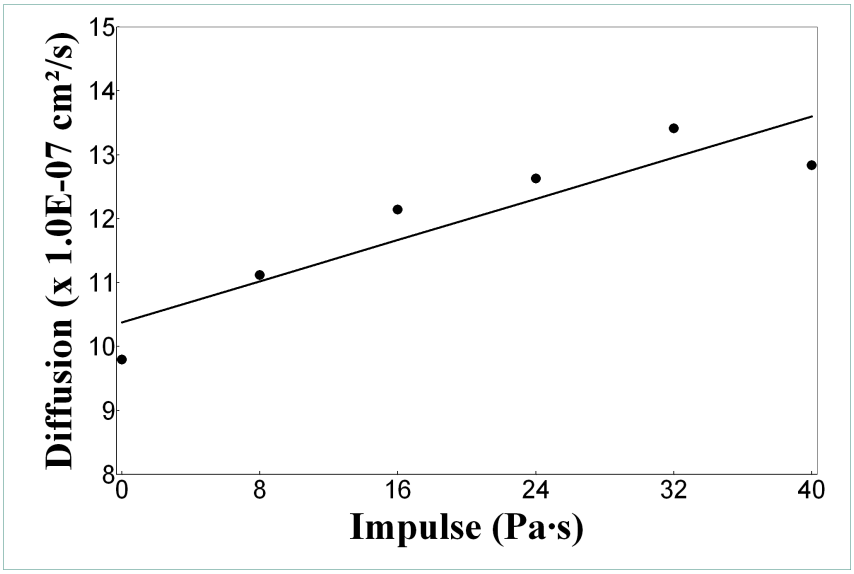

Figure 4.17: NPT lateral diffusion trend.

This diffusion process makes possible a motion of the entire lipid bilayer with respect to the centre of mass of the system (including the water molecules) and even motion of the monolayers with respect to each other [93] during the simulation. The trajectory of the centres of mass of the lipids has been tracked in order to calculate the MSD for the different impulses.

From other experimental results, it is known that, in the case of self-diffusion coefficients for water across pure ordered-phase phosphatidylcholine membranes, the values are in the order of $10^{-7}\frac{cm^2}{s}$ corresponding to a fluid bilayer. However, that value can be increased at the phase transition by two orders of magnitude [94]. This is different from air-water interfaces where a singularly high permeability to water occurs at the phase transition only [30].

In general, the translational diffusion coefficients have been found experimentally in the range from $10^{-7}\frac{cm^2}{s}$ to $10^{-12}\frac{cm^2}{s}$, bearing in mind this last one is effectively immobile for these experiments.

Impulse $(Pa \cdot s)$	$I_p = 0$	$I_p = 8$	$I_p = 16$	$I_p = 24$	$I_p = 32$	$I_p = 40$
Lateral diffusion	9.80	11.12	12.14	12.63	13.41	12.84

Table 4.7: NPT lateral diffusion $(10^{-7} \cdot \frac{cm^2}{s})$.

As explained, even though the mechanism by which lipids diffuse is cur-

rently not well characterised or understood [91], a translational lateral diffusion coefficient can be calculated from the slope of the linear regression of the MSD. Once the MSD is calculated, the diffusion coefficient can be obtained using equation 4.5 as shown in table 4.7.

On the other hand, these values point out a proportional relation between the impulse of the shock wave and lateral diffusion of the lipids.

4.1.5 Validation.

In order to validate the *Molecular Dynamics* results, a comparison will made with values obtained by other authors, which, experimental or not, will give an idea of the reliability of the calculations in this study.

The mean values of the thickness are between 37 and 40 Å (38.87 $\mathring{A}$ without shock wave) as shown in table 4.3.

A perfect agreement is obtained with other experimental [95] (35 - 41 $\mathring{A}$) and computational [95] (38.0±1.0 $\mathring{A}$) results for POPC lipid bilayers, all of them in the same range.

Thickness	Experimental	Computations	Obtained result
$\mathring{A}$	35 - 41	38.0±1.0	38.87

Table 4.8: Thickness.

The area per lipid in the plane of the bilayer has an increasing trend along the simulation, with very low values at the beginning, which, by the other hand, are affected by the shock wave. Therefore, in order to compare these with results provided by other authors, the last part of the computation must be considered where the maximum values are obtained and the lipids reached final and more stable positions.

The presented values in table 4.4 are between 59 - 63 $\mathring{A}^2$ (62 $\mathring{A}^2$ in the case of no shock wave). These results are in accord with those presented by other authors, either experimentally [95] (63 - 66 $\mathring{A}^2$) or computationally [96] (63.5±0.3 $\mathring{A}^2$), [95] (64.5±1.0 $\mathring{A}^2$), [97] (66.4±1.0 $\mathring{A}^2$) obtained.

It is considered that a value of 0.2 is the normal order of magnitude for the deuterium order parameter in the case of lipid bilayers with plenty of examples

Area per lipid	Experimental	Computations	Obtained result
$\mathring{A}^2$	63 - 66	63.5±0.3	62

Table 4.9: Area per lipid.

given in the literature. The presented numbers, in table 4.6, also agree with other simulations for POPC bilayers [96].

As was explained in subsection 4.1.4, the value of the lateral diffusion in the case of lipid bilayers can be quite flexible depending on the time scale (long term and short term measurements) and the phase of the lipids.

In any case, this study's values, in the order of $10^{-7} \cdot \frac{cm^2}{s}$ (9.8 for the case of no shock wave) are fairly matching the results presented by other authors either in the experimental [94] (1.0 - 100.0 $\cdot 10^{-7} \cdot \frac{cm^2}{s}$), [98] (6.34 - 9.00 $\cdot 10^{-7} \cdot \frac{cm^2}{s}$), [99] (1.0 - 40.0 $\cdot 10^{-7} \cdot \frac{cm^2}{s}$) or computational [100] (4.0 - 4.5 $\cdot 10^{-7} \cdot \frac{cm^2}{s}$) fields.

Lateral diffusion	Experimental	Computations	Obtained result
$\cdot 10^{-7} \cdot \frac{cm^2}{s}$	6.34 - 9.0	4.0 - 4.5	9.80

Table 4.10: Lateral diffusion.

As the reader can imagine at this point, the values of the lateral diffusion of the lipids are quite difficult to precise as they occurs at a rather small time scale, so getting values into the order of magnitude of other experiments or computations is considered a fair agreement.

4.2 The NVE ensemble

Using the Cranfield University HPC facilities another *Molecular Dynamics* study over the POPC lipid membrane was launched and successfully computed. On this occasion, the more powerful resources made possible to undertake a more ambitious computation.

The front-end machines consist of 8 X Sun UltraSPARC IIIcu processors running at 900MHz each with 16GB of shared memory, while the main machine was a Sun Fire 15000 Enterprise server with72 UltraSPARC IIIcu processors running at 1.2GHz each with 288GB shared memory available.

This time it was decided to run an NPT minimisation followed by an NVE ensemble for the simulation stage to achieve a better understanding of the physical phenomenon in a constant volume and energy computation.

4.2.1 Minimisation.

As explained in subsection 4.1.1, a local minimum in the neighbourhood of the initial position for the atoms can be easily examined in order to relieve strain in experimentally obtained conformations [87].

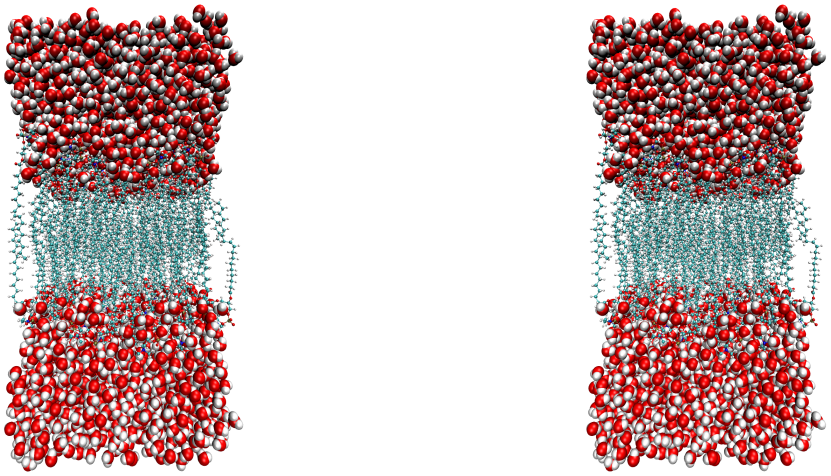

(a) Initial condition.

(b) End of minimisation, after 200 ps.

Figure 4.18: NVE minimisation.

In this case, it was possible to undertake a longer minimisation which lasted for 200 ps and was divided into three stages:

1. Minimisation for 1000 femptoseconds (fs).
2. Temperature increasing for 1000 fs.
3. Pressure increasing for 3000 fs.
4. Volume equilibration for 195000 fs.

A rather long volume equilibration was chosen for this ensemble in the NPT minimisation stage as the volume would be kept constant all along the simulation.

4.2.2 Shock wave implementation.

As explained for the NPT ensemble in subsection 4.1.2, a single shock wave characterised by an impulse which was implemented as a change in the momentum of the upper water layer.

Using equation 4.2 to calculate the velocities of the particles after the shock wave was applied, several simulations had been performed with impulses in the range of 0.0 to 40.0 $Pa \cdot s$.

4.2.3 Simulation.

Once the model is minimised and the shock wave applied, the simulation starts by using the latest coordinates and velocities of the atoms as initial conditions for the simulation (See subsection 4.1.3).

The microcanonical or NVE ensemble, i.e. the one decided upon for this experiment, is treated with more detail in section 2.3. There is no pressure or temperature control in this case, and the equations are applied as described in section 2.2.

The number of particles, the volume and the energy are kept constant all along the simulation, which means that it will not be possible to simulate the transient effects, but a rather stable simulation could be expected after the state reached in the minimisation process, which was much longer than in the case of the NPT ensemble. The simulations were run for 300 ps.

The membrane remains stable for all the intensities of the shock wave from Ip = 8 to 40 $Pa \cdot s$. The representation of the *Molecular Dynamics* calculation can be seen in figures 4.19 and 4.20 without any lost of structure in the lipid membrane.

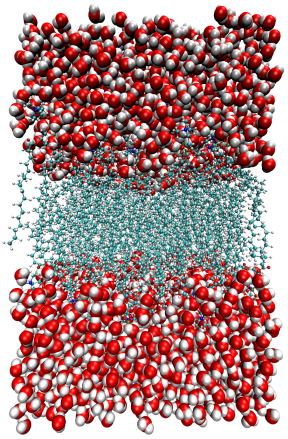

(a) t=0.1 ps.

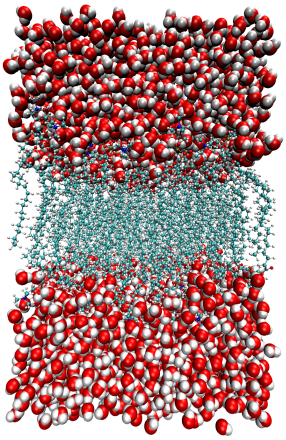

(b) t=25 ps.

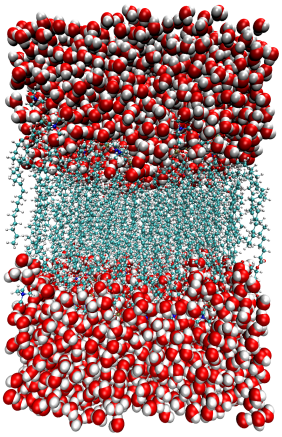

(c) t=50 ps.

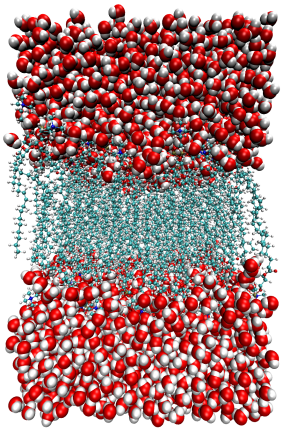

(d) t=75 ps.

Figure 4.19: NVE simulation without shock-wave.

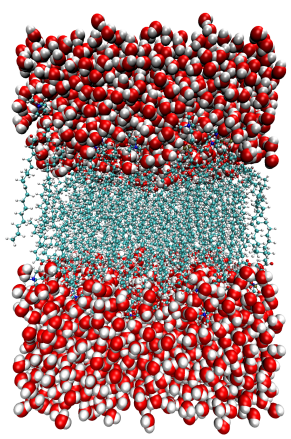

(a) t=0.1 ps.

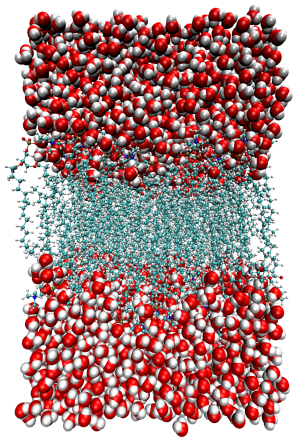

(b) t=25 ps.

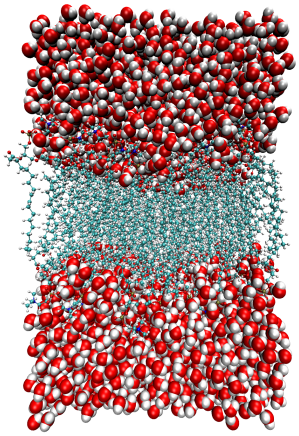

(c) t=50 ps.

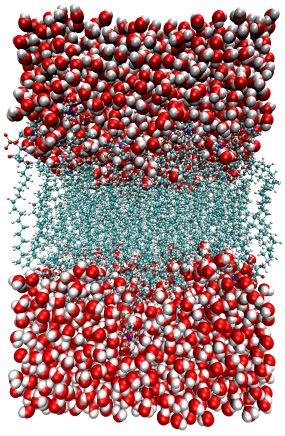

(d) t=75 ps.

Figure 4.20: NVE simulation with a shock-wave of Ip = 40 $Pa \cdot s$.

4.2.4 Analysis.

After the simulations are computed, the results can be processed and analysed in the same way as for previous calculations, as can be seen in subsection 4.1.4.

As could already be assumed, the obtained volume curve will not be analysed as it has no bearing at all in the case of an NVE ensemble.

Kinetic energy.

The shock wave generates a sudden increment in the kinetic energy (E_k), which can be calculated using equation 4.3.

The produced imbalance is kept all along the simulation, therefore the transient effect, one of the most important characteristics of this process, is missing in this ensemble.

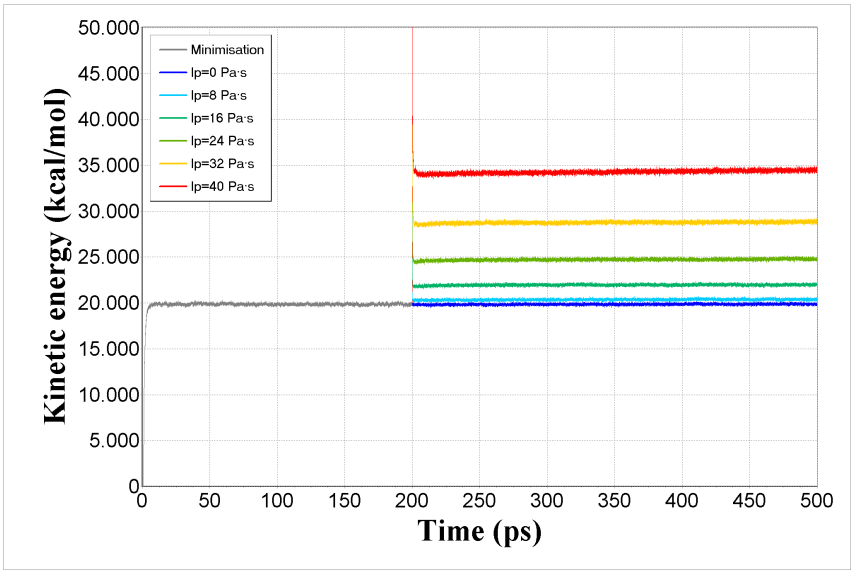

Figure 4.21: NVE kinetic energy representation.

The values obtained for the kinetic energy are shown in table 4.11. In this case, the NVE ensemble keeps the energy of the system fluctuating into its range at some point between the minimisation state and the artificial state generated by the change of the momentum provoked by the single shock wave application.

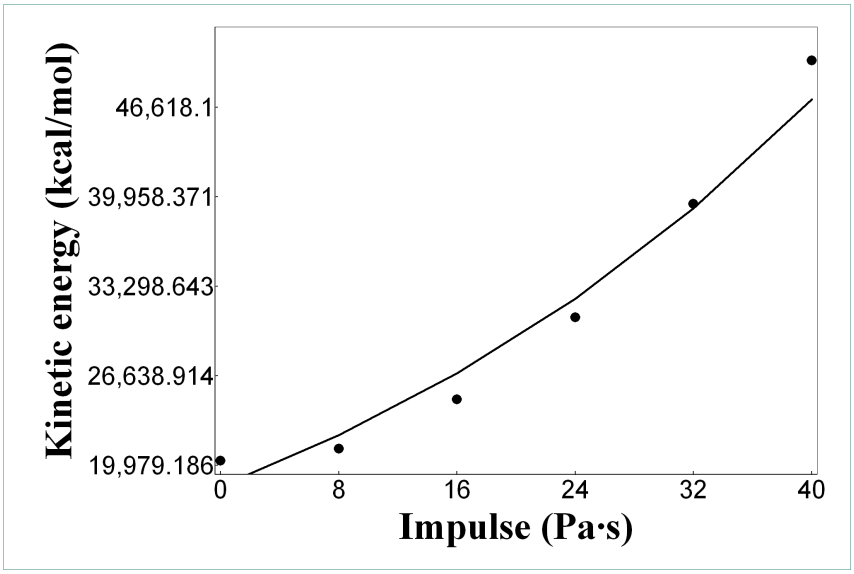

Figure 4.22: NVE kinetic energy trend.

Impulse (Pas)	Ip=0	Ip=8	Ip=16	Ip=24	Ip=32	Ip=40
Maximum	3546.7	3506.3	3705.3	3775.9	3896.4	4284.2

Table 4.11: NVE kinetic energy ($\frac{kcal}{mol}$).

Temperature.

As set out in equation 2.5, the temperature and the velocity of a *Molecular Dynamics* system are related through the Boltzman constant, so the representation of this value will have a behaviour rather similar to the case of kinetic energy.

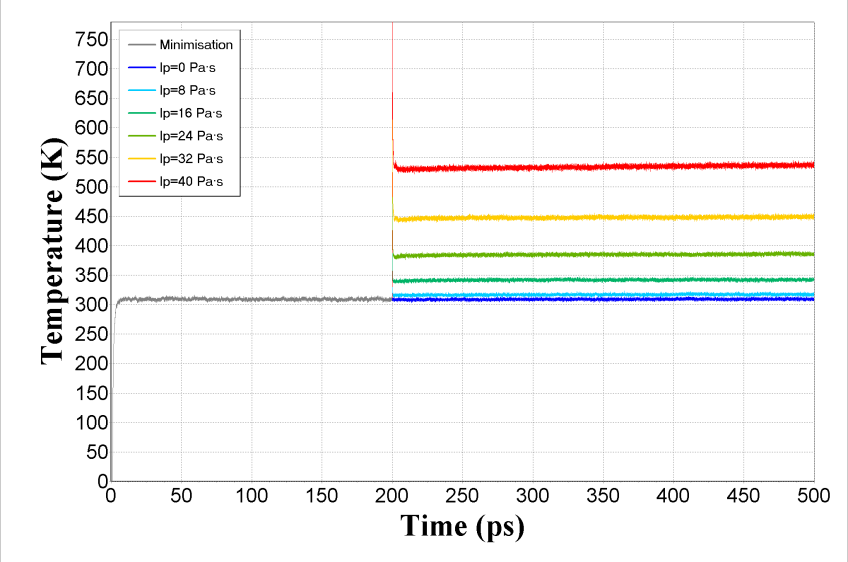

Figure 4.23: NVE temperature representation.

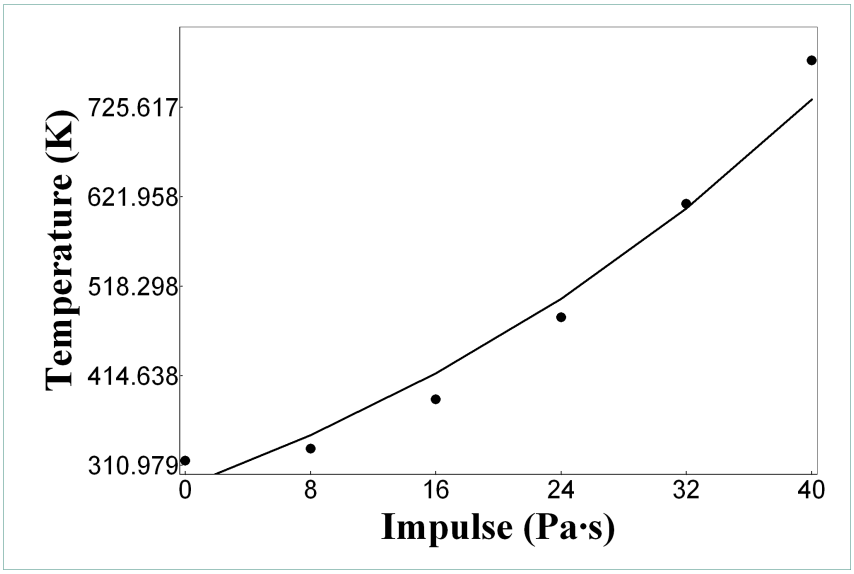

Figure 4.24: NVE temperature trend.

From figure 4.23 it can be seen how the NVE ensemble keeps the temperature fluctuating at some point between the minimisation state and the artificial state generated by the shock wave application.

Impulse (Pas)	Ip=0	Ip=8	Ip=16	Ip=24	Ip=32	Ip=40
Maximum	316.0	329.8	387.1	482.1	613.4	779.6
Mean value	302.6	307.2	322.0	347.3	384.4	435.0

Table 4.12: NVE temperature (K).

The obtained results are shown in table 4.12. These values do not make any sense for the case of a biological system because the temperature stabilises at values much higher than those accepted by any living organism and the NVE ensemble does not permit any control over it.

Thickness of the membrane and area per lipid.

As explained in subsection 4.1.4, the thickness of the membrane can be calculated in the *Molecular Dynamics* simulations for each time step. Their representation is shown in figure 4.25.

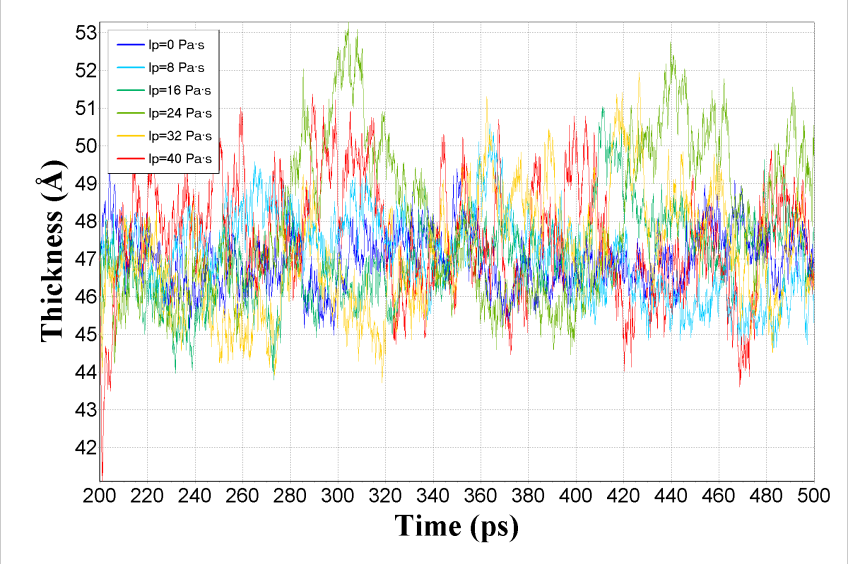

Figure 4.25: NVE thickness representation.

The obtained values are shown in table 4.13

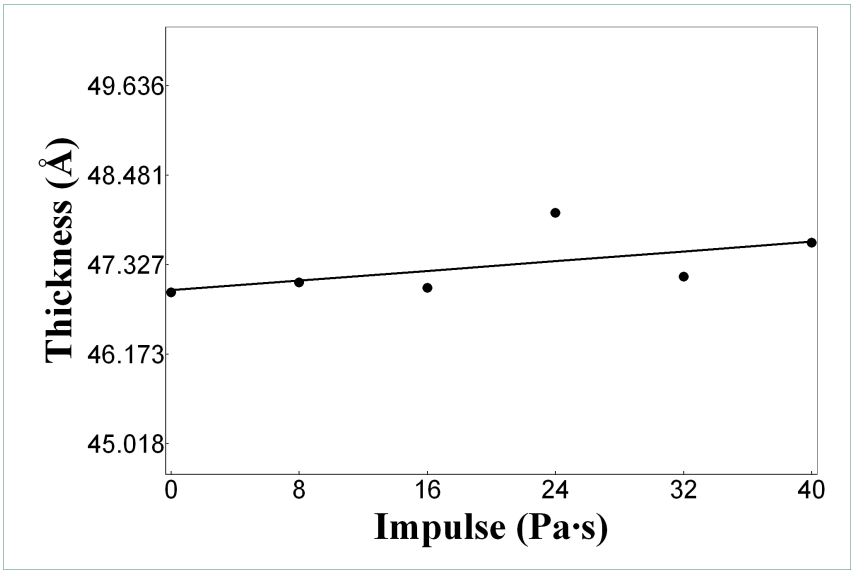

Figure 4.26: NVE thickness trend.

Impulse (Pas)	Ip=0	Ip=8	Ip=16	Ip=24	Ip=32	Ip=40
Maximum	49.45	50.59	51.05	53.29	51.95	51.38
Minimum	44.98	44.64	43.79	44.24	43.72	41.10
Mean value	46.97	47.10	47.03	48.00	47.17	47.61
Range	4.47	5.95	7.25	9.05	8.23	10.27

Table 4.13: NVE thickness (Å).

The representation of the area in the plane of the bilayer is shown in figure 4.27.

In this case, it has been found that a positive trend for this area in the plane of the bilayer and, following the obtained the results, it would be considerately affected by the application of a shock wave. This is because the NVE ensemble let the temperature stabilyse at higher values with no transient effect, so temperature related values, like this area, are numerically affected.

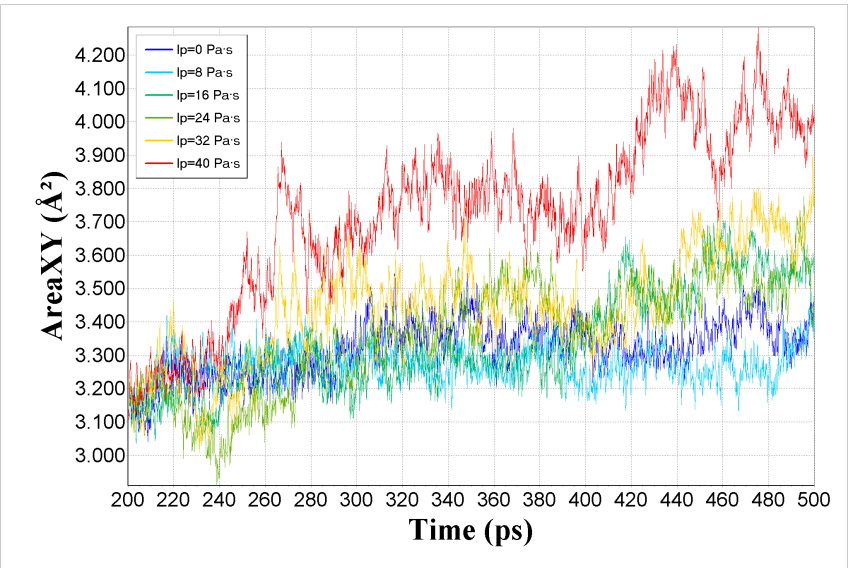

Figure 4.27: NVE area in the plane of the bilayer representation.

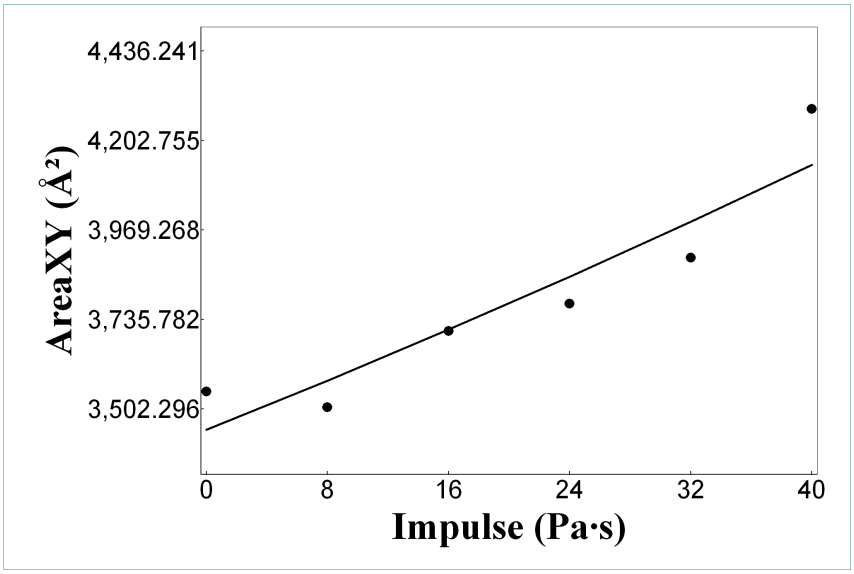

Figure 4.28: NVE area in the plane of the bilayer trend.

Impulse (Pas)	Ip=0	Ip=8	Ip=16	Ip=24	Ip=32	Ip=40
Maximum	53.74	53.13	56.14	57.21	59.04	64.91
Minimum	46.07	46.00	46.12	44.08	45.59	47.07
Mean value	50.28	49.56	50.57	50.9	52.2	56.44

Table 4.14: NVE area per lipid ($Å^2$).

Order parameter.

The deuterium-order parameter (S_{cd}) characterises the order of the lipid bilayers as described in subsection 4.1.4.

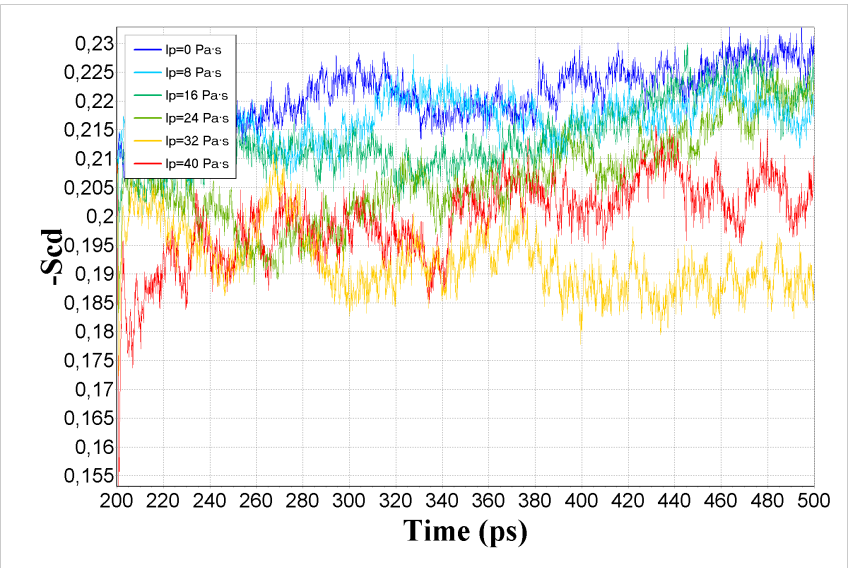

Figure 4.29: NVE order parameter representation.

Their representation in figure 4.29 shows a normal *Molecular Dynamics* simulation fluctuation and a logical descending trend. The obtained values are shown in table 4.15.

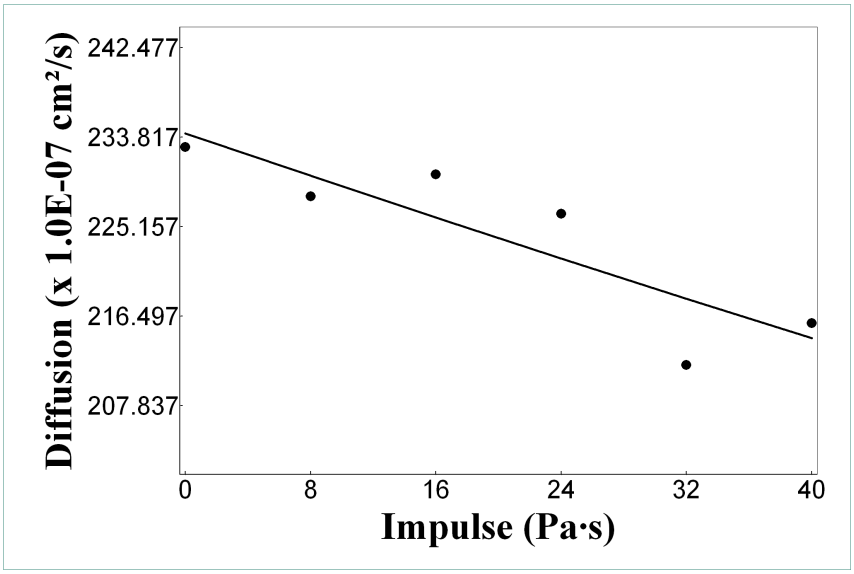

Figure 4.30: NVE order parameter trend.

Impulse (Pas)	Ip=0	Ip=8	Ip=16	Ip=24	Ip=32	Ip=40
Maximum	0.23	0.23	0.23	0.23	0.21	0.22
Minimum	0.21	0.20	0.20	0.18	0.17	0.15
Mean value	0.22	0.22	0.21	0.21	0.19	0.20

Table 4.15: NVE order parameter.

Lateral diffusion.

This behaviour of the lipids, explained in subsection 4.1.4, is represented in figure 4.31.

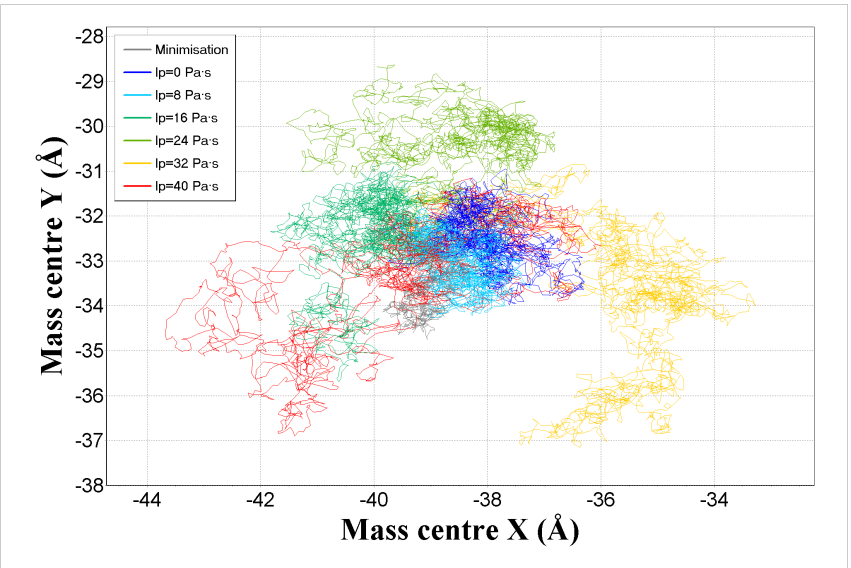

Figure 4.31: NVE mass centre of the lipids trajectory.

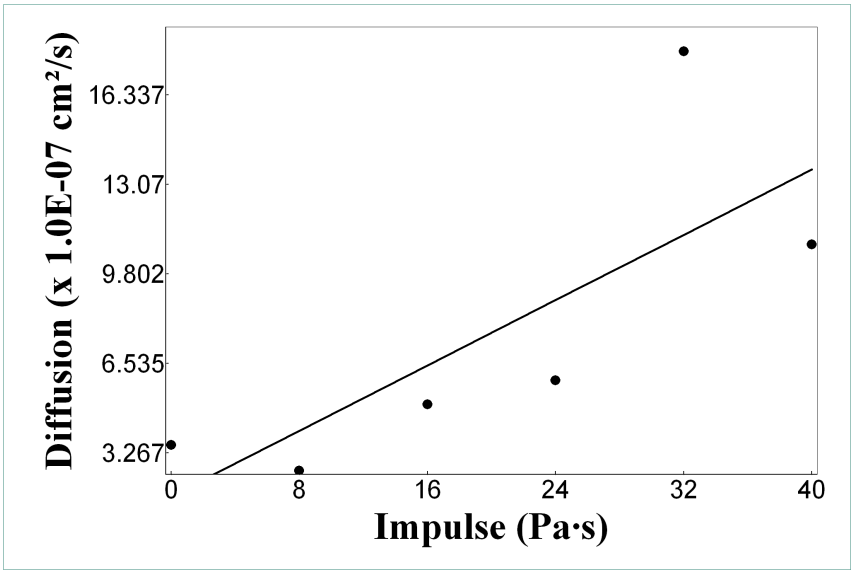

Figure 4.32: NVE lateral diffusion trend.

Even though the values are in the order of magnitude of other published results, it was not possible to find a sensible trend for the lateral diffusion in the case of the launched NVE ensemble.

Impulse $(Pa \cdot s)$	$I_p = 0$	$I_p = 8$	$I_p = 16$	$I_p = 24$	$I_p = 32$	$I_p = 40$
Lateral diffusion	3.56	2.62	5.04	5.92	17.93	10.89

Table 4.16: NVE lateral diffusion $(10^{-7} \cdot \frac{cm^2}{s})$.

4.2.5 Validation.

As shown in the first study, presented in chapter 4.1, these *Molecular Dynamics* results can be validated by comparison with values obtained by other authors.

The thickness mean values are between 47 and 48 Å (46.97 $\mathring{A}$ without shock wave) as shown in table 4.13.

Other experimental [95] (35 - 41 $\mathring{A}$) and computational [95] (38.0±1.0 $\mathring{A}$) results for POPC lipid bilayers have slightly lower values, therefore thicker values are being obtained and they cannot be adjusted as the NVE ensemble does not allow that over the volume of the control cell.

Thickness	Experimental	Computations	Obtained result
$\mathring{A}$	35 - 41	38.0±1.0	47

Table 4.17: Thickness.

The obtained values for the area in the plane of the bilayer are shown in table 4.14 are between 49 - 56 $\mathring{A}^2$ (50.28 $\mathring{A}^2$ in the case of no shock wave). These results are lower than those presented by other authors, either experimentally [95] (63 - 66 $\mathring{A}^2$) or computationally [96] (63.5±0.3 $\mathring{A}^2$), [95] (64.5±1.0 $\mathring{A}^2$), [97] (66.4±1.0 $\mathring{A}^2$) obtained.

Area per lipid	Experimental	Computations	Obtained result
$\mathring{A}^2$	63 - 66	63.5 - 64.5 ±0.3	50.28

Table 4.18: Area per lipid.

The same NVE limitations are being experienced again. As well as with the thickness value, this ensemble does not provide any adjustment for the volume of the cell.

As shown in the case of the NPT ensemble, the lipids find their place along the simulation resulting in an area increase and a thickness reduction. This process cannot occur in the case of the microcanonical ensemble as the volume remains constant.

As the reader will have already noticed, after briefly looking into section 4.2.1, a extremely long NPT minimisation process was computed to improve the volume equilibration. However, the results are not satisfactory.

It is considered that a value of 0.2 is the normal order of magnitude for the deuterium order parameter in the case of lipid bilayers with plenty of examples in the literature. The presented numbers, in table 4.15, also agree with other simulations for POPC bilayers [96].

As explained in subsection 4.1.4, the value of the lateral diffusion in the case of lipid bilayers can be quite flexible depending on the time scale (long term and short term measurements) and the phase of the lipids.

The obtained values, in the order of $10^{-7} \cdot \frac{cm^2}{s}$ are in agreement with results presented by other authors either in the experimental [94] (1.0 - 100.0 $\cdot 10^{-7} \cdot \frac{cm^2}{s}$), [98] (6.34 - 9.00 $\cdot 10^{-7} \cdot \frac{cm^2}{s}$), [99] (1.0 - 40.0 $\cdot 10^{-7} \cdot \frac{cm^2}{s}$) or computational [100] (4.0 - 4.5 $\cdot 10^{-7} \cdot \frac{cm^2}{s}$) field.

Lateral diffusion	Experimental	Computations	Obtained result
$\cdot 10^{-7} \cdot \frac{cm^2}{s}$	6.34 - 9.0	4.0 - 4.5	3.56

Table 4.19: Lateral diffusion.

It can be concluded, therefore, that the geometrical adjust limitation of the NVE ensemble does not make it possible to validate this simulation.

4.3 NPT and NVE ensembles comparison

As it has been discussed in previous sections 4.1 and 4.2, two different lots of simulations, one using a NPT ensemble and another one using a NVE ensemble, have been successfully computed for the study of the interaction of shock waves

with a biological cell membranes. This section is going to be used to compare the obtained results for both computations.

The NPT ensemble let pressure and temperature be set up to target values, while the NVE ensemble makes volume and energy constant all along the simulation. The main difference, from the biological point of view, lies on the possibility of simulating the transient occurred as the shock wave impacts the membrane [13], which is possible using the NPT ensemble as the volume adapts to pressure and temperature conditions.

4.3.1 Thickness of the membrane.

A table with the results obtained for the thickness with both ensembles is presented next:

NPT						
Impulse ($Pa \cdot s$)	$I_p = 0$	$I_p = 8$	$I_p = 16$	$I_p = 24$	$I_p = 32$	$I_p = 40$
Maximum	41.54	41.35	41.84	42.18	41.47	42.48
Minimum	36.51	35.83	36.00	36.75	35.30	34.95
Mean value	38.87	38.42	38.29	39.62	37.90	37.30
Range	5.02	5.52	5.84	5.43	6.18	7.53
NVE						
Impulse (Pas)	Ip=0	Ip=8	Ip=16	Ip=24	Ip=32	Ip=40
Maximum	49.45	50.59	51.05	53.29	51.95	51.38
Minimum	44.98	44.64	43.79	44.24	43.72	41.10
Mean value	46.97	47.10	47.03	48.00	47.17	47.61
Range	4.47	5.95	7.25	9.05	8.23	10.27

Table 4.20: NPT and NVE thickness comparison (Å).

It is observed that higher values appear for the NVE ensemble. This effect occurs because there is not volume fluctuation in that kind of computations as it remains constant. That is opposite to the NPT ensemble, where the volume fluctuation is not restricted and the molecules move in order to find their equilibrium position for the pressure and temperature conditions set at the beginning of the simulation.

That is the reason why experimental [95] (35 - 41 $\mathring{A}$) and computational

[95] (38.0±1.0 $\mathring{A}$) results for POPC lipid bilayers do not agree with this NVE simulations, which yield thicker values, while the NPT ensemble results agree with those results presented by other authors.

Even though, we can not conclude the increase of the impulse generates a decrease in the value of the thickness as the mean values just slightly fluctuate, the range, defined as the difference between the maximum and the minimum value, seems to experiment an increase proportional to the impulse as shown in table 4.3. An explanation for this behaviour can be in the excitement the shock wave produces into the particles as it elevates their velocity.

4.3.2 Area per lipid.

A table with the results obtained for the area per lipid with both ensembles can be seen next:

NPT						
Impulse ($Pa \cdot s$)	$I_p = 0$	$I_p = 8$	$I_p = 16$	$I_p = 24$	$I_p = 32$	$I_p = 40$
Maximum	62	63	57	61	59	60
Minimum	45	46	46	47	46	46
Mean value	54	53	51	57	54	54
NVE						
Impulse (Pas)	Ip=0	Ip=8	Ip=16	Ip=24	Ip=32	Ip=40
Maximum	54	53	56	57	59	65
Minimum	46	46	46	44	46	47
Mean value	50	50	51	51	52	56

Table 4.21: NPT and NVE area per lipid comparison (Å^2).

The values obtained for the NPT ensemble are higher than the ones obtained for the NVE ensemble. This difference occurs because in the case of the NPT ensemble the dimensions of the *Molecular Dynamics* simulation box can fluctuate in order to maintain pressure and temperature set to their target values and, therefore, letting the lipids move to find their location along the simulation, expanding the dimensions in the XY plane if necessary.

As in the case of the thickness, the values for the NPT ensemble, between 59 - 63 $\mathring{A}^2$ (62 $\mathring{A}^2$ in the case of no shock wave), are in accord with those presented

by other authors, either experimentally [95] (63 - 66 $\mathring{A}^2$) or computationally [96] (63.5±0.3 $\mathring{A}^2$), [95] (64.5±1.0 $\mathring{A}^2$), [97] (66.4±1.0 $\mathring{A}^2$) obtained, while the values presented for the NVE ensemble are slightly lower.

4.3.3 Order parameter.

A table with the results obtained for the order parameter with both ensembles are shown next:

NPT						
Impulse ($Pa \cdot s$)	$I_p = 0$	$I_p = 8$	$I_p = 16$	$I_p = 24$	$I_p = 32$	$I_p = 40$
Maximum	0.23	0.23	0.23	0.23	0.23	0.23
Minimum	0.19	0.19	0.20	0.18	0.18	0.19
Mean value	0.20	0.20	0.21	0.20	0.20	0.21
NVE						
Impulse (Pas)	Ip=0	Ip=8	Ip=16	Ip=24	Ip=32	Ip=40
Maximum	0.23	0.23	0.23	0.23	0.21	0.22
Minimum	0.21	0.20	0.20	0.18	0.17	0.15
Mean value	0.22	0.22	0.21	0.21	0.19	0.20

Table 4.22: NPT and NVE order parameter comparison.

In the case of the order parameter, the values are in the same order for both ensembles (around 0.2), so the lipid membrane agrees with the values presented by other authors in both cases.

4.3.4 Lateral diffusion.

A table with the results obtained for the lateral diffusion with both ensembles are presented next:

Lower values are observed for the NVE ensemble, and then again, it can be concluded that the fluctuations of the dimensions of the *Molecular Dynamics* box in the case of the NPT ensemble are the reason for this difference as the dimensions expands in order to set pressure and temperature to their target values giving the lipids more space for lateral diffusion.

NPT						
Impulse $(Pa \cdot s)$	$I_p = 0$	$I_p = 8$	$I_p = 16$	$I_p = 24$	$I_p = 32$	$I_p = 40$
Lateral diffusion	9.80	11.12	12.14	12.63	13.41	12.84
NVE						
Impulse $(Pa \cdot s)$	$I_p = 0$	$I_p = 8$	$I_p = 16$	$I_p = 24$	$I_p = 32$	$I_p = 40$
Lateral diffusion	3.56	2.62	5.04	5.92	17.93	10.89

Table 4.23: NPT and NVE lateral diffusion comparison $(10^{-7} \cdot \frac{cm^2}{s})$.

4.4 Other bilayers

Fortunately, the author has had the chance to use the Cranfield University HPC facilities for these lots of computations, which model are described in subsection 3.2.2, otherwise it would have been impossible to undertake such a task.

As presented in section 4.2, this system consisted of front-end machines of 8 X Sun UltraSPARC IIIcu processors running at 900MHz each with 16GB of shared memory, while the main machine was a Sun Fire 15000 Enterprise server with 72 UltraSPARC IIIcu processors running at 1.2GHz each with 288GB shared memory available.

After the disappointment with the NVE ensemble, it was decided to come back to the NPT ensemble for this group of studies.

4.4.1 Minimisation.

Similar processes, as explained in subsection 4.1.1, have been repeated. In this case the stages for the NPT ensemble are:

1. Minimisation for 1000 femptoseconds (fs).
2. Temperature increasing for 1000 fs.
3. Pressure increasing for 3000 fs.
4. Volume equilibration for 45000 fs.

4.4.2 Shock wave implementation.

A single shock wave characterised by an impulse in the range of 0.0 to 40.0 $Pa \cdot s$ is applied in the same way as was explained in subsection 4.1.2.

4.4.3 Simulation.

The simulations, undertaken in the same way as in subsection 4.1.3, were computed for 200 ps and they will be discussed all along the next subsections.

Representations for the DMPC bilayer.

The membrane remains well-shaped for all the intensities of the shock wave from Ip = 8 to 40 $Pa \cdot s$ as it can be seen in figure 4.34.

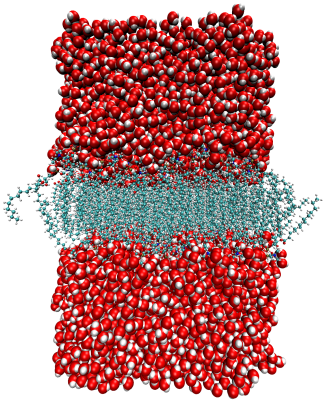

(a) t=0.1 ps.

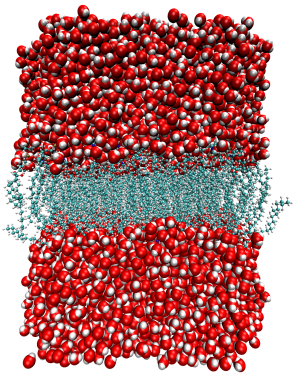

(b) t=25 ps.

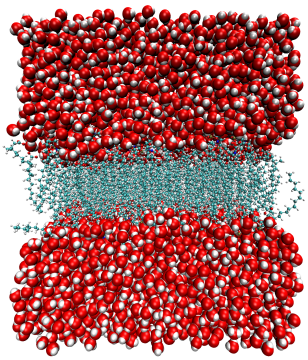

(c) t=50 ps.

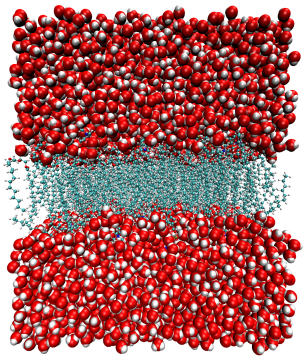

(d) t=75 ps.

Figure 4.33: DMPC simulation without shock-wave.

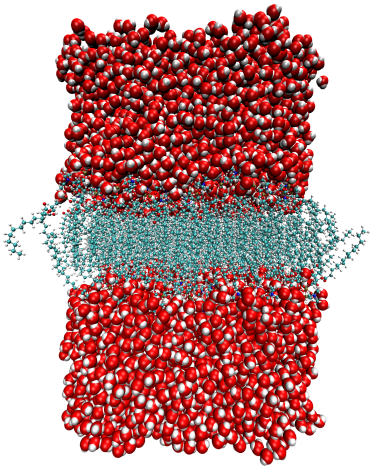

(a) t=0.1 ps.

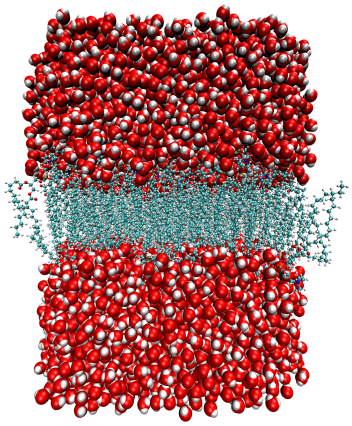

(b) t=25 ps.

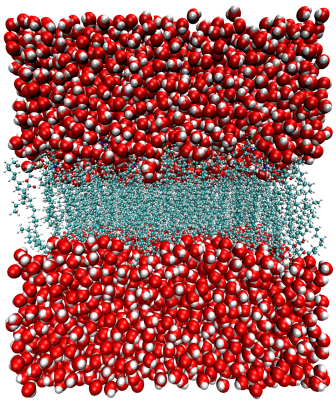

(c) t=50 ps.

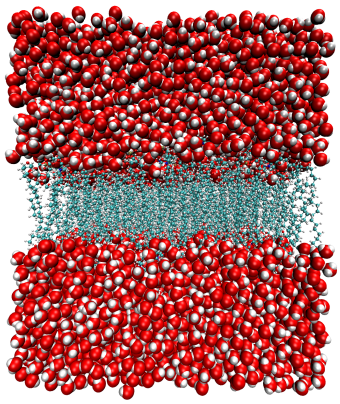

(d) t=75 ps.

Figure 4.34: DMPC simulation with a shock-wave of Ip = 40 $Pa \cdot s$.

Representations for the DPPC bilayer.

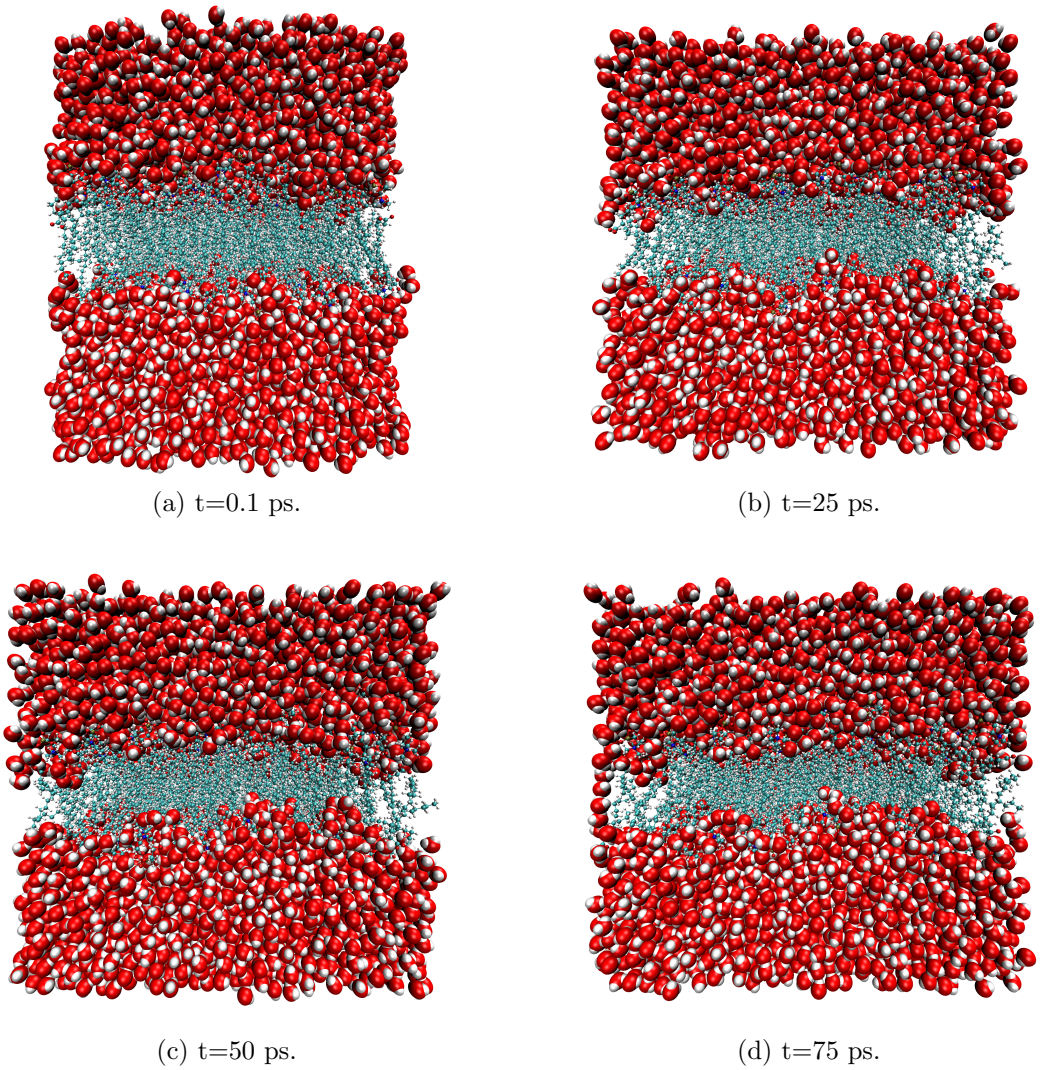

(a) t=0.1 ps.

(b) t=25 ps.

(c) t=50 ps.

(d) t=75 ps.

Figure 4.35: DPPC simulation without shock-wave.

The membrane does not remain well-shaped for this lot of simulations and the lipids rotate into a rather horizontal position, so the values of the thickness, area per lipid and order parameter, as well as, lateral diffusion will not be affected as we will see later.

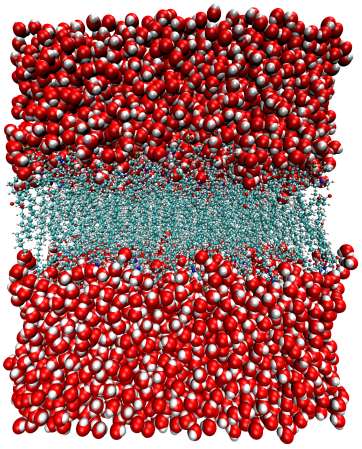

(a) t=0.1 ps.

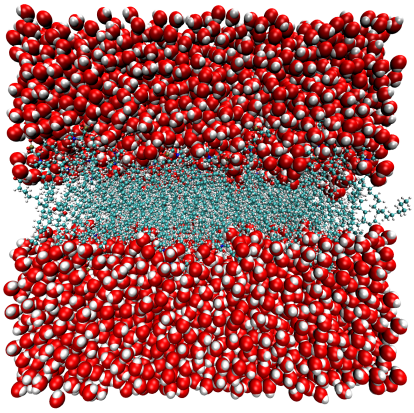

(b) t=25 ps.

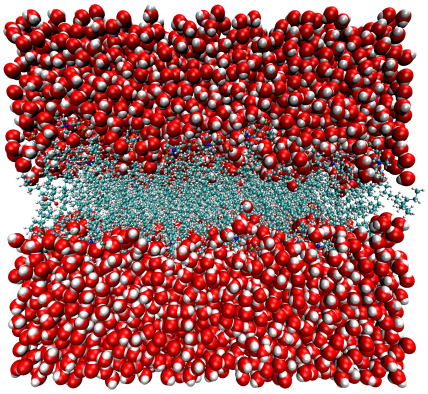

(c) t=50 ps.

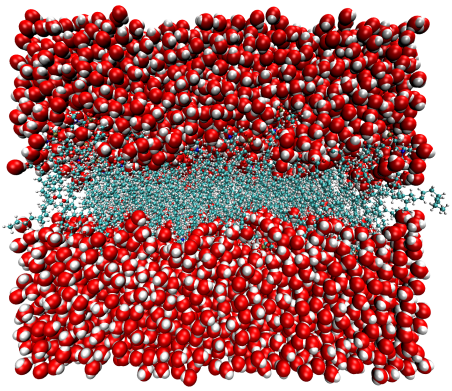

(d) t=75 ps.

Figure 4.36: DPPC simulation with a shock-wave of Ip = 40 $Pa \cdot s$.

Representations for the POPE bilayer.

The membrane remains well-shaped for all the intensities of the shock wave from Ip = 8 to 40 $Pa \cdot s$ as it can be seen in figure 4.38.

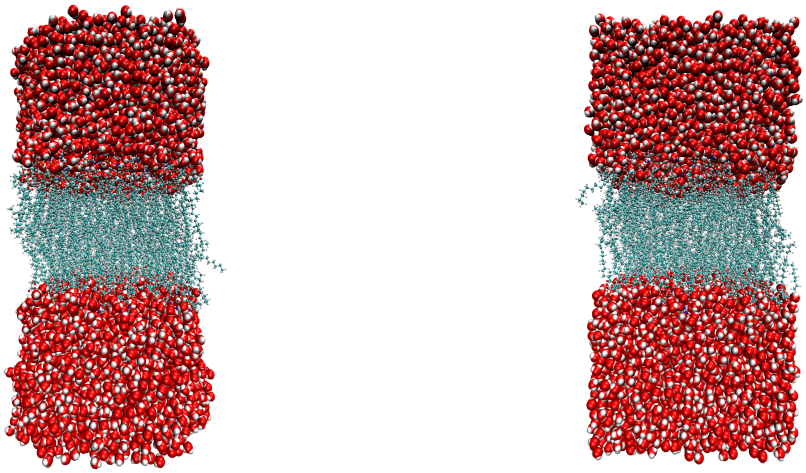

(a) t=0.1 ps.

(b) t=25 ps.

(c) t=50 ps.

(d) t=75 ps.

Figure 4.37: POPE simulation without shock-wave.

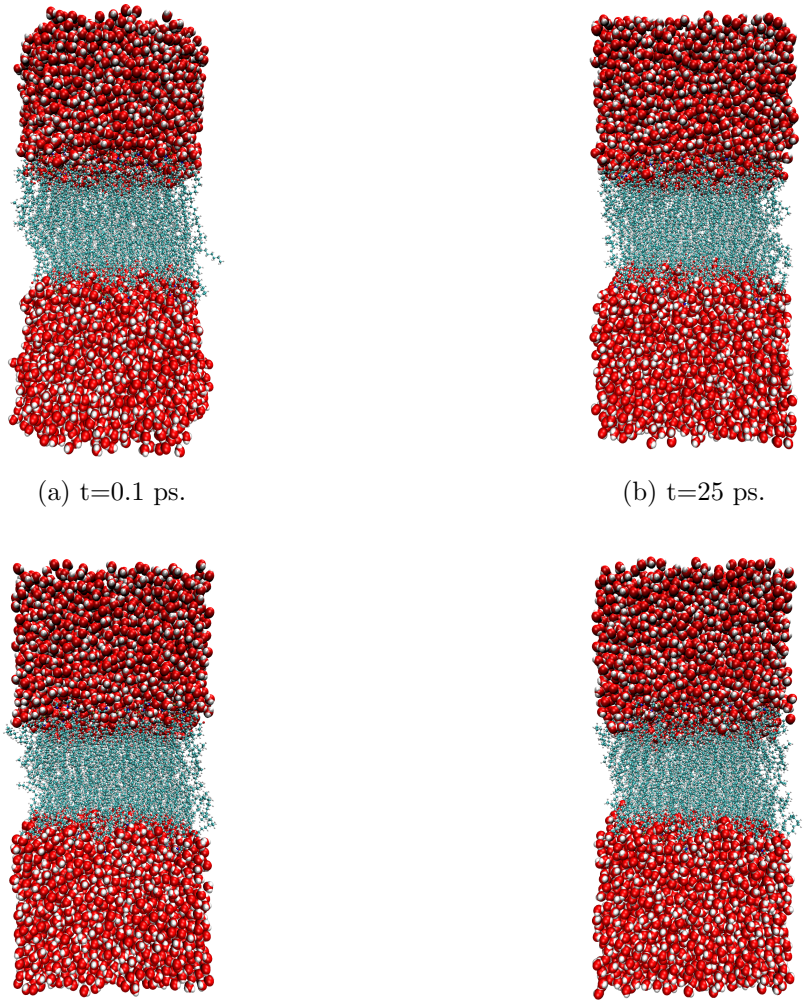

(a) t=0.1 ps.

(b) t=25 ps.

(c) t=50 ps.

(d) t=75 ps.

Figure 4.38: POPE simulation with a shock-wave of Ip = 40 $Pa \cdot s$.

4.4.4 Results.

After the computation of the simulations, the post-processing of the results were made. The representation of the obtained values are presented below.

We are not going to show all the results discussed in previous sections as they have been analyzed for the other membrane simulations and the conclusions would be similar, however, the results for the key parameters will be presented next and discussed at the end of this section.

Results for the DMPC bilayer.

Thickness of the membrane.

Impulse $(Pa \cdot s)$	$I_p = 0$	$I_p = 8$	$I_p = 16$	$I_p = 24$	$I_p = 32$	$I_p = 40$
Maximum	45.06	45.30	45.05	46.76	45.61	43.45
Minimum	37.64	37.67	37.48	37.41	38.12	37.29
Mean value	41.95	42.21	42.08	42.76	42.05	40.66

Table 4.24: DMPC bilayer thickness (Å).

Area per lipid.

Impulse $(Pa \cdot s)$	$I_p = 0$	$I_p = 8$	$I_p = 16$	$I_p = 24$	$I_p = 32$	$I_p = 40$
Maximum	54	55	53	53	54	54
Minimum	47	47	45	47	47	46
Mean value	50	49	48	50	50	49

Table 4.25: DMPC bilayer area per lipid ($Å^2$).

Order parameter.

Impulse $(Pa \cdot s)$	$I_p = 0$	$I_p = 8$	$I_p = 16$	$I_p = 24$	$I_p = 32$	$I_p = 40$
Maximum	0.23	0.24	0.25	0.25	0.24	0.25
Minimum	0.21	0.21	0.21	0.21	0.21	0.21
Mean value	0.22	0.23	0.23	0.23	0.23	0.23

Table 4.26: DMPC bilayer order parameter.

Lateral diffusion.

Impulse $(Pa \cdot s)$	$I_p = 0$	$I_p = 8$	$I_p = 16$	$I_p = 24$	$I_p = 32$	$I_p = 40$
Lateral diffusion	10.71	7.48	7.23	5.16	10.53	10.68

Table 4.27: DMPC bilayer lateral diffusion $(10^{-7} \cdot \frac{cm^2}{s})$.

Results for the DPPC bilayer.

Thickness of the membrane.

Impulse $(Pa \cdot s)$	$I_p = 0$	$I_p = 8$	$I_p = 16$	$I_p = 24$	$I_p = 32$	$I_p = 40$
Maximum	49.07	44.23	46.10	53.47	44.10	56.17
Minimum	38.12	36.39	37.93	36.87	38.41	38.06
Mean value	42.78	39.43	41.27	43.73	41.40	45.47

Table 4.28: DPPC bilayer thickness (Å).

Area per lipid.

Impulse $(Pa \cdot s)$	$I_p = 0$	$I_p = 8$	$I_p = 16$	$I_p = 24$	$I_p = 32$	$I_p = 40$
Maximum	74	77	77	78	78	77
Minimum	58	59	59	60	59	58
Mean value	66	67	69	70	69	68

Table 4.29: DPPC bilayer area per lipid ($Å^2$).

Order parameter.

Impulse $(Pa \cdot s)$	$I_p = 0$	$I_p = 8$	$I_p = 16$	$I_p = 24$	$I_p = 32$	$I_p = 40$
Maximum	0.15	0.16	0.16	0.16	0.16	0.16
Minimum	0.09	0.09	0.11	0.10	0.09	0.10
Mean value	0.12	0.12	0.12	0.12	0.11	0.12

Table 4.30: DPPC bilayer order parameter.

Lateral diffusion.

Impulse $(Pa \cdot s)$	$I_p = 0$	$I_p = 8$	$I_p = 16$	$I_p = 24$	$I_p = 32$	$I_p = 40$
Lateral diffusion	193.61	254.35	290.61	268.17	215.59	191.37

Table 4.31: DPPC bilayer lateral diffusion $(10^{-7} \cdot \frac{cm^2}{s})$.

Results for the POPE bilayer.

Thickness of the membrane.

Impulse $(Pa \cdot s)$	$I_p = 0$	$I_p = 8$	$I_p = 16$	$I_p = 24$	$I_p = 32$	$I_p = 40$
Maximum	59.26	58.38	60.04	58.05	55.96	57.91
Minimum	50.92	50.97	51.17	51.32	50.17	50.88
Mean value	55.69	55.01	55.68	54.53	52.62	54.44

Table 4.32: POPE bilayer thickness (Å).

Area per lipid.

Impulse $(Pa \cdot s)$	$I_p = 0$	$I_p = 8$	$I_p = 16$	$I_p = 24$	$I_p = 32$	$I_p = 40$
Maximum	46	52	44	48	49	46
Minimum	40	39	38	41	41	38
Mean value	43	47	41	44	45	42

Table 4.33: POPE bilayer area per lipid ($Å^2$).

Order parameter.

Impulse $(Pa \cdot s)$	$I_p = 0$	$I_p = 8$	$I_p = 16$	$I_p = 24$	$I_p = 32$	$I_p = 40$
Maximum	0.21	0.21	0.21	0.21	0.22	0.22
Minimum	0.16	0.15	0.15	0.17	0.16	0.16
Mean value	0.18	0.18	0.18	0.18	0.18	0.18

Table 4.34: POPE bilayer order parameter.

Lateral diffusion.

Impulse $(Pa \cdot s)$	$I_p = 0$	$I_p = 8$	$I_p = 16$	$I_p = 24$	$I_p = 32$	$I_p = 40$
Lateral diffusion	1.68	5.31	2.74	7.87	6.85	6.49

Table 4.35: POPE bilayer lateral diffusion $(10^{-7} \cdot \frac{cm^2}{s})$.

4.4.5 Discussion.

Even though we would not like to considered this as a validation, a discussion of the obtained results for this group of simulations will be discussed here.

The transient effect is well simulated for all these calculations as can be seen in the representation of its associated values, such as kinetic energy, temperature and volume. Consistently, the figures show an increase proportional to the impulse and a positive trend.

In the case of the DMPC bilayer, the thickness values are around 40 and 43 Å (41.95 Å without shock wave) which agrees fairly well with other reported experimental values [101].

On the other hand, the area per lipid, i.e. between 48 and 50 Å^2 (50 Å^2 without shock wave) is slightly low when compared with other reported values [91], which implies an overgenerous density while the order parameter and diffusion results, around 0.2 and $10^{-7} \cdot \frac{cm^2}{s}$, can be well accepted.

However, in the case of the DPPC bilayer, the results became unacceptable, as thickness values, around 39 and 46 Å (42.78 Å without shockwave), disagree with results presented by other authors [102], and the same occurs with the area per lipid, between 66 and 69 Å^2 (66 Å^2 without shock wave) [93]. The

values for the order parameter and the lateral diffusion made no sense. This computation must be considered unsuccessful.

The case of the POPE bilayer is much better. However the values of thickness between 52 and 56 Å (55.69 Å without shock wave) and area per lipid between 41 and 47 Å^2 (43 Å^2 without shock wave) are slightly different from results published by other authors [96]. On the other hand, the order parameter is slightly low and, even though the lateral diffusion can be considered acceptable as it is in the usual order of magnitude, it is not consistent.

As it can be seen the results for lateral diffusion are well accepted as long as the values are in the order of magnitude of $10^{-7} \cdot \frac{cm^2}{s}$, which occurs for the case of DMPC and POPE bilayers. However, in the case of the DPPC bilayer, the results, 2 orders of magnitude over this value, must considered unacceptable. No trend for the values of lateral diffusion has been found in this lot of computations.

In conclusion, the *Molecular Dynamics* computations can be rather sensitive to initial conditions, so the analysis of the generated model and its related values is quite important in order to achieve precise, useful results. Neatness in the *Molecular Dynamics* model which is going to be used for the calculations is, therefore, essential.

Chapter 5

Mass flow through the alveolar surface

From an experimental point of view, the structure of the alveoli and the way this gas exchange is done, are still matters of research and controversy. This is mostly, because the microscopic studies require fixation of tissues using different acids which alters their morphology.

Tannic acid is used in the case of visualising lipid structures, this acid may cause surface-active phospholipid (SAPL) migration [103] which introduces even more confusion regarding the alveolar structure.

During recent decades, several models have been developed in order to explain the alveolar structure and operation.

- The bubble model [66].

  Widespread accepted for over 40 years, it works on the principle that the alveoli are normally covered with liquid forming an air-liquid interface with the alveolar gas, the only place where surfactant is assumed to be located as a surface of constant thickness.

  However, since the only stable liquid-gas interface, according to basic physics, is the sphere, this model could not explain alveolus as non-spherical structures.

- The morphological model [67].

  Starting from the point of surfactant thickness variation all along the alveolar surface, morphological studies led to the definition of concave fluid free areas as well as convex areas with excess of fluid.

This model led to a self-regulating alveolar fluid control to resolve the accumulation of surfactant in the convex areas.

- The foam model [68].

  The alveolar surface, defined as an agglomeration of bubbles, fills the bronchioles end in the form of alveolar sacs. These are complete surfactants containing films which surround units of alveolar gas.

  This is opposite to the other two models which accept bubble segments or one-sided bubbles.

- The geodesic model.

  Opposite to the bubble model, where a continuous lining for the alveolar surface was implicit, a solid phase of DPPC is assumed. The surface activity of these lipids, identified in the lung in 1946 [69], was demonstrated in the 1920s [70].

  In the process of expiration, the lipids of the membrane can come together in order to generate a solid geodesic dome rigid structure [71] while they can expand in inhalation.

In order to study the mass flow through this biological membrane, a *Molecular Dynamics* model made by DPPC phospholipids, pulmonary gas and surfactant can simulate the behaviour of an alveolar surface with *Molecular Dynamics* precision. This could bring some more light into this extremely complex and spellbinding subject.

Unfortunately, the Cranfield University HPC facilities were not available for this experiment and a 1.86 GHz 64 bit single processor desktop computer with 3.25 GB of RAM had to be used.

Using an NPT minimisation followed by an NVE simulation ensemble, the alveolar surface model described in section 3.3 was computed in order to analyse the respiration process through the alveola and will be described later.

This computational scheme allows the target values, pressure and temperature, to be set at the minimisation process to compute the simulation into the microcanonical ensemble with volume and energy conservation guaranteed.

5.1 Minimisation.

As well as in the case of the POPC model, section 4.1.1, and in order to relieve strain in experimentally obtained conformations [87], an initial minimisation of the model is computed before carrying out the simulation.

The process has been done for 50 ps in three stages described as follows:

1. Minimisation for 6 ps.
2. Temperature and pressure increment for 4 ps.
3. Volume equilibration for 40 ps.

The conditions inside the lung have been recreated following a well published transpulmonary Pressure-Volume function [104], which is the representation of the mathematical general expression shown in equation 5.1.

$$P = \frac{k_1}{V_M - V} + \frac{k_2}{V_m - V} + k_3 \tag{5.1}$$

This is a hyperbolic-sigmoid function derived from data of human subjects covering from Total Lung Capacity (TLC) to Residual Volume (RV) irrespective of the interpretation of inflection points below the Functional Residual Capacity (FRC) with an esophageal balloon. The human constants have been evaluated using least-squares non-linear regression.

As this ensemble will allow the setting of the pressure variables of the model to chosen target values, as explained in 2.3, the quantities obtained from this curve will be used for the NPT ensemble, in order to carry out the three minimisations of the model. In this case, the calculations have been done for the values at the extreme of the respiration process (minimum and maximum pressure) and for atmospheric pressure. Their representation is shown in figure 5.2.

In doing so, it is possible to analyse the behaviour of the model for different conditions and compare the results. This will provide more information about the process, rather than running a single simulation.

The representation of the minimisations for the different conditions of pressure are shown in figure 5.2. It can be seen that none of the air particles crosses the membrane in this process.

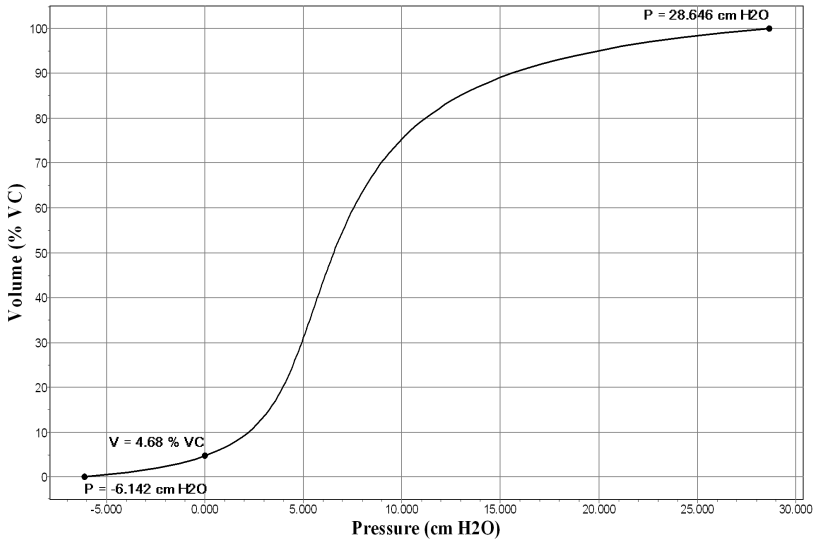

Figure 5.1: Transpulmonary pressure-volume function.

5.2 Simulation.

Once the model is minimised for all the chosen conditions, the latest coordinates and velocities of the atoms for the simulation can be used.

As has been pointed before, the stability of the lipid bilayer system is susceptible to the starting conditions [89] and an analysis of the variables result of the calculation is needed to verify its reliability.

This computation scheme of different minimisation processes will make possible a better analysis of the calculation as more results will be obtained and compared with values published by other authors.

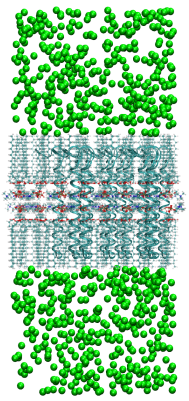

(a) Initial condition.

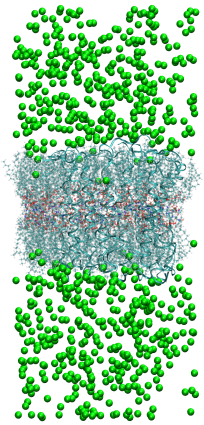

(b) End for minimum pressure.

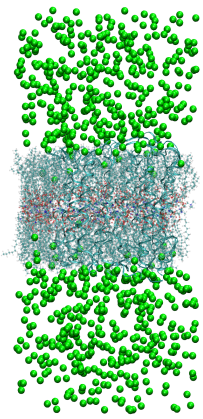

(c) End for atmospheric pressure.

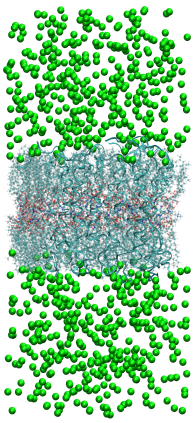

(d) End for maximum pressure.

Figure 5.2: Alveolar surface minimisations.

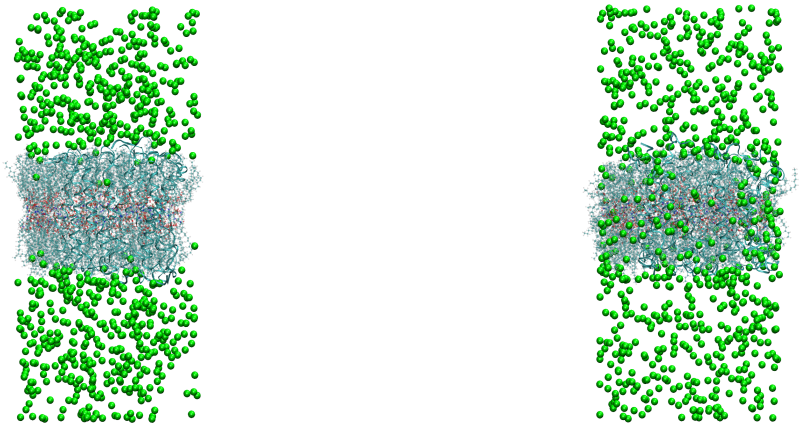

(a) Initial condition. (b) End of simulation.

Figure 5.3: Alveolar surface simulation for minimum pressure.

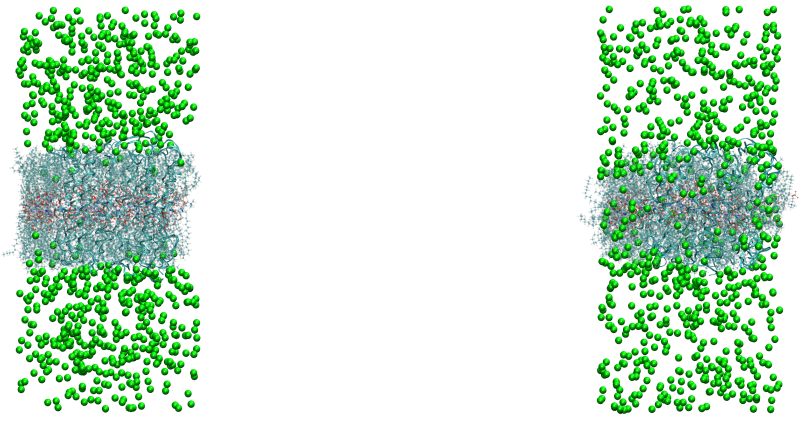

(a) Initial condition. (b) End of simulation.

Figure 5.4: Alveolar surface simulation for atmospheric pressure.

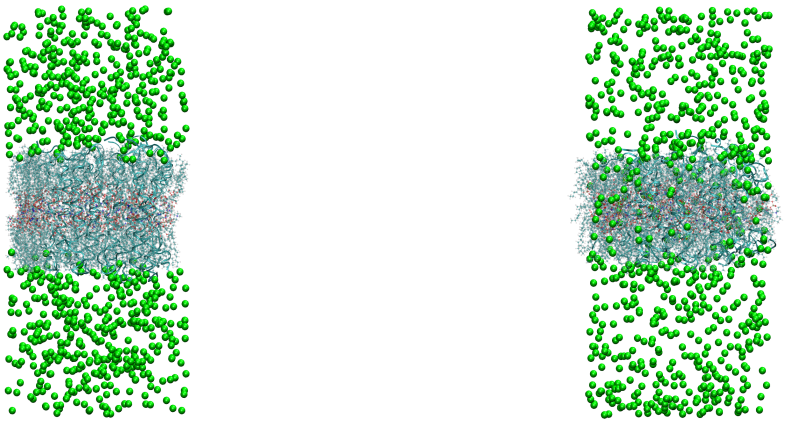

(a) Initial condition.

(b) End of simulation.

Figure 5.5: Alveolar surface simulation for maximum pressure.

5.3 Analysis.

5.3.1 Temperature and energies.

The representation of the energies does not provide interesting results for the analysis, but for the reliability of the simulation.

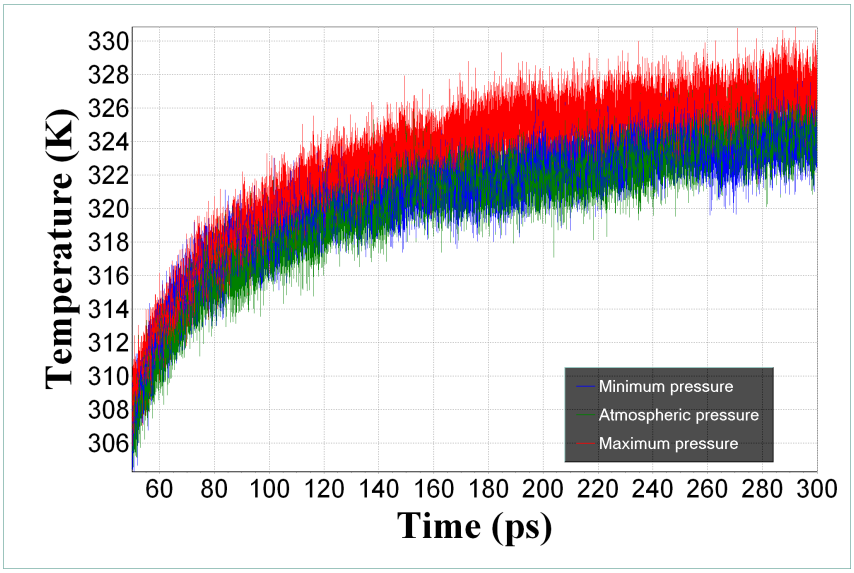

Figure 5.6: Alveolar surface temperature.

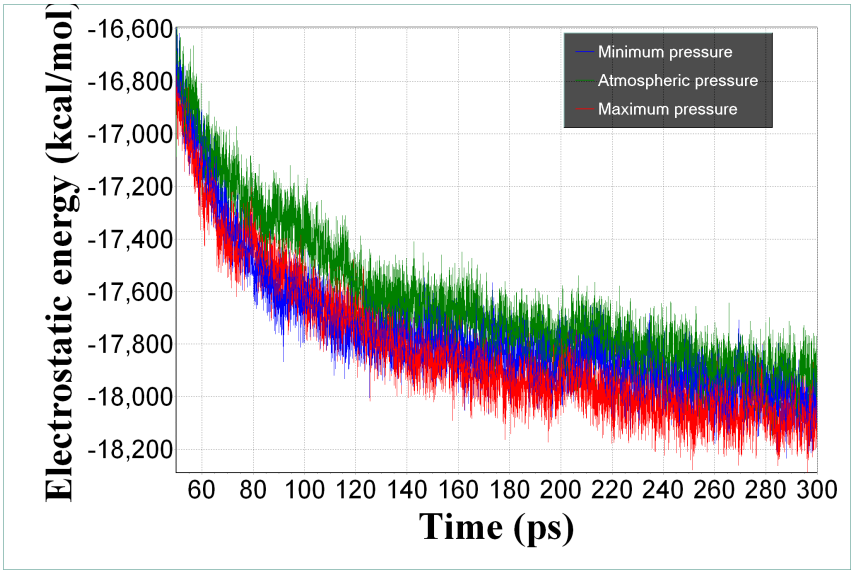

Figure 5.7: Alveolar surface electrostatic energy.

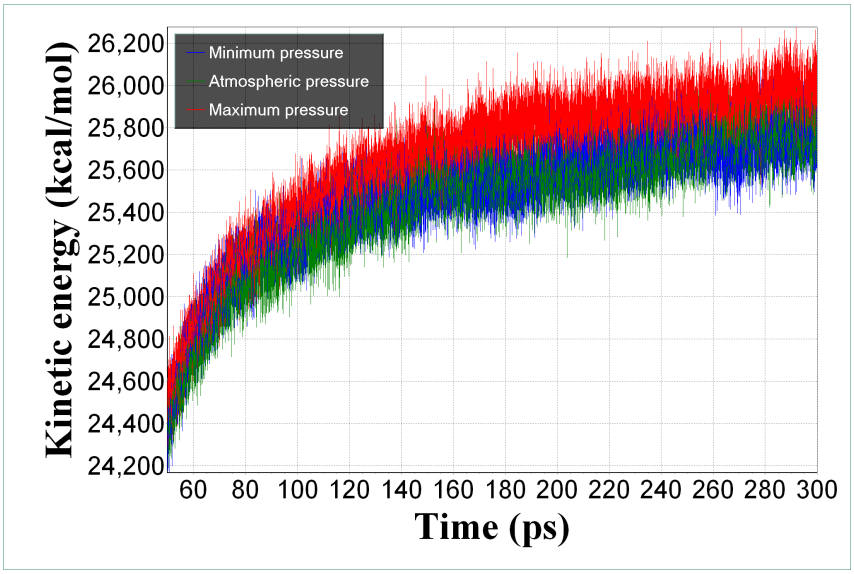

Figure 5.8: Alveolar surface kinetic energy.

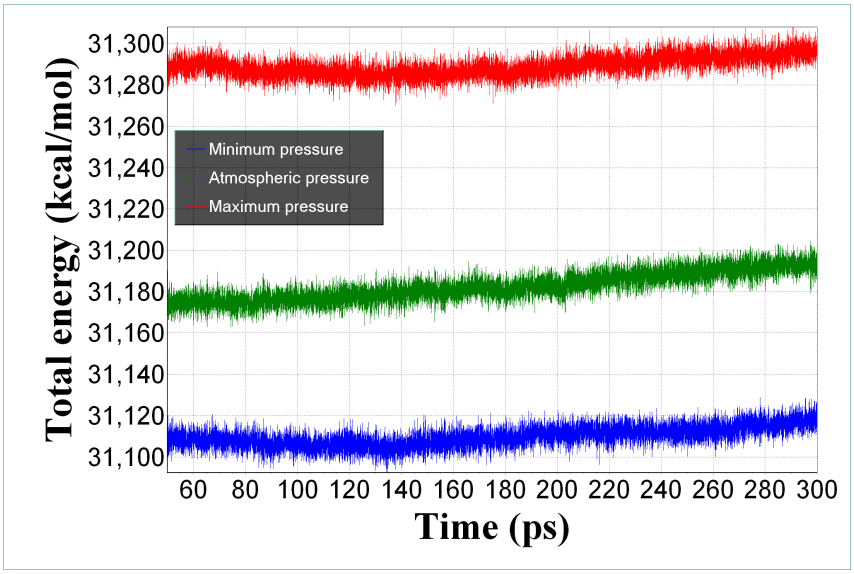

Figure 5.9: Alveolar surface total energy.

The different representations show a smooth progressive function for all the variables involved.

This is all fine from the numerical point of view and it indicates a successful experiment. On the other hand, if the lipid membrane were not kept stable,

the curves on the graphics would jump into random shapes and a membrane break would be observed in the 3D representations of the simulation.

The results have to be checked in order to ensure agreement with the physical process though.

5.3.2 Thickness of the membrane and area per lipid.

The representation of the thickness (figure 5.10) and the total area in the plane of the bilayer (figure 5.11) are shown for each time step. A normal evolution of the values is observed.

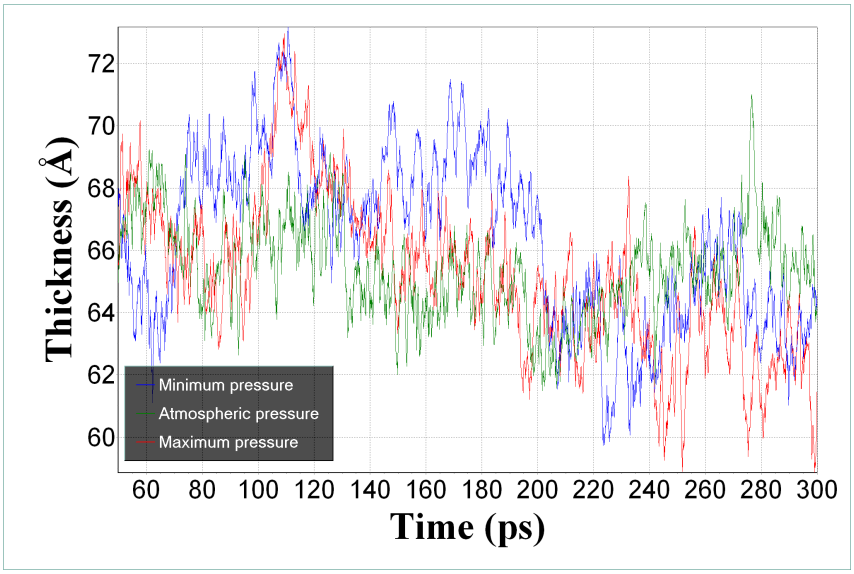

Figure 5.10: Alveolar surface film thickness.

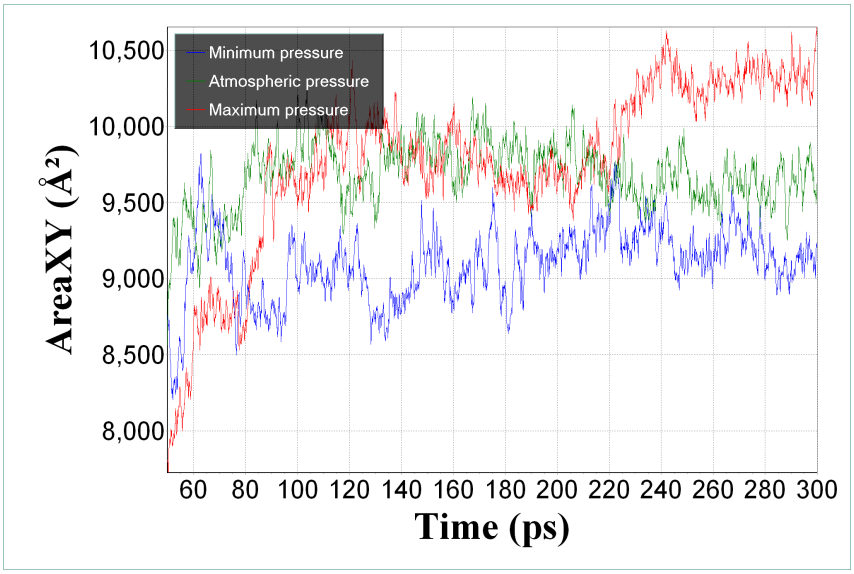

Figure 5.11: Alveolar surface area in the plane of the layers.

The obtained values are shown in tables 5.1 and 5.2.

	Minimum pressure	Atmospheric pressure	Maximum pressure
Maximum	73.17	71.00	72.96
Minimum	59.73	61.48	58.85
Mean value	66.36	65.42	65.23

Table 5.1: Alveolar surface thickness (Å).

	Minimum pressure	Atmospheric pressure	Maximum pressure
Maximum	76.73	80.01	83.22
Minimum	64.10	66.89	60.35
Mean value	71.07	75.64	76.29

Table 5.2: Alveolar surface area per lipid in the plane of the layers.

These values will allow the comparison of the computation with other values later, as it will be explained in section 5.4.

5.3.3 Lateral diffusion and mass flow.

The permeation process of molecules across lipid bilayers is an interesting topic for study with *Molecular Dynamics*, as the equilibrium concentration in the membrane is too low to be detected experimentally [76].

The results for each time step have been represented in figure 5.12. A normal lateral diffusion of the lipids is observed in the trace of the centre of mass, while its permeability to air is confirmed.

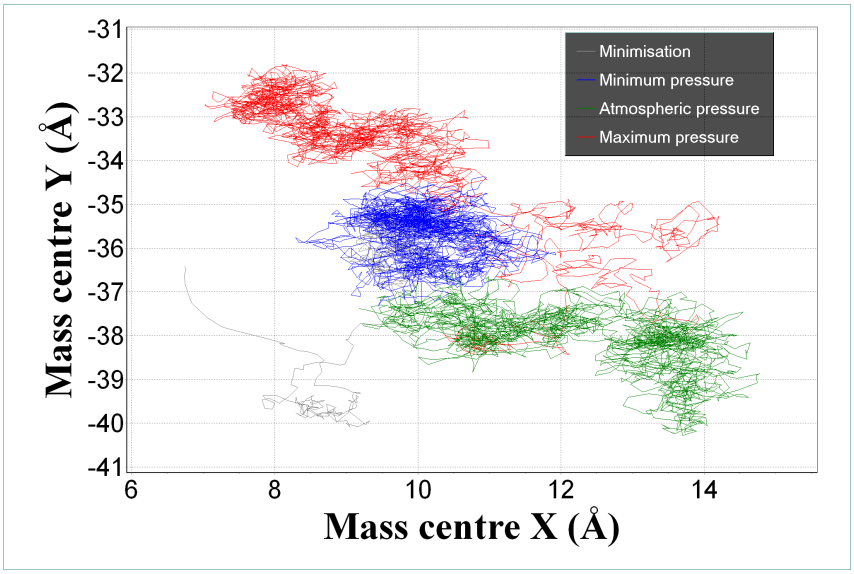

Figure 5.12: Alveolar surface centre of mass.

The obtained values are shown in tables 5.3 and 5.4.

	Minimum pressure	Atmospheric pressure	Maximum pressure
Lateral diffusion	11.45	14.77	18.08

Table 5.3: Alveolar surface lateral diffusion ($10^{-7} \cdot \frac{cm^2}{s}$).

As a preferential flow for the air particles has not been defined, there is not conclusion about the direction of the mass flow which is not the objective of this simulation. The initial velocity values has been set to random values and the particles flow in any direction.

It has been observed an inverted flow for the case of maximum pressure

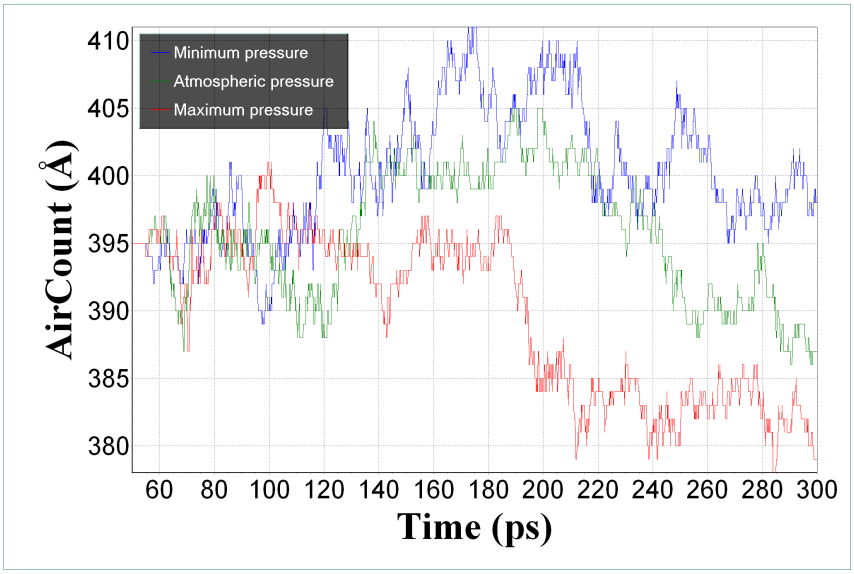

Figure 5.13: Alveolar surface flow through the membrane.

	Minimum pressure	Atmospheric pressure	Maximum pressure
Maximum	16	10	6
Minimum	-6	-9	-17
Mean value	5	1	-5
Difference	22	19	23

Table 5.4: Alveolar surface mass flow.

(-5), contrasting with the case of minimum pressure (+5) which does not yield any conclusion as the aim of this simulation is to observe the stability of this kind of membrane for the experimental conditions pointing to the possibility of its existence in the human body.

5.4 Discussion.

The validation of the results obtained for the alveolar surface is slightly more complicated than those undertaken in previous chapters because of the controversy all around this biological structure.

A value for the thickness of this membrane can be obtained from the

Scarpelli studies [25] which point to a value of 7 nm agreeing with the presented computations (65.42 Å for the case of atmospheric pressure).

The area in the plane of the bilayer is affected by the temperature and, as an NVE ensemble has been used, there is no control for this value after the minimisation process. In order to compare the results the beginning of the simulation must be focused on when the temperature is in the corporeal range.

In any case, the obtained values, around 70 Å, are in fair agreement with those presented by other authors for DPPC bilayers [105] [106] [107] [108] [109] and monolayers [110].

The lateral diffusion seem to be slightly high compared with the values presented by other authors for DPPC bilayers [100]. However, it must be taken into account that this is not a bilayer, as heads of the phospholipids are pointing inwards and instead of water, air molecules are placed on and under the DPPC layers.

On the other hand, the obtained value for atmospheric pressure, $14.77 \cdot 10^{-7} \frac{cm^2}{s}$, agrees with other studies for DPPC monolayers [110].

5.5 Conclusions.

This *Molecular Dynamics* calculation has successfully simulated the inter-alveoli gas exchange, becoming a numerical recreation of the operation of the pulmonary membranes.

As it was presented, two DPPC layers placed head to head representing the membranes of two alveoli, two groups of air particles in contact with their hydrophobic tails and embedded surfactant into the membranes, can generate a stable physical system.

The obtained geometrical properties of this system are in fair agreement with other studies as it is pointed out in section 5.4.

A permeability to air of the membranes has been observed through this lipid-surfactant system permitting a gas exchange. The air particles can cross through the DPPC membrane allowing the respiration process.

Therefore, a numerical recreation virtual experiment for a pulmonary membrane behaviour has been computed using *Molecular Dynamics* techniques and

the obtained results can explain behaviours which might fit into a biological scheme lighting a possible procedure to explain missing data in experimental analysis.

This lipid-protein membrane model numerically demonstrates the possibility of air flow through a stable two-layered DPPC phospholipid structure either from a numerical or physical and biological point of view and the existence of an alveolar membrane at the end of the bronchial tubes.

Chapter 6

Concluding overview

The studies on biological membranes include a wide variety of phenomena which can be approached using diverse techniques whether experimental or not. In this document, the *Molecular Dynamics* method has been successfully applied to simulate different situations of interest regarding the flow and mass transport through a biological membrane.

Several studies over a variety of phospholipid membranes with and without embedded proteins have been successfully computed and the simulation of the shock wave interaction was properly introduced, as described in Chapter 4, and published (See at the end of the bibliography section).

It was also possible to undertake the simulation of mass transport through a biological membrane. This calculation, described in chapter 5, was successfully computed and published.

In the first of the studies, a scheme of NPT minimisation, shock wave application and NPT simulation has been followed. This study has been validated by comparing the obtained results with others from different authors in both the experimental and computational fields.

The important conclusion of all those calculations is that an interaction of shock waves with biological cell membranes can generate a permeability for a limited short period of time or transient in which a proportional increase of the lateral diffusion is observed. Even though it has been proved experimentally, a numerical demonstration had not been demonstrated until this study.

Other effects of the interaction of the shock wave with the cell membrane

have been observed in the analysis of several variables such as kinetic energy, temperature, thickness, area, volume and order parameter.

As it was expected, an increase in the kinetic energy, temperature and volume proportional to the impulse could be observed for the NPT ensemble in an interval of a few picoseconds after the application of the shock wave. This phenomena comes from the change in the momentum of the water molecules of the top water layer.

It is precisely this temporal increase of the volume, the key process for the increase of permeability across the cell membrane as both permeability and lateral diffusion are strongly affected by the amount and distribution of free volume or area in a membrane (space not occupied by phospholipids) and it is reasonable to expect that the changes in these properties are somehow coupled [33].

In the case of the thickness, only an increase in the fluctuation range seems to be related to the impulse of the shock wave, however, as in the analysis of the area and the order parameter, the value does not seem to be affected by the shock wave in long term and the molecules come back to their equilibrium position.

In the second of the studies over the interaction of shock waves with biological cell membranes, the *Molecular Dynamics* scheme was completely different as the NPT ensemble is used only in the minimisation process and the simulation is made as microcanonical (NVE).

This kind of simulation does not allow change on the control volume along the simulation, which remains constant. That is why it has not been possible to simulate the transient process, the obtained results could not be validated and no conclusion can be derived from the resulting lateral diffusion parameters. Advice against using the NVE ensemble for this kind of simulation is, therefore, strongly recommended.

Many more simulations and results have been presented within this document, see chapter 4.4. Unfortunately, their computational cost made it practically impossible to have a proper tune up of the models. Nevertheless, a brief discussion of the obtained results can be read in subsection 4.4.5.

The last of the studies about the alveolar surface refers to another biological structure. In this case, there is no shock wave interaction and the interest of this research is focused on the mass transport through lipid membranes.

This lipid-protein membrane model can serve as a virtual experiment in order to solve the controversy about the alveolar surface. It points to the possibility of air flow through a stable two-layered DPPC phospholipid structure either from a numerical or physical and biological point of view and the existence of an alveolar membrane at the end of the bronchial tubes.

More aspects of these phenomena and their conclusions can be found in the author's publications referenced in appendix III.

Chapter 7

Future work

The calculations presented in this document are just a few possibilities of what *Molecular Dynamics* can do at the present time and it is hoped that other researchers will be encouraged to continue with even more experiments to increase this precious knowledge about these fascinating biological phenomena. Their applications and importance go beyond our actual imagination.

Technical advances and faster computers will make possible more precise, long and complex *Molecular Dynamics* models, simulations and analysis, increasing knowledge about the studied processes. At the same time, there is plenty of options for future work, comprising:

1. Introduction of other biological structures into the cell membrane model, such as proteins, cholesterol, glycolipids, carbohydrates or filaments of cytoskeleton in other to analyse its behaviour and influence in the membrane processes and cancer chemotherapy.

2. Simulation of microvilli: Formation, behaviour, evolution, affection and relation to the disease of cancer. It seems so be quite related to cancer cells as it grows widely on these ones.

3. Longer computations and richer models will allow the study of more precise and larger time scale processes. The previous small high performance facilities of Cranfield University have been widely improved, so longer time scale cellular processes could be studied and more relevant results about this matter could be obtained. Unfortunately, there was not a chance to use it during this PhD and take advantage of the latest *Molecular Dynamics* hardware and software implementations, the reliability of calculations and the precision of the models will be improved.

4. Simulation of one or more whole cells as spherical-shaped structures will allow the study of the interaction among the cells and bulk properties analysis, as well as a detailed study of the cell behaviour or a group of cells.

5. Simulation of mass flow across the alveolar membrane at differential pressure and introduction of preferential flows in order to achieve a more realistic idea of the respiration process.

6. Studies about the shock wave effect on gas diffusion across membranes.

7. More detailed models of biological fluids including the different molecules involved and their interaction with the cell membrane can be generated. In this study, it was necessary to use simplified models for the fluids in order to save computation time and a detail analysis of the behaviour of its components is missing. By the other hand, modelling of biological fluids, such as blood or air, will allow more precise calculations and better approximations to the processes involved.

8. Pre-processing can be achieved by generating more utilities to build the *Molecular Dynamics* models. This initial task usually requires the generation programs for the generation of the particular model as there is not a general computer package for that task.

9. Post-processing algorithms can be developed in order to calculate more results from the *Molecular Dynamics* simulations and studied processes. This task is usually complicated because of the size of the result files, which need long time to be processed. Further calculations can be made in order to get more information from the obtained results, this is permeability, shear strengths, local pressure, cavitation, shock wave damage thresholds, shock wave representation. These calculations often need longer *Molecular Dynamics* simulations, in the order of ns, to get acceptable values.

10. Analysis of other different processes into the biological world will allow the execution of *Molecular Dynamics* virtual experiments in order to compare with experimental results.

Bibliography

[1] J.N. Weinstein, D.M. Oster, J.B. Park, S.H. Park, and S. Loening. The effect of the extracorporeal shock wave lithotripter on the bone-cement interface in dogs. *Clinical Orthopaedics and Related Research*, 235:261–267, 1988.

[2] Valchanou V.D. and Michailov P. High energy shock waves in the treatment of delayed and nonunion of fractures. *International Orthopaedics*, 15(3):181–184, 1991.

[3] G. Haupt. Use of extracorporeal shock waves in the treatment of pseudarthrosis, tendinopathy and other orthopedic diseases. *The Journal of Urology*, 158(1):4–11, 1997.

[4] M. Kambe, N. Ioritani, S. Shirai, K. Kambe, M. Kuwahara, D. Arita, T. Funato, H. Shimadaira, M. Gamo, and S. Orikasa. Enhancement of chemotherapeutic effects with focused shock waves: Extracorporeal shock wave chemotherapy (eswc). *In Vivo*, 10(3):369–375, 1996.

[5] M. Kambe, N. Ioritani, S. Shirai, K. Kambe, F. Tekuza, M. Kaji, T. Saito, Y. Murakami, M. Kuwahara, T. Funato, M. Gamo, K. Takayama, S. Orikasa, and R Kanamaru. Microscopic pores opened by shock wave on cancer cell surfaces: Morphological and functional features. *Journal of Endouroly*, 9:161–167, 1996.

[6] C.P. Lin, M.W. Kelly, S.A.B. Sibayan, M.A. Latina, and R.R. Anderson. Selective cell killing by microparticle absorption of pulsed laser radiation. *IEEE Journal of Selected Topics in Quantum Electronics*, 5(4):963–968, 1999.

[7] C. Chaussy, E. Schmiedt, D. Jocham, W. Brendel, B. Forssmann, and V. Walther. First clinical experience with extracorporeally induced destruction of kidney stones by shock waves. *The Journal of Urology*, 167(5):1957–1960, 2002.

[8] H. Reichenberger. Lithotripter systems. *Proceedings of the IEEE*, 76(9):1236–1246, 1988.

[9] T.M. Richardson, S.V. Brown, J.V. Thomas, and R.J. Simmons. Shock wave effect on anterior segment structures following experimental neodymium: Yag laser iridectomy. *Ophthalmology*, 92(10):1387–1395, 1985.

[10] A.G. Doukas, D.J. McAuliffe, and T.J. Flotte. Biological effects of laser-induced shock-waves: Structural and functional cell damage in vitro. *Ultrasound in Medicine and Biology*, 19(2):137–146, 1993.

[11] S.M. Lee, D.J. McAuliffe, H. Zhang, Z. Xu, J. Taitelbaum, T.J. Flotte, and A.G. Doukas. Stress-wave-induced membrane permeation on red blood cells is facilitated by aquaporins. *Ultrasound in Medicine and Biology*, 23(7):1089–1094, 1997.

[12] F. Brümmer, Th. Bräuner, and Hülser D.F. Biological effects of shock waves. *World Journal of Urology*, 8:224–232, 1990.

[13] T. Kodama, M.R. Hamblin, and A.G. Doukas. Cytoplasmic molecular delivery with shock waves: Importance of impulse. *Biophysical Journal*, 79(4):1821–1832, 2000.

[14] R. Lawaczeck. On the permeability of water molecules vesicular lipid bilayers. *Journal of Molecular Biology*, 51:229–261, 1979.

[15] T.J. Flotte, S. Lee, H. Zhang, D. McAuliffe, T. Douki, and A. Doukas. Laser-induced enhancement of citoxity: A new approach to cancer therapy. *Laser-Tissue Interactions IV*, 2391:202–207, 1995.

[16] T.J. Flotte, T. Anderson, D.J. McAuliffe, T. Hasan, and A.G. Doukas. Laser-induced enhancement of citoxity: A new approach to cancer therapy. *Laser-Tissue Interactions IV*, 1882:122–129, 1993.

[17] E.F. Carome, N.A. Clark, and C.E. Moelle. Generation of acoustic signals in liquids by ruby laser-induced thermal stress gradients. *Applied Physics Letters*, 4(6):95–97, 1964.

[18] E.F. Carome, C.E. Moeller, and Clark N.A. Intense ruby-laser-induced acoustic impulses in liquids. *The Journal of the Acoustical Society of America*, 40(6):1462–1466, 1966.

[19] S. Fine, E. Klein, W. Nowak, R.E. Scott, Y. Laor, L. Simpson, J. Crissey, J. Donoghue, and V.E. Deer. Interaction of laser radiation with biological

systems i. studies of interactions with tissues. *Federation of Societies for Experimental Biology*, 24:S35–S45, 1965.

[20] K. Takayama. Applications of shock wave research to medicine. *22nd International symposium on shock waves, Imperial college, London*, 2010:23–32, 1999.

[21] L. Saiz and M.L. Klein. Computer simulation studies of model biological membranes. *Accounts of Chemical Research*, 35(6):482–489, 2002.

[22] A. Blume. *Phospholipids Handbook*, chapter Dynamic properties, pages 455–552. Marcel Dekker, New York, 1993.

[23] K. Koshiyama, T. Kodama, M.R. Hamblin, A.G. Doukas, T. Yano, and S. Fujiyama. Molecular delivery into a lipid bilayer with a single shock wave using molecular dynamic simulation. In G.R. ter Haar and I. Rivends, editors, 4^th *International Symposium on Therapeutic Ultrasound*, volume 754, pages 104–106. American Institute of Physics, September 2004.

[24] Leff A.R. and P.T. Schumaker. *Respiratory physiology: Basics and applications*. W.B. Saunders Co., Philadelphia, 1993.

[25] E.M. Scarpelli. The alveolar surface network: A new anatomy and its physiological significance. *The Anatomical Record*, 251(4):491–527, 1998.

[26] P.C. Jost, H. Griffith, O, R.A. Capaldi, and G. Vanderkooi. Evidence for boundary lipid in membranes. *Proceedings of the National Academy of Sciences of the United States of America*, 70(2):480–484, 1973.

[27] S.J. Singer and G.L. Nicolson. The fluid mosaic model of the structure of cell membranes. *Science*, 175(4023):720–731, 1972.

[28] S. Marrink and J.C. Berendsen. Simulation of water transport through a lipid membrane. *The Journal of Physical Chemistry*, 98(15):4155–4168, 1994.

[29] A.G. Doukas, D.J. McAuliffe, S. Lee, V. Venugopalan, and T.J. Flotte. Physical factors involved in stress-wave-induced cell injury: The effect of stress gradient. *Ultrasound in Medicine and Biology*, 21(7):961–967, 1995.

[30] D.W. Deamer and J. Bramhall. Permeability of lipid bilayers to water and ionic solutes. *Chemistry and Physics of lipids*, 40(2):167–188, 1986.

[31] P. Harris and Presles H.N. The shock induced electrical polarization of water. *Journal of Chemical Physics*, 77(10):5157–5164, 1982.

[32] P. Devaux and H.M. McConnell. Lateral diffusion in spin-labeled phosphatidylcholine multilayers. *Journal of the American Chemical Society*, 94(13):4475–4481, 1972.

[33] Emma Falck, M. Patra, M. Karttunen, M.T. Hyvönen, and I. Vattulainen. Lessons of slicing membranes: Interplay of packing, free area, and lateral diffusion in phospholipid/cholesterol bilayers. *Biophysical Journal*, 87(2):1076–1091, 2004.

[34] P. Steinbach, F. Hofstädter, H. Nicolai, W. Rössler, and W. Wieland. In vitro investigations on cellular damage induced by high energy shock waves. *Ultrasound in Medicine and Biology*, 18(8):691–699, 1992.

[35] S.E. Mulholland, S. Lee, D.J. McAuliffe, and A.G. Doukas. Cell loading with laser-generated stress waves: The role of the stress gradient. *Pharmaceutical Research*, 16(4):514–518, 1999.

[36] S. Lee and A.G. Doukas. Laser-generated stress waves and their effects on the cell membrane. *IEEE Journal of Selected Topics in Quantum Electronics*, 5(4):997–1003, 1999.

[37] S.F. Cleary. Laser pulses and the generation of acoustic transients in biological material. *Laser Applications in Medicine and Surgery*, 3:175–219, 1977.

[38] A.G. Doukas and T.J. Flotte. Physical characteristics and biological effects of laser-induced stress waves. *Ultrasound in Medicine and Biology*, 22(2):151–164, 1996.

[39] D.A. Hutchins. *Physical Acoustics*, volume XVIII, chapter Ultrasonic generation by pulsed lasers, pages 21–123. Academic Press, New York, 1988.

[40] G.E. Duvall and G.R. Fowles. *High pressure physics and chemistry*, volume II, chapter Shock wave, pages 201–291. Academic Press, New York, 1963.

[41] J. Fueyo, C. Gomez-Manzano, A. Yung, and A. Kyritsis. Targeting in gene therapy for gliomas. *Archives of Neurology*, 56(4):445–448, 1999.

[42] L. Barbieri, L. Polito, A. Bolognesi, M. Ciani, E. Pelosi, V. Farini, A. Jha, N. Sharma, J.M. Vivanco, A. Chambery, A. Parente, and F. Stirpe.

Ribosome-inactivating proteins in edible plants and purification and characterization of a new ribosome-inactivating protein from cucurbita moschata. *Biochimica et Biophysica Acta*, 1760:783–792, 2006.

[43] K. Von Neergaard. New notions on a fundamental principle of respiratory mechanics: The retractile force of the lung, dependent on the surface tension in the alveoli. *Exp. Med.*, 66:373–394, 1929. (Translated from the original for Pulmonary and Respiratory Physiology, Part 1. Comroe, J.R. Jr. Ed. Stroudsburg, PA: Dowden, Hutchinsonand Ross, Inc., 1976).

[44] R.E. Pattle. Properties, function and origin of the alveolar lining layer. *Nature*, 175:11251126, 1955.

[45] R.E. Pattle. Properties, function, and origin of the alveolar lining layer. *Proceedings of the Royal Society of London. Series B, Biological Sciences*, 148(931):217–240, 1958.

[46] E.M. Scarpelli. R.e. pattle and the discovery of lung surfactant. *American Journal of Perinatology*, 12:377378., 1995.

[47] E.M. Scarpelli. *The Place for New Technologies in Gynecology, Obstetrics and Perinatology*, chapter Pattles discovery (19531955) and early definition of lung surfactant, page 36. Cosmi EV, Bologna, Italy, 1995.

[48] E.M. Scarpelli. *Surfactants and the lining of the lung.* Johns Hopkins University Press, Baltimore, 1988.

[49] E.M. Scarpelli. Intrapulmonary foam at birth: An adaptational phenomenon. *Pediatric Research*, 12(11):1070–1078, 1978.

[50] E.M. Scarpelli, B.C. Clutario, and Traver D. Failure of immature lungs to produce foam and retain air at birth. *Pediatric Research*, 13(11):1285–1289, 1979.

[51] E.M. Scarpelli, A. Kumar, and B.C. Clutario. *Pulmonary surfactant system*, chapter Near-zero surface tension, intrapulmonary foam and lung mechanics, pages 3–16. Elsevier Science Publishers, 1983.

[52] E.M. Scarpelli, B.C. Clutario, A.J. Mautone, and J. Baum. Intrasaccular bubbles of near-zero surface tension stabilize neonatal lungs. *Pflügers Archiv: European Journal of Physiology*, 401(3):287–292, 1984.

[53] E.M. Scarpelli, A.J. Mautone, and Chinoy M.R. Intraalveolar bubbles and bubble films. i. formation and development during the first 48 hours of extrauterine life in rabbits. *The Anatomical Record*, 244(3):344357, 1996.

[54] E.M. Scarpelli, Mautone A.J., D.O. DeFouw, and B.C. Clutario. Intraalveolar bubbles and bubble films. ii. formation in vivo through adulthood. *The Anatomical Record*, 246(3):245270, 1996.

[55] E.M. Scarpelli, A.J. Mautone, M.R. Chinoy, D.O. DeFouw, and B.C. Clutario. Intraalveolar bubbles and bubble films. iii. vulnerability and preservation in the laboratory. *The Anatomical Record*, 248(4):498520, 1997.

[56] E.M. Scarpelli, M.T. Antonio-Santiago, B.C. Clutario, and A.J. Mautone. Fluid dynamics during initial aeration of mature fetal lung and effect of temperature. *Pediatric Pulmonology*, 15(4):235243, 1993.

[57] J.H. Jr. Comroe. *Pulmonary and Respiratory Physiology, Part 1.* Stroudsburg, Pa. Dowden, Hutchinson and Ross, New York, 1976.

[58] J.A. Clements. Surface tension in relation to pulmonary function. *Physiologist*, 2:1128, 1962.

[59] J. Mead, T. Takishima, and D. Lieth. Stress distribution in lungs: A model of pulmonary elasticity. *Journal of Applied Physiology*, 28:596608, 1970.

[60] I.A. Greaves, J. Hildebrandt, and F.G. Jr. Hoppin. *Handbook of physiology, section 3: The respiratory system, Vol. III: Mechanics of breathing, Part 1*, chapter Micromechanics of the lung, page 195210. American Physiological Society, 1986.

[61] D. Stamenovic. Micromechanical foundations of pulmonary elasticity. *Physiological Reviews*, 70:11171134, 1990.

[62] D. Stamenovic, K.R. Lutchen, and G.M. Barnas. Alternative model of respiratory tissue viscoplasticity. *Journal of Applied Physiology*, 75:10621069, 1993.

[63] Wilson TA. Bachofen H. *The lung scientific foundations*, volume 1, chapter Micromechanics of the acinus and alveolar walls, page 11591167. Lippincott-Raven, Philadelphia, 2 edition, 1997.

[64] E.M. Scarpelli. *The Place for New Technologies in Gynecology, Obstetrics and Perinatology*, chapter Form and function of the alveolar surface and the alveolar surface network, page 723. Cosmi EV, Bologna, Italy, 1995.

[65] E.M. Scarpelli and A.J. Mautone. Surface biophysics of the surface monolayer theory is incompatible with regional lung function. *Biophysical Journal*, 67:10801089, 1994.

[66] J.A. Clements and D.F. Tierney. *Handbook of Physiology: Respiration*, volume II, chapter Alveolar instability associated with altered surface tension, pages 1565–1583. American Physiology Society, Washington DC, 1965.

[67] B.A. Hills. An alternative view of the role(s) of surfactant and the alveolar model. *Journal of Applied Physiology*, 87(5):1567–1583, 1999.

[68] E.M. Scarpelli. *Pulmonary physiology of the fetus, newborn, and child*, chapter Perinatal respiration, pages 116–139. Lea and Febiger, 1975.

[69] S.J. Thannhauser, J. Benotti, and N.F. Boncoddo. Isolation and properties of hydrolecithin (dipalmityl lecithin) from lung; its occurrence in the sphingomyelin fraction of animal tissues. *The Journal of Biological Chemistry*, 166:669–675, 1946.

[70] J.B. Leathes. Role of fats in vital phenomena. lecture ii. *Lancet*, 1:853–856, 1925.

[71] A.D. Bangham. Lung surfactant: how it does and does not work. *Lung*, 165(1):17–25, 1987.

[72] J.C. Phillips, R. Braun, W. Wang, J. Gumbart, E. Tajkhorshid, E. Villa, C. Chipot, R.D. Skeel, L. Kal, and K. Schulten. Scalable molecular dynamics with NAMD. *Journal of Computational Chemistry*, 26(16):17811802, 2005.

[73] G.J. Martyna, D. Tobias, and M.L. Klein. Constant pressure molecular dynamics algorithms. *The Journal of Chemical Physics*, 101(5):4177–4187, 1994.

[74] W.G. Hoover. Canonical dynamics: Equilibrium phase-space distributions. *Physical review letters A*, 31(3):1695–1697, 1985.

[75] S.E. Feller, Y. Zhang, R.W. Pastor, and B.R. Brooks. Constant pressure molecular dynamics simulation: The langevin piston method. *The Journal of Chemical Physics*, 103(11):4613–4621, 1995.

[76] D.P. Tieleman, S.J. Marrink, and H.J.C. Berendsen. A computer perspective of membranes: Molecular dynamics studies of lipid bilayer systems. *Biochimica et Biophysica Acta (BBA) - Reviews on Biomembranes*, 1331(3):235–270, 1997.

[77] R.B. Gennis. *Biomembranes : Molecular structure and function.* Springer-Verlag, New York, 1989.

[78] S.E. Feller, G. Gawrisch, and A.D. MacKerell, Jr. Polyunsaturated fatty acids in lipid bilayers: Intrinsic and environmental contributions to their unique physical properties. *Journal of the American Chemical Society*, 124(2):318–326, 2002.

[79] S. Feller and A.D. MacKerell, Jr. An improved empirical potential energy function for molecular simulations of phospholipids. *Journal of Physical Chemistry B*, 104:7510–7515, 2000.

[80] M. Schlenkrich, J. Brickmann, A.D. MacKerell, Jr., and M. Karplus. *Biological Membranes: A molecular perspective from computation and experiment*, chapter Empirical potential energy function for phospholipids: Criteria for parameter optimization and applications, pages 31–81. Birkhauser, Boston, 1996.

[81] B. Guillot. A reappraisal of what we have learnt during three decades of computer simulations on water. *Journal of Molecular Liquids*, 101(1):219260, 2002.

[82] W. Humphrey, A. Dalke, and K. Schulten. VMD - visual molecular dynamics. *Journal of Molecular Graphics*, 14:33–38, 1996.

[83] K. Nag, J. Perez-Gil, M.L.F. Ruano, L.A.D. Worthman, J. Stewart, C. Casals, and K.M.W. Keough. Phase transitions in films of lung surfactant at the air-water interface. *Biophysical Journal*, 74(6):29832995, 1998.

[84] E.W. Lemmon and R.T. Jacobsen. Viscosity and thermal conductivity equations for nitrogen, oxygen, argon, and air. *International Journal of Thermophysics*, 25(1):21–69, 2004.

[85] J. Johansson, T. Curstedt, B. Robertson, and H. Jörnvall. Size and structure of the hydrophobic low molecular weight surfactant-associated polypeptide. *Biochemistry*, 27(10):3544–3547, 1988.

[86] J. Johansson, T. Szyperski, T. Curstedt, and K. Wüthrich. The nmr structure of the pulmonary surfactant-associated polypeptide sp-c in an apolar solvent contains a valyl-rich alpha-helix. *Biochemistry*, 33(19):6015–6023, 1994.

[87] B.R. Brooks, R.E. Bruccoleri, B.D. Olafson, D.J. States, S. Swaminathan, and M. Karpus. CHARMM: A program for macromolecular

energy, minimization and dynamics calculations. *Journal of Computational Chemistry*, 4(2):187–217, 1983.

[88] T. Feigl, B. Vöklein, H. Iro, C. Ell, and T. Schneider. Biophysical effects of high-energy pulsed ultrasound on human cells. *Ultrasound in Medicine and Biology*, 22(9):1267–1275, 1996.

[89] T. Husslein, D.M. Newns, P.C. Pattnaik, Q.F. Zhong, P.B. Moore, and M.L. Klein. Constant pressure and temperature molecular-dynamics simulation of the hydrated diphytanolphosphatidycholine lipid bilayer. *The Journal of Chemical Physics*, 109(7):2826–2832, 1998.

[90] J.F. Nagle and S. Tristram-Nagle. Structure of lipid bilayers. *Biochimica et Biophysica Acta*, 1469(3):159–195, 2000.

[91] P.B. Moore, C.F. Lopez, and M.L. Klein. Dynamical properties of a hydrated lipid bilayer from a multinanosecond molecular dynamics simulation. *Biophysical Journal*, 81(5):2484–2494, 2001.

[92] E. Lindahl and O. Edholm. Molecular dynamics simulations of nmr relaxation rates and slow dynamics in lipid bilayers. *The Journal of Chemical Physics*, 115(10):4938–4950, 2001.

[93] C. Hofsäβ, E. Lindahl, and O. Edholm. Molecular dynamics simulations of phospholipid bilayers with cholesterol. *Biophysical Journal*, 84(4):2192–2206, 2003.

[94] G. Cevc. *Phospholipids Handbook*, chapter Solute transport across bilayers, pages 639–661. Marcel Dekker, New York, 1993.

[95] M. Pasenkiewicz-Gierula, K. Murzyn, T. Róg, and C. Czaplewski. Molecular dynamics simulation studies of lipid bilayer systems. *Acta Biochimica Polonica*, 47(3):601–611, 2000.

[96] T. Róg, K. Murzyn, and M. Pasenkiewicz-Gierula. Molecular dynamics simulations of charge and neutral lipid bilayers: Treatment of electrostatic interactions. *Acta Biochimica Polonica*, 50(3):789–798, 2003.

[97] S.W. Chiu, E. Jakobsson, S. Subramaniam, and H. Larry Scott. Combined monte carlo and molecular dynamics simulation of fully hydrated dioleyl and palmitoyl-oleyl phosphatidylcholine lipid bilayers. *Biophysical Journal*, 77(5):2462–2469, 1999.

[98] J.J. Chou, J.L. Baber, and Ad. Bax. Characterization of phospholipid mixed micelles by translational diffusion. *Journal of Biomolecular NMR*, 29:299308, 2004.

[99] R.A. Böckmann, A. Hac, T. Heimburg, and H. Grubmüller. Effect of sodium chloride on a lipid bilayer. *Biophysical Journal*, 85:16471655, 2003.

[100] D.P. Tieleman and H.J.C. Berendsen. Molecular dynamics simulations of a fully hydrated dipalmitoylphosphatidylcholine bilayer with different macroscopic boundary conditions and parameters. *The Journal of Chemical Physics*, 105:4871–4880, 1996.

[101] J. Saccani, S. Castano, B. Desbat, and D. Blaudezy. A phospholipid bilayer supported under a polymerized langmuir film. *Biophysical Journal*, 85:37813787, 2003.

[102] S. Leekumjorn and A.K. Sum. Molecular simulation study of structural and dynamic properties of mixed dppc/dppe bilayers. *Biophysical Journal*, 90(11):39513965, 2006.

[103] A.H. Schrijvers, P.M. Frederik, M.C. Stuart, K.N. Burger, V.V. Heijnen, Van der Vusse G.J., and R.S. Reneman. Formation of multilamellar vesicles by addition of tannic acid to phosphatidylcholine-containing small unilamellar vesicles. *Journal of Histochemistry and Citochemistry*, 37(11):1635–1643, 1989.

[104] B.G. Murphy and L.A. Engel. Models of the pressure-volume relationship of the human lung. *Respiration Physiology*, 32(2):183–194, 1978.

[105] B.A. Lewis and D.M. Engelman. Lipid bilayer thickness varies linearly with acyl chain length in fluid phosphatidylcholine vesicles. *Journal of Molecular Biology*, 166(2):211–217, 1983.

[106] M.J. Janiak, D.M. Small, and Shipley G.G. Temperature and compositional dependence of the structure of hydrated dimyristoyl lecithin. *The Journal of Biological Chemistry*, 254(13):6068–6078, 1979.

[107] R.P. Rand and V.A. Parsegian. Hydration forces between phospholipid bilayers. *Biochimica et Biophysica Acta*, 998:351–376, 1989.

[108] H.I. Petrache, S.W. Dodd, and M.F. Brown. Area per lipid and acyl length distributions in fluid phosphatidylcholines determined by 2h nmr spectroscopy. *Biophysical Journal*, 79(6):3172–3192, 2000.

[109] M. Patra, M. Karttunen, M.T. Hyvönen, E. Falck, P. Lindqvist, and I. Vattulainenz. Molecular dynamics simulations of lipid bilayers: Major artifacts due to truncating electrostatic interactions. *Biophysical Journal*, 84:3636–3645, 2003.

[110] J.J. López Cascales, T.F. Otero, B.D. Smith, C. González, and M. Márquez. Model of an asymmetric dppc/dpps membrane: Effect of asymmetry on the lipid properties. a molecular dynamics simulation study. *Journal of Physical Chemistry B*, 110:2358–2363, 2006.

Appendix I.

Computational set-up for the POPC bilayer

The *Molecular Dynamics* model for the POPC bilayer, described in subsection 3.2.1, has been generated using VMD package [82].

Into the list of software utilities provided by this package, known as plugins, there is one called membrane. This is a collection of routines which can be executed into de VMD tcl/tk console to generate a hydrated phospholipid bilayer (See http://www.ks.uiuc.edu/Research/vmd/plugins/membrane for more details).

Let's generate a hydrated POPC bilayer of 50 x 50 Å perpendicular to Z axe into the needed NAMD files ("POPCMembrane.pdb" and "POPCMembrane.psf"). The tcl/tk code for that would be:

```
package requires membrane
membrane -l POPC -x 50 -y 50 -o POPCMembrane
```

In any case, it is usually desired to include more water molecules into the model in order to get some matter to propagate a shock wave, a few amstrongs would be enough. This can be done using another VMD plugin called solvate, which has been implemented into the VMD GUI (See http://www.ks.uiuc.edu/Research/vmd/plugins/solvate for more details).

But before doing this, it is necessary to calculate the boundaries of the model, so you will know the maximum and minimum coordinates of the generated model and you will be able to add more water over and underneath your

bilayer. That can be obtained with the next tcl code with the model loaded into VMD:

```
set everyone [atomselect top all]
set outfile [open Geom.res w]
puts $outfile [measure minmax $everyone]
puts $outfile [measure center $everyone]
```

, which generates a file called "Geom.res" with the minimum, maximum and center XYZ coordinates of your *Molecular Dynamics* box.

Solvate could be used to generate two layers of water of 50 Å at both sides of the membrane. That would be from minimum Z to minimum Z - 50 and from maximum Z to maximum Z + 50. It is usually desirable to use a margin of about 5 Å in the X and Y axes to get the water layers into the area of the membrane. In any case, the particles will find their place after the minimisation process.

Once your membrane is generated and properly hydrated, the minimisation process, described in subsection 4.1.1, can be computed. The configuration file for that would be:

```
structure          "POPCmembrane.psf"
coordinates        "POPCmembrane.pdb"
temperature        0
parameters         "par_all27_lipid.prm"
paraTypeCharmm     on

outputEnergies     10
outputTiming       100
xstFreq            100
dcdFreq            100
wrapAll            on
wrapNearest        on

timestep             1
nonBondedFreq        2
fullElectFrequency   4
stepsPerCycle       20

switching          on
switchDist        8.5
cutoff           10.0
```

```
pairlistdist 11.5

cellBasisVector1 56.0    0.0   0.0
cellBasisVector2  0.0   55.0   0.0
cellBasisVector3  0.0    0.0  95.0
cellOrigin       -23.0  -22.0   1.0
margin 5

Pme            on
PmeGridsizeX 10
PmeGridsizeY 10
PmeGridsizeZ 10

exclude scaled1-4
1-4scaling 1.0

langevin           on
langevinDamping    10
langevinTemp      310
langevinHydrogen   no

langevinPiston        on
langevinPistonTarget 1.01325
langevinPistonPeriod 200
langevinPistonDecay  100
langevinPistonTemp   310

useGroupPressure yes
useFlexibleCell  yes
useConstantRatio yes

binaryoutput off
outputname   "POPCMembrane minimisation"

# run one step to get into scripting mode
minimize 0
langevinPiston off

minimize 1000
output   "POPCMembrane minimisation MinAll"

run     1000
```

```
output "POPCMembrane minimisation Heat"

langevinPiston    on
run              3000
output           "POPCMembrane minimisation Langevin"

run     45000
output "POPCMembrane minimisation Equil"
```

(The cell parameters, this is CellBasis and CellOrigin, should be changed to the particular case. They refer to the boundaries of the model which can be obtained as described before into a "Geom.res" file).

The file "par_all27_lipid.prm" contains the necessary parameters for the potential function and it can be freely downloaded from Internet.

(See http://mackerell.umaryland.edu/CHARMM_ff_params.html)

As NAMD [72] package let define the initial velocities of the particles using a Pdb format file, reading the final velocities of the particles from the generated file after the minimisation process, "POPCMembrane minimisation.vel" in our example, and conveniently changing the values for the Z direction as described in subsection 4.1.2, a velocity file for the simulation process described in subsection 4.1.3, called "POPCMembrane.vel", can be created.

Therefore, the launch of the NPT simulation into NAMD can be undertaken using the next configuration file, where "POPCMembrane minimisation.coor" and "POPCMembrane minimisation.xsc" are result files from the minimisation process:

```
structure        "POPCMembrane.psf"
coordinates      "POPCMembrane minimisation.coor"
velocities       "POPCMembrane.vel"
extendedSystem   "POPCMembrane minimisation.xsc"
parameters       "par_all27_lipid.prm"
paraTypeCharmm   on

outputEnergies    10
outputTiming     100
xstFreq          100
dcdFreq          100
wrapAll           on
wrapNearest       on
```

```
timestep              1
nonBondedFreq         2
fullElectFrequency    4
stepsPerCycle        20

switching       on
switchDist     8.5
cutoff        10.0
pairlistdist  11.5
margin           2

Pme            on
PmeGridsizeX  10
PmeGridsizeY  10
PmeGridsizeZ  10

exclude scaled1-4
1-4scaling 1.0

langevin          on
langevinDamping    1
langevinTemp     310
langevinHydrogen no

langevinPiston        on
langevinPistonTarget  1.01325
langevinPistonPeriod  200
langevinPistonDecay   500
langevinPistonTemp    310

useGroupPressure yes
useFlexibleCell  yes
useConstantRatio yes

binaryoutput off
outputname   "POPCMembrane simulation"

firsttimestep 50000
run           200000
```

After the computation, the results can be calculated from the position of the particles for each time step. These values can be obtained from the tcl/tk console into VMD (See http://tcl.sourceforge.net for more details about tcl/tk programming language). With the model loaded into VMD, which can be done using:

```
mol delete all
menu animate on
mol load psf "POPCMembrane.psf" pdb "POPCMembrane.pdb"
animate read dcd "POPCMembrane minimisation.dcd"
```

or

```
mol delete all
menu animate on
mol load psf "POPCMembrane.psf" pdb "POPCMembrane.pdb"
animate read dcd "POPCMembrane simulation.dcd"
```

,the code to obtain the position of the particles for each time step would be:

```
pbc unwrap -all

set Atom [atomselect top all]
set FrameN [molinfo top get numframes]

set outfile [open Results.idc w]

puts $outfile "[$Atom num] $FrameN"

for {set FrameI 0} {$FrameI<$FrameN} {incr FrameI 1} {
set Frame [atomselect top all frame $FrameI]
puts $outfile [$Frame get
    {resname segname resid name index x y z}]
$Frame delete
}

close $outfile
```

This last tcl/tk code generates a file called "Results.idc" which contains the position of each particle for all the time step along the computation.

Appendix II.

Computational set-up for the alveolar surface

In the case of the alveolar surface, there was not any pre-built package or plugin that could be used to generate the model as it was a very particular case: The phospholipid heads pointing inwards, layers of air molecules and surfactant proteins embedded into the membranes.

Reading the phospholipid molecule from a pdb file int a Pdb programming structure. The C++ code made to generate the lattice of phospholipids into a pdb file is shown next:

```
void LatticeGenerator(TPdb *Pdb)
{  const int ni=Pdb->Atom->Count;
   // Number of atoms of the lipid
   const int nj=EditInt1->Value;
   // Number of lipids in X axe lattice
   const int nk=EditInt2->Value;
   // Number of lipids in Y axe lattice

   double AX,AY,AZ,KZ=1.0,WX2,WY2,ZMin1,ZMin2;
   FILE *fres;
   int i,j,k,l;
   String Line;

   AX=Pdb->Atom->MaxX-Pdb->Atom->MinX;
   // Wide of the lipid
   AY=Pdb->Atom->MaxY-Pdb->Atom->MinY;
```

```
// Length of the lipid
AZ=Pdb->Atom->MaxZ-Pdb->Atom->MinZ;
// Height of the lipid

WX2=0.5*double(nj)*AX;
// Half the total wide of the lattice
WY2=0.5*double(nk)*AY;
// Half the total length of the lattice

fres=fopen(FileName,"w");
// Open result pdb file

ZMin1=Pdb->Atom->MinZ;
// Initial minimum Z of the lipid

for (l=0;l<2;l++)
{  Pdb->Atom->Rotate(180.0,0.0,0.0);
   // Lipid rotation. Heads pointing inward
   Pdb->Atom->Initiate();
   // Center the lipid to the coordinate origin

   ZMin2=Pdb->Atom->MinZ;
   // Current minimum Z of the lipid

   for (k=0;k<nk;k++)
   // Loop over the lipids in X axe
   {  for (j=0;j<nj;j++)
      // Loop over the lipids in Y axe
      {  Pdb->Atom->Rotate(0.0,0.0
                           ,double(random(360));
         // Include some disorder

         for (i=0;i<ni;i++)
         // Loop over the atoms of the lipid
         {  Line=Pdb->Atom->LineStr(i,
                  ,Pdb->Atom->ValueX->Value[i]
                  -WX2+AX*double(j)
                  ,Pdb->Atom->ValueY->Value[i]
                  -WY2+AY*double(k)
                  ,Pdb->Atom->ValueZ->Value[i]
                  -(AZ-ZMin1+ZMin2)*KZ*double(l));
            // Calculate the new coordinates of the
```

```
                // lipid translated into the lattice

                fprintf(fres,"%s\n",Line);
                // Print the line to the pdb result file
            }
        }
    }

    Pdb->Atom->Rotate(180.0,0.0,0.0);
    Pdb->Atom->Initiate();
    // Take the lipid to its original position to
    // process the next one
  }

  fprintf(fres,"%s","END");
  fclose(fres);
  // Close result pdb file
}
```

Similar processes can be use to include the air particles and the proteins into the model.

In the first case, the air particles, the boundaries of the model must known before hand, which can be calculated once you load your pdb modelinto VMD using the next code into the tcl/tk console and obtaining the consequent "Geom.res" file:

```
set everyone [atomselect top all]
set outfile [open Geom.res w]
puts $outfile [measure minmax $everyone]
puts $outfile [measure center $everyone]
```

For the second case, the proteins inclusion, it is desirable to have a routine to merge the proteins and the membranes and remove the lipids that overlap with the protein groups.

(See "http://www.ks.uiuc.edu/Research/vmd/plugins/membrane" for details about this process)

In order to generate the psf structure file for NAMD from your generated pdb file, VMD provides a psf generator which is possible to use into the tcl/tk console. The code is:

```
package require psfgen
topology top_all27_prot_lipid.rtf
segment U {pdb FileName.pdb}
coordpdb FileName.pdb U
regenerate angles dihedrals
guesscoord
writepdb AlveolarMembrane.pdb
writepsf AlveolarMembrane.psf
exit
```

Once you get the pbd and the psf files of your model you can start your calculation. The minimisation process can be launched using the next configuration file:

```
structure          "AlveolarMembrane.psf"
coordinates        "AlveolarMembrane.pdb"
temperature        0
parameters         "par_all27_prot_lipid.prm"
parameters         "Air.prm"
paraTypeCharmm     on

outputEnergies     10
outputTiming       100
xstFreq            100
dcdFreq            100
wrapAll            on
wrapNearest        on

timestep           1
nonBondedFreq      2
fullElectFrequency 4
stepsPerCycle      20

switching          on
switchDist         8.5
cutoff             10.0
pairlistdist       11.5

cellBasisVector1   102.0   0.0    0.0
cellBasisVector2   0.0     80.0   0.0
cellBasisVector3   0.0     0.0    167.0
```

```
cellOrigin          -8.0 -9.0 -14.0
margin 10

Pme             off
PmeGridsizeX 100
PmeGridsizeY  80
PmeGridsizeZ 160

exclude scaled1-4
1-4scaling 1.0

langevin            on
langevinDamping    10
langevinTemp      307
langevinHydrogen   no

langevinPiston         on
langevinPistonTarget 1.01325
langevinPistonPeriod 200
langevinPistonDecay  100
langevinPistonTemp   300

useGroupPressure yes
useFlexibleCell  yes
useConstantRatio yes

binaryoutput off
outputname "AlveolarMembrane minimisation"

# run one step to get into scripting mode
minimize 0
langevinPiston off

minimize 6000
output   "AlveolarMembrane minimisation MinAll"

run     2000
output "AlveolarMembrane minimisation Heat"

langevinPiston on
run     2000
output "AlveolarMembrane minimisation Langevin"
```

```
run 40000
```

(The cell parameters, this is CellBasis and CellOrigin, should be changed to the particular case. They refer to the boundaries of the model which can be obtained as described before into a "Geom.res" file).

The file "par_all27_prot_lipid.prm" contains some of the parameters for the potential function and it can be freely downloaded from Internet.

(see http://mackerell.umaryland.edu/CHARMM_ff_params.html)

"Air.prm" contains the parameters used for the simulation of the air particles [84]. This last file is shown next.

```
NONBONDED
!V(Lennard-Jones) = Eps,i,j[(Rmin,i,j/ri,j)**12
! - 2(Rmin,i,j/ri,j)**6]
!
!epsilon: kcal/mole, Eps,i,j = sqrt(eps,i * eps,j)
!R: Kb*Na=8.314472 J/K/mol
!Air: 103.3*R*0.2388459E-03 = 0.2051 Kcal/mol
!Rmin/2: A, Rmin,i,j = Rmin/2,i + Rmin/2,j
!
!atom ignored epsilon Rmin/2 ignored eps,1-4 Rmin/2,1-4
!
AirT     0.0       -0.2051  1.8000
```

The launch of the NVE simulation into NAMD can be undertaken using the next configuration file, where "AlveolarMembrane minimisation.coor", "AlveolarMembrane minimisation.vel" and "AlveolarMembrane minimisation.xsc" are result files from the minimisation process:

```
structure        "AlveolarMembrane.psf"
coordinates      "AlveolarMembrane minimisation.coor"
velocities       "AlveolarMembrane minimisation.vel"
extendedSystem   "AlveolarMembrane minimisation.xsc"
parameters       "par_all27_prot_lipid.prm"
parameters       "Air.prm"
paraTypeCharmm   on

outputEnergies   10
outputTiming     100
```

```
xstFreq          100
dcdFreq          100
wrapAll           on
wrapNearest       on

timestep           1
nonBondedFreq      2
fullElectFrequency  4
stepsPerCycle     20

switching        on
switchDist      8.5
cutoff         10.0
pairlistdist   11.5

cellBasisVector1  106.0   0.0    0.0
cellBasisVector2    0.0  81.0    0.0
cellBasisVector3    0.0   0.0  163.0
cellOrigin         -7.0  -8.0  -13.0

exclude scaled1-4
1-4scaling        1.0

useGroupPressure    yes

binaryoutput  off
outputname    "AlveolarMembrane simulation"

firsttimestep   50000
run            250000
```

(The cell parameters, this is CellBasis and CellOrigin, should be changed to the particular case. They refer to the boundaries of the model which can be obtained as described before into a "Geom.res" file after the minimisation process).

After the computation, the results can be calculated from the position of the particles for each time step. These values can be obtained from the tcl/tk console (See http://tcl.sourceforge.net for more details about tcl/tk programming language). With the model loaded into VMD, which can be done using:

```
mol delete all
```

```
menu animate on
mol load psf "AlveolarMembrane.psf"
    pdb "AlveolarMembrane.pdb"
animate read dcd "AlveolarMembrane minimisation.dcd"
```

or

```
mol delete all
menu animate on
mol load psf "AlveolarMembrane.psf"
    pdb "AlveolarMembrane.pdb"
animate read dcd "AlveolarMembrane simulation.dcd"
```

,the code to obtain the position of the particles for each time step would be:

```
pbc unwrap -all

set Atom [atomselect top all]
set FrameN [molinfo top get numframes]

set outfile [open Results.idc w]

puts $outfile "[$Atom num] $FrameN"

for {set FrameI 0} {$FrameI<$FrameN} {incr FrameI 1} {
set Frame [atomselect top all frame $FrameI]
puts $outfile [$Frame get
    {resname segname resid name index x y z}]
$Frame delete
}

close $outfile
```

This last tcl/tk code generates a file called "Results.idc" which contains the position of each particle for all the time step along the computation.

Appendix III.

Author's publications

- J. Lechuga, D. Drikakis and S. Pal. Molecular dynamics study of the interaction of a shock wave with a biological membrane. *International Journal for Numerical Methods in Fluids*.
- S. Pal, J. Lechuga and D. Drikakis. On the controversy of the alveolar structure: A Molecular Dynamics Study. *ARS Conference 2007*.
- J. Lechuga, D. Drikakis and S. Pal. *Journal of Computational and Theoretical Nanoscience*. (In preparation).